Coupled lattice Boltzmann and discrete element method for reactive particle fluid flows with applications in process engineering

zur Erlangung des akademischen Grades einer

DOKTORIN DER INGENIEURWISSENSCHAFTEN (Dr.-Ing.)

von der KIT-Fakultät für Chemieingenieurwesen und Verfahrenstechnik des
Karlsruher Instituts für Technologie (KIT)

genehmigte

DISSERTATION

von

Marie-Luise Maier

aus Karlsruhe

Referent: Prof. Dr.-Ing. Hermann Nirschl
Erste Korreferentin: PD Dr. Gudrun Thäter
Zweiter Korreferent: Dr. Mathias J. Krause

Tag der mündlichen Prüfung: 30. April 2021

Acknowledgements

The contents of this thesis were developed during my work as a research assistant at the Institute of Mechanical Process Engineering and Mechanics (MVM) at the Karlsruhe Institute of Technology (KIT).

My special thanks go to Prof. Dr.-Ing. habil. Nirschl for giving me the confidence and the opportunity to carry out this research.

I would like to thank Dr. Mathias J. Krause, head of the Lattice Boltzmann Research Group (LBRG), for the good cooperation and mutual support. His commitment to forward the *OpenLB* code is remarkable. This gave me and gives many researchers the opportunity to apply lattice Boltzmann methods to a multitude of advanced technical applications.

Furthermore, I would like to thank the German Research Foundation (DFG) for the project funding and the Karlsruhe House of Young Scientists (KHYS) for the financial support during my research stay at the Paul Scherrer Institute (PSI) in Villigen, Switzerland. Many thanks go to Prof. Dr. Sergey Churakov, Dr. Nikolaos Parasianakis and Dr. Ravi A. Patel from PSI for the kind support to deepen the reactive flow simulations. The discussions with Ravi were very helpful as was his valuable advice in writing this thesis.

I am happy about the contribution of many motivated students, which has led to the success of this work. I would like to mention Stefanie Milles, Sascha Janz, Hoon Seng Chan, Asher Zarth, Michael Bonavia, Philipp Klas, Julius Wörner, Thomas Fuchs and Matthias Brosz.

I would also like to thank all my colleagues from MVM and LBRG for the helpful discussions and the pleasant working atmosphere. Many friendships have developed during this time. I have always enjoyed going to work even in difficult and stressful times.

A heartfelt and warm thank you to my parents for their unconditional and loving support during my entire career. I am also very happy that my siblings and I help each other with advice and support whenever necessary.

Above all I would like to thank my husband for his patience, understanding and constant support in general and also during the time I wrote this thesis. This enabled me to finish this work even with our little daughter. I am very grateful to have you both!

Abstract

The present work deals with the numerical simulation of reactive particle fluid systems that are of great importance for a multitude of practical applications in process engineering. Examples include the biomass conversion in photo-bio-reactors, chemical catalytic reactors or fluidized bed reactors. In waste water treatment, calcium silicate hydrate particles are utilized to remove dissolved phosphate by adsorption. Most studies on reactive particle fluid systems by numerical simulation consider fixed bed reactors with static solid particles. Investigations on reactions to moving particles are rare. Furthermore, grid convergence studies of all components are often missing, especially for two-way coupled systems. A proper reactive transport model that takes into account the coupling of fluid and moving particles is of essential use and needs further research.

The focus of this thesis is on the development of a novel Euler-Lagrange algorithm for reactive particle fluid flows in order to investigate the uptake of the dissolved substance to the particles. This is to be achieved by suitable simulation tools for calculating the fluid dynamics, the components' mixing and interaction for a better understanding of the overall process. A consistent coupling and a proper validation of the models is of great importance.

The lattice Boltzmann methods are applied to numerically solve the continuity, the Navier-Stokes, the advection-diffusion-reaction equations and their volume-averaged counterparts. They are very well suited due to the ability to handle complex domains and the intrinsically parallel algorithm which scales reasonably well. The particles are considered as sub-grid particles and are described by discrete particle methods. The coupling of the components is modeled by both one-way and two-way coupling that depends on whether the suspension is dense or diluted. The methods are validated either by experimental data from measurements, from the literature or by comparative simulations of thoroughly tested approaches. Furthermore, grid studies show the convergence of the simulations.

First, a one-way coupled simulation of reactive particle fluid flows is carried out. The fluid flow and mixing simulations of the components show a very good agreement in comparison to *in-situ* studies using magnetic resonance imaging and optical investigations by use of an ink solution. The grid study of the mass transport simulation performs very well. First

simulations of reactions to the surface of moving particles suspended in water show the adequacy of the method for reactive particle fluid flows.

The simulation of a single particle settling in initially resting fluid is investigated with a novel two-way coupling approach where both fluid and reactive substance are treated in a continuous frame by a volume-averaged procedure. The two-way coupling with the particles is realized by consideration of drag force and changes in porosity. In addition, the change in porosity affects the diffusion coefficient. The simulation results agree well with the results from the literature. Furthermore, grid studies demonstrate that the simulation converges for both fluid and particle velocities. To further investigate the reactive particle fluid flow, the approach is applied to fixed particles in a channel. The reactions are considered to take place at the surface of the particles, realized by a linear sink term in the advection-diffusion-reaction equation. Comparative studies show the accuracy, grid studies the convergence of the simulation approach. A multi-particle simulation of 1.000, 2.000 and 3.000 particles is performed for both one-way and two-way coupling to demonstrate the potential of the method. At lower porosity the effects of two-way coupling are clearly visible.

The specific separation of target proteins from the fermentation broth by surface function-alized magnetic carrier particles is an application of reactive particle fluid flows in biotech-nological processes. Particle separation is achieved by magnetic forces. Here, a simulation of the particle separation is carried out in a complete device. The influence of process parameters such as volume flow, particle size or magnetization on the particle separation is investigated.

The one-way and two-way coupled lattice Boltzmann and discrete particle methods presented in this thesis successfully reproduce the expected behavior of the reactive particle fluid flow applications. They promise that they are accurate tools for the simulation of dilute, respective dense reactive particle fluid applications. The numerical simulations help to e.g. optimize the uptake of phosphate on calcium silicate hydrate particles by finding optimal process parameters.

Zusammenfassung

Die vorliegende Arbeit befasst sich mit der numerischen Simulation reaktiver Partikel-Fluid Systeme, die für eine Vielzahl von praktischen Anwendungen in der Verfahrenstechnik von großer Bedeutung sind. Beispiele sind die Umwandlung von Biomasse in Photobioreaktoren, chemisch-katalytische Reaktoren oder Wirbelschichtreaktoren. In der Abwasserbehandlung werden Partikel aus Kalziumsilikathydrat verwendet, um gelöstes Phosphat durch Adsorption zu entfernen. Die meisten Studien zu reaktiven Partikel-Fluid Systemen mittels numerischer Simulation betrachten Festbettreaktoren. Untersuchungen zu Reaktionen an mitströmende Partikel sind selten. Darüber hinaus gibt es wenige Studien zur Gitterkonvergenz der Komponenten, insbesondere für Zwei-Wege gekoppelte Systeme. Ein geeignetes reaktives Transportmodell, das die Kopplung von Fluid und mitströmenden Partikeln berücksichtigt, ist von wesentlichem Nutzen und bedarf weiterer Forschung.

Der Schwerpunkt dieser Arbeit liegt auf der Entwicklung eines neuartigen Euler-Lagrange Algorithmus für reaktive Partikel-Fluid Strömungen, um die Aufnahme gelöster Stoffe an die Partikel zu untersuchen. Dies soll zum besseren Verständnis des Gesamtprozesses durch geeignete Simulationswerkzeuge zur Berechnung der Fluiddynamik, der Durchmischung und der Interaktion der Komponenten erreicht werden. Eine konsequente Kopplung und eine ordnungsgemäße Validierung der Modelle ist dabei von großer Bedeutung.

Die Lattice-Boltzmann-Methoden werden zur numerischen Lösung der Kontinuitäts-, der Navier-Stokes- und der Advektions-Diffusions-Gleichungen inklusive Reaktionen sowie zur Lösung der volumengemittelten Gleichungen angewendet. Sie eignen sich sehr gut, da sie auch in komplexen Gebieten verwendet werden können und der Algorithmus intrinsisch parallel und gut skalierbar ist. Die Partikel werden als *sub-grid* Partikel betrachtet und mit diskreten Partikelmethoden beschrieben. Die Kopplung der Komponenten wird sowohl durch Einweg- als auch durch Zweiwegkopplung modelliert und hängt davon ab, ob die Suspension dicht oder verdünnt ist. Die Methoden werden entweder anhand experimenteller Daten aus Messungen, aus der Literatur oder anhand vergleichender Simulationen gründlich getesteter Ansätze validiert. Darüber hinaus zeigen Gitterstudien die Konvergenz der Simulationen.

Zunächst wird eine Ein-Weg gekoppelte Simulation eines reaktiven Partikel-Fluid Systems durchgeführt. Die Strömungs- und Mischungssimulationen der Komponenten zeigen eine sehr gute Übereinstimmung im Vergleich zu *in-situ*-Studien mit Magnetresonanztomographie und optischen Untersuchungen. Die Gitterstudie der Massentransportsimulation ist ebenfalls vielversprechend. Erste Simulationen der Adsorption an bewegten, in Wasser suspendierten Partikeln zeigen die Eignung der Methode für reaktive Partikel-Fluid Strömungen.

Die Simulation eines einzelnen Partikels, das sich in zunächst ruhender Flüssigkeit absetzt, wird mittels Zweiwege-Kopplung untersucht. Die Ergebnisse stimmen gut mit den Ergebnissen aus der Literatur überein. Darüber hinaus zeigen Gitterstudien, dass die Simulation sowohl für Flüssigkeits- als auch für Partikelgeschwindigkeiten konvergiert. Um die reaktive Partikel-Fluid Strömungen zu testen, wird der Ansatz an in einem Kanal fixierte Partikel angewendet. Die Adsorption, die an der Oberfläche der Partikel stattfindet, wird durch einen linearen Senken-Term in der Advektions-Diffusions-Reaktionsgleichung berücksichtigt. Vergleichende Studien zeigen die Genauigkeit, Gitterstudien die Konvergenz des Simulationsansatzes. Eine Simulation mit 1.000, 2.000 und 3.000 Partikeln wird sowohl für die Einweg- als auch für die Zweiwegkopplung durchgeführt, um das Potenzial der Methode aufzuzeigen. Je kleiner die Porosität, desto deutlicher sind die Auswirkungen der Zweiwege-Kopplung ersichtlich.

Die gezielte Abtrennung von Zielproteinen aus der Fermentationsbrühe durch oberflächenfunktionalisierte magnetische Trägerpartikel ist eine Anwendung reaktiver Partikel-Fluid Strömungen in biotechnologischen Prozessen. Die Abtrennung der Partikel wird durch magnetische Kräfte erreicht. Hier wird eine Simulation der Partikelabscheidung in einem kompletten Gerät durchgeführt, um den Einfluss von Prozessparametern wie Volumenstrom, Partikelgröße oder Magnetisierung auf die Partikelabscheidung zu untersuchen.

Die in dieser Arbeit vorgestellten Ein-Weg und Zwei-Weg gekoppelten Lattice-Boltzmann- und diskrete Partikelmethoden reproduzieren erfolgreich das erwartete Verhalten der reaktiven Partikel-Fluid Systeme. Es wird aufgezeigt, dass sie korrekte Werkzeuge für die Simulation verdünnter, beziehungsweise dichter reaktiver Partikel-Fluid Systeme sind. Die numerischen Simulationen ermöglichen es, z. B. die Phosphatbeladung an Partikel aus Kalziumsilikathyadrat zu optimieren, in dem die optimalen Prozessparameter berechnet werden.

List of acronyms

ADRE   advection-diffusion-reaction equation

BE   Boltzmann equation

BGK   Bhatnagar–Gross–Krook

C-S-H   calcium silicate hydrate

DEM   discrete element method

EDF   equilibrium distribution function

EOC   experimental order of convergence

F   forcing

FEM   finite element method

LBE   lattice Boltzmann equation

LBM   lattice Boltzmann method

MRI   magnetic resonance imaging

NSE   Navier-Stokes equation

P-RoC   phosphorus recovery by crystallization

PCR   pressure correction term

SRT   single relaxation time

TRT   two relaxation time

VAADRE   volume-averaged advection-diffusion-reaction equation

VANSE   volume-averaged Navier–Stokes equation

Contents

1 Introduction

Reactive particle fluid systems are of prime importance in a variety of practical applications in process engineering, e.g. the biomass conversion in photo-bio-reactors, chemical catalytic reactors or fluidized bed reactors. As a practical example, this thesis considers the phosphorus recovery by crystallization (P-RoC)$^{\copyright}$ process, that stands for *p*hosphorus *rec*overy by *c*rystallization to calcium silicate hydrate (C-S-H) [1]. It targets to remove phosphate from e.g. industrial waste water by adsorption of phosphate ions on C-S-H particles. For such systems modeling and numerical simulation have a large potential to help to optimize process conditions, e.g. particle size distributions or volume flows. Simulations of reactive particle fluid flows require the simulation of the carrier fluid, the mass transport of the reactive substance and the solid particles. As the simulation of the sub-grid particle interactions as well as the coupling to the fluid and to the reactive substance is computational expensive, the computational demand is possible to be compensated by a highly parallel and fast algorithm like the lattice Boltzmann method (LBM). In the past decades, the LBM is applied to simulate complex flows. The explicit algorithm with inherent parallelization originates from the Boltzmann equation. It has turned out to be an attractive alternative to conventional numerical methods due to its simple algorithm and the underlying equidistant grid without necessity to adapt it to the geometry. It is able to handle complex domains and the parallel algorithm can scale reasonably well [2–4].

Simulations of reaction processes between the components and taking into account the hydrodynamic influence have already been carried out in several numerical studies, among others using the LBM. Most works consider packed bed reactors [5–7]. For instance, Agawarl et al. [8] and Manjhi et al. [9] consider the decrease in concentration due to adsorption on immobile packed particles in a fixed bed using an Euler-Euler approach. They calculate the water and concentration transport by LBM and model the adsorption by a global sink term. Patel et al. [10] use the LBM in combination with a reactive transport model to simulate changes in the micro structure of cement-based materials such as portlandite or C-S-H due to calcium leaching. Studies of reactions that happen to moving particles are

rare [11]. Additionally, a consistent coupling of the three components as well as numerical grid convergence studies do not exist.

The challenge faced in this work is to research an efficient approach that allows to study, understand and predict the dynamics of reactive particle fluid flows in e.g. process engineering. The contribution of this thesis is to develop, implement, validate and apply numerically convergent LBM-based algorithms for that purpose. The main aim is to present a novel LBM-based Euler-Lagrange approach that considers reaction processes on moving particles by a one-way, respective a fully two-way coupling of the components.

In the developed methodology of a one-way coupled approach, the fluid flow and the reactive substance transport are described by an Euler approach, the suspended and moving particles by a Lagrange approach. The carrier fluid is assumed to be incompressible and Newtonian modeled by the continuity and the Navier-Stokes equation (NSE). The mass transport of the reactive substance is modeled by the advection-diffusion-reaction equation (ADRE). The particle phase is represented by a collection of discrete sub-grid particles, their trajectories are obtained by solving Newton's equation of motion. The implementation is realized using and advancing the open-source C++ software project *OpenLB* (`http://www.openlb.net`). *OpenLB* contains many methods and approaches that can be used for the development of e.g. particle fluid flows, reactive, thermal or turbulent flows, light transport, fluid-structure interaction or flows in porous media and complex geometries. An overview is given in [12]. The flow field is validated by an *in-situ* study by magnetic resonance imaging (MRI), the components' mixing by optical examination and a grid study. It is shown that reactions to the surface of moving particles by simulation is possible.

The use of volume-averaged equations for reactive particulate fluid flows is the key difference between the previously proposed model and the developed methodology of the fully two-way coupled multi-scale Euler-Lagrange approach. The fluid and the reactive transport processes are treated in a continuous framework through a volume-averaging procedure. The governing equations are given by the volume-averaged Navier–Stokes equation (VANSE) and the volume-averaged advection-diffusion-reaction equation (VAADRE). The effect of the sub-grid particles on the fluid is considered by the change in porosity and by the drag force. Additionally, the effect on the reactive mass transport is considered by a change in the porosity that is included in the diffusion coefficient. The implementation is done in the LBM based framework *Yantra* (`https://bitbucket.org/yantralbm/yantra/src/master/`), an open-source framework to simulate multi-component reactive transport at the pore as well as at the meso- and the continuum scale [13, 14]. It has been coupled to *Yade*, an open-source

framework (`https://gitlab.com/yade-dev`) for modeling particles using the discrete element method (DEM). The method is applied to the single particle sedimentation in a steady fluid. The results are compared to experimental data from literature. Grid convergence studies applied to reactive particle fluid flows are conducted. Comparative studies are performed for validation purposes. Finally, a demonstration case showing full potential of the developed model is presented.

The implemented and validated one-way coupled approach is applied to study the real case of the magnetic particle separation in a complete device. Magnetic carrier particles are separated by magnetic forces that originate from an external magnetic field that is computed by finite element method (FEM). The magnetic field is obtained by *COMSOL Multiphysics® 5.3, magnetic fields - no currents* [15] loaded into *OpenLB* to perform the particle separation. The particle separation is studied for two different volume flows, two different particle fractions and two different saturation magnetizations. This shows the potential of possible extensions of the present work in other applications of reactive particle fluid flow e.g. to specifically separate target proteins from the fermentation broth by surface-functionalized magnetic carrier particles [16].

The thesis is divided into two parts. Part I deals with the mathematical formulation of the governing equations and the details of the LBM based Euler-Lagrange framework to model one- and two-way reactive particle fluid flows. Chapter 2 introduces the continuity equation, the NSE and the ADRE. Chapter 3 presents the volume-averaged equations for reactive particle fluid flows that allow to handle large porosity gradients and a two-way coupling. Chapter 4 introduces to the governing equations for solving particle motions and forces acting on the particles. In Part II, different applications are presented to demonstrate the potential of the developed framework. In Chapter 5, validations and applications related to one-way coupled reactive particle fluid flows are presented. The volume-averaging approach of the two-way coupled reactive particle fluid flows is applied in Chapter 6 and is validated by different experiments. Chapter 7 presents a real case scenario of a magnetic particle separation in a complete device. Chapter 8 summarizes this thesis and gives a conclusion of the thesis as well as an outlook about future research topics.

Part 1

Theory, governing equations and numerical realization

2 Modeling and simulation approaches of reactive flows

In this thesis the LBM is used as numerical technique for the calculation of the carrier fluid flow and the mass transport of the reactive substance. This chapter is therefore dedicated to provide a detailed description of the LBM. The chapter starts with explanation of the relevant length and time scales, followed by the governing equations for reactive flows. This is followed by a detailed derivation of the LBM which includes the derivation of the LBM equation from the discrete Boltzmann equation (BE) and the Chapman-Enskog equation to relate the LBM with the governing macroscopic equations. The dimensions are given by the corresponding symbols L (length), M (mass), T (time) and N (amount of substance).

2.1 Relevant length and time scales

The motion of a fluid can be described by various mathematical models that differ in the scale. The latter results from the respective point of view.

- In the *microscopic scale* the dynamics of interacting fluid atoms or molecules are included in the model equations of Newtonian dynamics. In liquids, the interacting forces are weak and a relative movement of the molecules is possible compared to molecules of solids. In gases these forces are much weaker, the molecules expand and occupy the available volume.

- In the *macroscopic scale* the fluid is considered as a continuous matter. The fact that it consists of single molecules is ignored by taking an exemplary volume of fluid that contains enough molecules to provide a statistically meaningful mean value. Fluid dynamics is described by changes e.g. in macroscopic fluid velocity or pressure. The length and time scales are chosen large enough to make the average valid. The governing equation on this scale is the NSE.

- A third scale, located between the microscopic and the macroscopic scale, is the *mesoscopic* scale. This is used to track the evolution of a distribution of fluid molecules, atoms or particles within a state averaged over time, space and velocity. This gives the probabilistic average behaviour of the quantity. The LBM works on the mesoscopic scale and is based on the kinetic theory.

There are several dimensionless quantities, e.g. the Reynolds number, the Mach number or the Knudsen number, that help to determine the appropriate flow model with respect to the different length and time scales.

- The *Knudsen number* Kn $[-]$,

$$\text{Kn} = \frac{L_{\text{mfp}}}{L_{\text{ch}}} \,, \tag{2.1}$$

is the ratio of the mean free path $L_{\text{mfp}} \in \mathbb{R}_{>0}$ $[L]$ between the molecules and the characteristic length $L_{\text{ch}} \in \mathbb{R}_{>0}$ $[L]$. L_{mfp} is the way a molecule moves between two collisions with other molecules. In the case of Kn $\ll 1$ the continuum assumption holds and thus also the NSE.

- The *Reynolds number* $[-]$,

$$\text{Re} = \frac{T_{\text{diff}}}{T_{\text{adv}}} = \frac{L_{\text{ch}}^2 \,/\, \nu}{L_{\text{ch}} \,/\, U_{\text{ch}}} = \frac{U_{\text{ch}} \, L_{\text{ch}}}{\nu} \tag{2.2}$$

is the ratio of inertial to viscous forces and accordingly relates the time scales of diffusive ($T_{\text{diff}} \in \mathbb{R}_{>0}$ $[T]$) and advective dynamics ($T_{\text{adv}} \in \mathbb{R}_{>0}$ $[T]$). $\nu \in \mathbb{R}_{>0}$ $[L^2 \, T^{-1}]$ is the kinematic viscosity and $U_{\text{ch}} \in \mathbb{R}$ $[L \, T^{-1}]$ is the magnitude of the characteristic macroscopic fluid velocity.

- The *Mach number* $[-]$,

$$\text{Ma} = \frac{T_{\text{s}}}{T_{\text{adv}}} = \frac{L_{\text{ch}} \,/\, c_s}{L_{\text{ch}} \,/\, U_{\text{ch}}} = \frac{U_{\text{ch}}}{c_s} \tag{2.3}$$

relates the time scales of acoustic ($T_{\text{s}} \in \mathbb{R}_{>0}$ $[T]$) and advective dynamics. $c_s \in \mathbb{R}_{>0}$ $[L \, T^{-1}]$ is the speed of sound in the fluid. Normally Ma < 0.3 refers to an incompressible fluid flow [17], Ma ≤ 0.1 to a steady flow of an incompressible fluid.

2.2 Governing equations

2.2.1 Continuity and Navier-Stokes equation for continuous matter

The basic theory of fluid dynamics particularly includes the continuity and the NSE as a direct consequence of the conservation of mass and momentum on the macroscopic scale [18]. The continuity of a fluid refers to the fact that temporal changes in fluid mass within a stationary and arbitrary volume element occur due to fluid flow in or out. It neither arises from nothing nor disappears into it. The continuity equation of an incompressible fluid with constant mass density $\rho \in \mathbb{R}_{>0}$ $[\mathrm{M\,L^{-3}}]$ is given by

$$\nabla \cdot \vec{u} = 0 \qquad \text{in } I \times \Omega \,, \tag{2.4}$$

for the flow velocity $\vec{u} : I \times \Omega \to \mathbb{R}^3$ $[\mathrm{L\,T^{-1}}]$ defined on the domain $\Omega \subseteq \mathbb{R}^3$ and the time interval $I \subseteq \mathbb{R}$. Change of momentum is caused e.g. by flow of momentum into or out of the stationary and arbitrary volume element, by changes of pressure $p : I \times \Omega \to \mathbb{R}_{>0}$ $[\mathrm{M\,L^{-1}\,T^{-2}}]$, by shear stress with dynamic viscosity $\mu \in \mathbb{R}_{>0}$ $[\mathrm{M\,L^{-1}\,T^{-1}}]$ or by an external body force density $\vec{f} : I \times \Omega \to \mathbb{R}^3$ $[\mathrm{M\,L^{-2}\,T^{-2}}]$. The obtained momentum equation is called incompressible NSE:

$$\frac{\partial \rho\,\vec{u}}{\partial t} + (\rho\,\vec{u} \cdot \nabla)\,\vec{u} = -\nabla p + \mu\,\nabla^2\,\vec{u} + \vec{f} \qquad \text{in } I \times \Omega \,. \tag{2.5}$$

It holds for incompressible Newtonian fluids.

2.2.2 Advection-diffusion-reaction equation for dissolved reactive substances

The transport of the mass concentration $c : I \to \mathbb{R}$ $[\mathrm{N\,L^{-3}}]$ of a reactive substance dissolved in water (dilute electrolyte) can be modeled under the assumption of a passive scalar transport. In this case the evolution of the mass concentration in a control volume is modeled by the ADRE,

$$\frac{\partial c}{\partial t} + \nabla \cdot (c\,\vec{u}) = D\,\nabla^2 c + R \qquad \text{in } I \times \Omega \,. \tag{2.6}$$

The velocity $\vec{u}$ is obtained by the NSE in (2.4) and (2.5). $D \in \mathbb{R}_{\geq 0}$ [$L^2\,T-1$] is the homogeneous and isotropic diffusion coefficient. $R : I \times \Omega \to \mathbb{R}$ [$N\,L^{-3}\,T^{-1}$] is a source or sink term and takes into account changes in concentration, for example due to adsorption processes [19, 20].

2.3   Lattice Boltzmann method

The lattice Boltzmann equation (LBE) is the discrete form of the BE in space, time and velocity space such that macroscopic equations e.g. the NSE are correctly recovered upon multiscale analysis. It does not aim to directly solve the BE. The resulting governing equation referred to as LBE consists of two terms, collision and streaming. The method originates from the lattice gas automata. Following the introduction of the LBM, the inclusion of forcing schemes to take into account forces acting on the fluid is presented. This is followed by the turbulence modeling of Smagorinsky-Lilly. The section concludes with the adaptation of LBM to solve the mass transport equations for solutes.

2.3.1   Boltzmann equation for distributions of fluid molecules

The probabilistic behaviour of the distribution of fluid atoms is described by the particle distribution function $f : I \times \Omega \times C \to \mathbb{R}_{\geq 0}$ [$M\,L^{-3}$] in kinetic theory. $C \subset \mathbb{R}^3$ is defined as the velocity space. $f(t, \vec{x}, \vec{c})$ alternatively can be referred to as a density distribution function which corresponds to the particle density at location $\vec{x} \in \Omega$ [L] at time $t \in I$ [T] with particle velocity $\vec{c} \in C$ [$L\,T^{-1}$] [19, 21].

The moments of the density distribution function f provide the connection to the local macroscopic quantities of the fluid. The fluid density ρ is given by the zeroth moment

$$\rho = \int_C f(t, \vec{x}, \vec{c})\,\mathrm{d}\,\vec{c}. \tag{2.7}$$

The first moment gives the macroscopic momentum density

$$\rho\,\vec{u} = \int_C \vec{c}\,f(t, \vec{x}, \vec{c})\,\mathrm{d}\,\vec{c}, \tag{2.8}$$

with $\vec{u} := \vec{u}(t, \vec{x})$. If energy is to be conserved, the internal energy density is given by

$$\rho\,e = \frac{1}{2} \int_C \|\vec{c} - \vec{u}\|^2\,f(t, \vec{x}, \vec{c})\,\mathrm{d}\,\vec{c}, \tag{2.9}$$

with internal energy $e := e(t, \vec{x})$ $[\mathrm{M\,L^2\,T^{-2}}]$ and relative velocity $\vec{v} := \vec{c} - \vec{u}$. This is of importance for non-isothermal flows that are not considered here. The macroscopic pressure

$$p = \frac{1}{3} \int_C \|\vec{c} - \vec{u}\|^2 f(t, \vec{x}, \vec{c}) \, \mathrm{d}\,\vec{c} \tag{2.10}$$

can also be retrieved by a moment of f and is obviously proportional to e, since they are connected by the ideal gas law

$$p = \rho\,R\,T\,, \tag{2.11}$$

with specific gas constant $R = 8.3143\,\mathrm{J\,mol^{-1}\,k^{-1}}$ and temperature T.

To account for changes in ρ, $\vec{u}$, e or p, the evolution of f is indicated by the total differential

$$\frac{\mathrm{d}\,f}{\mathrm{d}\,t} = \frac{\partial\,f}{\partial\,t} + \frac{\mathrm{d}\,\vec{x}}{\mathrm{d}\,t} \cdot \nabla f + \frac{\mathrm{d}\,\vec{c}}{\mathrm{d}\,t} \cdot \nabla_{\vec{c}} f \tag{2.12}$$

with $\nabla = \left(\frac{\partial}{\partial\,x_1}, \frac{\partial}{\partial\,x_2}, \frac{\partial}{\partial\,x_3} \right)$ and $\vec{x} = (x_1, x_2, x_3)$, $\nabla_{\vec{c}} = \left(\frac{\partial}{\partial\,c_1}, \frac{\partial}{\partial\,c_2}, \frac{\partial}{\partial\,c_3} \right)$ and $\vec{c} = (c_1, c_2, c_3)$. Finally, the BE results from (2.12) by replacing $\mathrm{d}\,\vec{x}/\mathrm{d}\,t$ with the particle velocity $\vec{c}$ and $\mathrm{d}\,\vec{c}/\mathrm{d}\,t$ with the force density per (mass) density $\vec{f}/\rho$, respectively [22]:

$$\Omega(f) = \frac{\partial\,f}{\partial\,t} + \vec{c} \cdot \nabla f + \frac{\vec{f}}{\rho} \cdot \nabla_{\vec{c}} f\,. \tag{2.13}$$

Concluding, f evolves by changes because of both advection and forces. The BE is called *force-free* in case the third term to the right of (2.13) is zero with $\vec{f} = 0$.

The collision operator $\Omega(f)$ represents a source term that includes changes caused by particle collisions. The original Boltzmann collision operator considers collisions of just two particles resulting into a complex integral. The most popular and simple formulation of the collision operator in LBE is the Bhatnagar–Gross–Krook (BGK) collision operator,

$$\Omega^{\mathrm{BGK}}(f) = -\frac{1}{\tau_{\mathrm{BE}}} \left(f - f^{\mathrm{eq}} \right) \tag{2.14}$$

as proposed by Bhatnagar, Gross, and Krook [23]. The force-free BGK-BE is given by

$$\frac{\partial\,f}{\partial\,t} + \vec{c} \cdot \nabla f = -\frac{1}{\tau_{\mathrm{BE}}} \left(f - f^{\mathrm{eq}} \right)\,. \tag{2.15}$$

The particles of f collide and relax towards the equilibrium distribution function (EDF) $f^{\mathrm{eq}} : I \times \Omega \times C \to \mathbb{R}_{\geq 0}$ $[\mathrm{M\,L^{-3}}]$ according to the mean free time $\tau_{\mathrm{BE}} \in \mathbb{R}_{>0}$ $[\mathrm{T}]$ of the BE, the average time between two collisions with $\tau_{\mathrm{BE}} = \mu/\rho\,c_s^2$ $[\mathrm{T}]$. The formulation of the

BGK-collision operator is in good agreement with Boltzmann's *H*-theorem which states that the distribution functions of undisturbed fluids tend towards the EDF. In addition, mass, momentum and energy are conserved. Further information about the Boltzmann *H*-theorem can be found, for example, in [24].

The Maxwell-Boltzmann distribution, the basis of the EDF, was first described by James Clerk Maxwell and later derived from statistical mechanics by Ludwig Boltzmann, and is given by

$$
\begin{aligned}
f^{\text{eq}}(t, \vec{x}, \vec{c}) &= \rho \left(\frac{\rho}{2 \pi p} \right)^{3/2} \exp \left(-\frac{p \, \|\vec{c} - \vec{u}\|^2}{2 \, \rho} \right) \\
&= \rho \left(\frac{1}{2 \pi R T} \right)^{3/2} \exp \left(-\frac{\|\vec{c} - \vec{u}\|^2}{2 R T} \right).
\end{aligned}
\tag{2.16}
$$

f^{eq} also satisfies the moments in (2.7), (2.8), (2.9) and (2.10).

2.3.2 Lattice Boltzmann equation

To obtain the LBE from the continuous formulation of the BE, the discretization of velocity, time and space is necessary. In the case of the LBE the choice of the collision term and the equilibrium distribution function are less restrictive as the goal is to rather recover the macroscopic equations correctly through multiscale analysis. In this thesis, the Chapman-Enskog multiscale analysis is used to demonstrate the validity of the LBE for solving the governing equations.

Velocity discretization

The purpose of velocity discretization is to limit the continuous velocity space to a finite number of discrete velocities. The discrete velocity set $\{\vec{c}_i\} \in C \, [\text{L} \, \text{T}^{-1}]$ replaces the continuous velocity set $\vec{c}$. The velocities $\vec{c}_i$ are chosen to ensure that a fluid particle reaches the next node within one time step. Thus $\vec{c}_i$ is approximately in the same order of magnitude as the speed of sound:

$$
\mathcal{O}(c) \approx \mathcal{O}(c_s) \approx \mathcal{O}(\|\vec{c}_i\|) \qquad \text{with} \qquad c := \Delta x / \Delta t \, .
\tag{2.17}
$$

with the time step $\Delta t \in \mathbb{R}_{>0} \, [\text{T}]$ and the given lattice spacing $\Delta x \in \mathbb{R}_{>0} \, [\text{L}]$.

The correctness of the macroscopic conservation laws is ensured by the discrete velocities and a simplified representation of the EDF. For the classical LBE model, the representation of f^{eq} in (2.16) by a simplified version is done by a Taylor expansion,

$$
\begin{aligned}
f^{\mathrm{eq}}(t, \vec{x}, \vec{c}_i) &= \frac{\rho}{(2\pi RT)^{3/2}} \exp\left(-\frac{\|\vec{c}_i - \vec{u}\|^2}{2\,RT}\right) \\
&= \frac{\rho}{(2\pi RT)^{3/2}} \exp\left(-\frac{\|\vec{c}_i\|^2}{2\,RT}\right) \exp\left(\frac{\vec{c}_i \cdot \vec{u}}{RT} - \frac{\|\vec{u}\|^2}{2\,RT}\right) \\
&= \frac{\rho}{(2\pi RT)^{3/2}} \exp\left(-\frac{\|\vec{c}_i\|^2}{2\,RT}\right) \left(1 + \frac{\vec{c}_i \cdot \vec{u}}{RT} - \frac{\|\vec{u}\|^2}{2\,RT} + \frac{(\vec{c}_i \cdot \vec{u})^2}{2\,(RT)^2} + \mathcal{O}(\vec{u}^3)\right) \\
&\approx \rho\, w(\vec{c}_i) \left(1 + \frac{\vec{c}_i \cdot \vec{u}}{c_s^2} - \frac{\|\vec{u}\|^2}{2\,c_s^2} + \frac{(\vec{c}_i \cdot \vec{u})^2}{2\,c_s^4}\right),
\end{aligned}
\tag{2.18}
$$

for constant temperature and low Mach-number approximation with a discrete velocity $\vec{c}_i$ and $w(\vec{c}_i) = (2\pi c_s^2)^{-3/2} \exp\left(-\|\vec{c}_i\|^2 / 2\,c_s^2\right)$ [25, 26]. A low Mach-number (2.3) means that the characteristic flow velocity U_{ch} is much smaller than the speed of sound $c_s = \sqrt{RT}$, resulting in $\mathrm{Ma} \ll 1$. $\mathcal{O}(\vec{u}^3)$ contains the terms of $\vec{u}$ which are larger than second order [27]. According to (2.3), the terms of the Taylor expansion up to $\mathcal{O}(\mathrm{Ma}^2)$ are given. To solve the NSE, f^{eq} must fulfill the conservation of mass and momentum. Terms up to second order of $\vec{u}$ are sufficient for this. For the prevailing equations of the concentration transport, terms only up to first order of $\vec{u}$ are required.

The hydrodynamic moments of f^{eq}, (2.7) and (2.8), must hold for the discrete velocities. For this purpose the integrals are replaced by sums. In case of a polynomial $P^{(N)}$ of order N, the integral is solved by the Gauss-Hermite quadrature rule

$$
\int_{-\infty}^{\infty} \exp(-\vec{x}^2)\, P^{(N)}(\vec{x})\, \mathrm{d}\vec{x} = \sum_{i=0}^{q_f-1} w_i\, P^{(N)}(\vec{x}_i),
\tag{2.19}
$$

with at least $q_f = n^d$ discrete directions $\vec{c}_i$ and associated weights w_i given by the Hermite polynomials, $n \geq (N+1)/2$, $n \in \mathbb{N}$, the dimension d and $i = 0, \ldots, q_f - 1$. Following Krüger et al. [19], $P^{(N)}$ is a combination of f^{eq} and Hermite polynomials leading to a polynomial of at least fifth order in $\vec{c}$. The number of necessary directions or weights of the Gauss-Hermite quadrature is thus known, and the appropriate velocity set can be chosen so that [17]

$$
\rho = \int_C f^{\mathrm{eq}}(t, \vec{x}, \vec{c})\, \mathrm{d}\vec{c} = \sum_{i=0}^{q_f-1} f_i^{\mathrm{eq}}(t, \vec{x}),
\tag{2.20}
$$

and

$$\rho\,\vec{u}\,(t,\vec{x}) = \int_C \vec{c}\,f^{\text{eq}}(t,\vec{x},\vec{c})\,\mathrm{d}\,\vec{c} = \sum_{i=0}^{q_f-1} \vec{c}_i\,f_i^{\text{eq}}(t,\vec{x})\,. \tag{2.21}$$

The EDF in (2.18) is expressed by the discrete equilibrium distribution function

$$f_i^{\text{eq}}(t,\vec{x}) = f^{\text{eq}}(t,\vec{x},\vec{c}_i)\,. \tag{2.22}$$

with $f_i^{\text{eq}} : I_h \times \Omega_h \to \mathbb{R}_{>0}$ on the uniform lattice $\Omega_h \subset \Omega$ with a given lattice spacing Δx, and discrete time space $I_h \subset I$ with a discrete time step Δt and resolution $h \in \mathbb{N}$. The density distribution function f that is assumed to solve (2.15) is discretized in the same manner. Its discrete form $f_i : I_h \times \Omega_h \to \mathbb{R}_{>0}$ is obtained by

$$f_i\,(t,\vec{x}) = \frac{w_i}{w(\vec{c}_i)}\,f(t,\vec{x},\vec{c}_i)\,. \tag{2.23}$$

It meets the expectations regarding the moments in (2.20) and (2.21) by replacing f^{eq} by f and f_i^{eq} by f_i. Finally, the force-free discrete velocity BGK-BE is

$$\frac{\partial\,f_i}{\partial\,t} + \vec{c}_i \cdot \nabla f_i = -\frac{1}{\tau_{\text{BE}}}\,(f_i - f_i^{\text{eq}})\,. \tag{2.24}$$

The maximum number of directions or weights required in two-dimensional case (2D) is $q_f = 9$, in three-dimensional case (3D) $q_f = 27$. Due to concerns in symmetry, only even-order terms are considered in (2.19). Odd order terms disappear, reducing D3Q27 to e.g. D3Q19 [28]. In the following, a way to determine w_i, $\vec{c}_i$ and c_s of a velocity quantity is shown, which is similar to [29], [30] and [31]. From (2.20) follows

$$\begin{aligned}
\rho &= \sum_{i=0}^{q_f-1} f_i^{\text{eq}} \\
&= \rho\left[\sum_{i=0}^{q_f-1} w_i + \frac{u_\alpha}{c_s^2}\sum_{i=0}^{q_f-1} w_i\,c_{i,\alpha} + \frac{u_\alpha\,u_\beta}{2\,c_s^2}\left(\frac{1}{c_s^2}\sum_{i=0}^{q_f-1} w_i\,c_{i,\alpha}\,c_{i,\beta} - \delta_{\alpha\beta}\sum_{i=0}^{q_f-1} w_i\right)\right],
\end{aligned} \tag{2.25}$$

in index instead of vector notation due to less complexity of mathematical depiction. The indices α, β, γ, δ refer to a vector component and can be either identical or different. $\delta_{\alpha\beta}$ is the Kronecker delta symbol with $\delta_{\alpha\beta} = 1$ when $\alpha = \beta$ and $\delta_{\alpha\beta} = 0$ when $\alpha \neq \beta$. Odd-order terms in $\vec{c}_i$ disappear for symmetric lattices such as those used here. The constraints below

result from the problem that the term in the square brackets in (2.25) must be 1. For $w_i > 0$ it is

$$\sum_{i}^{q_f-1} w_i = 1\,,$$

$$\sum_{i}^{q_f-1} w_i\, c_{i,\alpha} = 0\,, \tag{2.26}$$

$$\sum_{i}^{q_f-1} w_i\, c_{i,\alpha}\, c_{i,\beta} = c_s^2\, \delta_{\alpha\beta}\,.$$

For advection-diffusion problems the conservation of momentum is not necessary, hence the moments of the weights up to second order are sufficient, as given in (2.26). The lattice stencil D2Q5 is appropriate and meets the constraints, Table 2.1. For Navier-Stokes problems, the first and second moment of f_i^{eq} lead to further limitations:

$$\sum_{i}^{q_f-1} w_i\, c_{i,\alpha}\, c_{i,\beta}\, c_{i,\gamma} = 0\,,$$

$$\sum_{i}^{q_f-1} w_i\, c_{i,\alpha}\, c_{i,\beta}\, c_{i,\gamma}\, c_{i,\delta} = c_s^4\,(\delta_{\alpha\beta}\,\delta_{\gamma\delta} + \delta_{\alpha\gamma}\,\delta_{\beta\delta} + \delta_{\alpha\delta}\,\delta_{\beta\gamma})\,. \tag{2.27}$$

Using the example of D2Q9, the corresponding weights w_i, the velocities $\vec{c}_i$ and the corresponding speed of sound c_s are evaluated in accordance with (2.26) and (2.27). In general, $\vec{c}_0 = \vec{0}$ is the zero velocity vector for particles that do not change the lattice node. The velocity vectors $\vec{c}_1$, $\vec{c}_2$, $\vec{c}_3$, $\vec{c}_4$ point in the directions parallel to the directions in the plane and have the order $c = \Delta x/\Delta t$ as described in Table 2.2. The remaining velocity vectors $\vec{c}_5$, $\vec{c}_6$, $\vec{c}_7$, $\vec{c}_8$ are diagonals of the size $\sqrt{2}\,c$. Since the weights assigned to the velocity directions of identical size are identical for reasons of symmetry, the weights w_a, w_b and $w_c > 0$ are introduced as

$$w_a = w_0\,,$$

$$w_b = w_1 = w_2 = w_3 = w_4\,,$$

$$w_c = w_5 = w_6 = w_7 = w_8\,.$$

Thus the final number of unknown weights is reduced to three. From the non-zero constraints follows

$$1 = \sum_i^{q_f-1} w_i = w_a + 4\,w_b + 4\,w_c \,,$$

$$c_s^2 = \sum_i^{q_f-1} w_i\,c_{i,1}^2 = \sum_i^{q_f-1} w_i\,c_{i,2}^2 = c^2\,(2\,w_b + 4\,w_c)\,,$$

$$c_s^4 = \sum_i^{q_f-1} w_i\,c_{i,1}^2\,c_{i,2}^2 = c^4\,4\,w_c\,,$$

$$3\,c_s^4 = \sum_i^{q_f-1} w_i\,c_{i,1}^4 = \sum_i^{q_f-1} w_i\,c_{i,2}^4 = c^4\,(2\,w_b + 4\,w_c)\,.$$

This results in $c = \sqrt{3}\,c_s$, $w_a = \frac{4}{9}$, $w_b = \frac{1}{9}$ and $w_c = \frac{1}{36}$.

Table 2.1 to Table 2.4 give the associated speed of sound c_s, the weights w_i and the velocity vectors $\vec{c}_i$ of the lattice stencils D2Q5, D2Q9, D3Q7 and D3Q19 with $\vec{c}_i \in \{-c, 0, c\}^d$, $c := \Delta x / \Delta t$. In 2D it is $\vec{c}_i = (c_{i,1}, c_{i,2})$, in 3D it is $\vec{c}_i = (c_{i,1}, c_{i,2}, c_{i,3})$. Exemplary, the D3Q19 stencil is given in Figure 2.1.
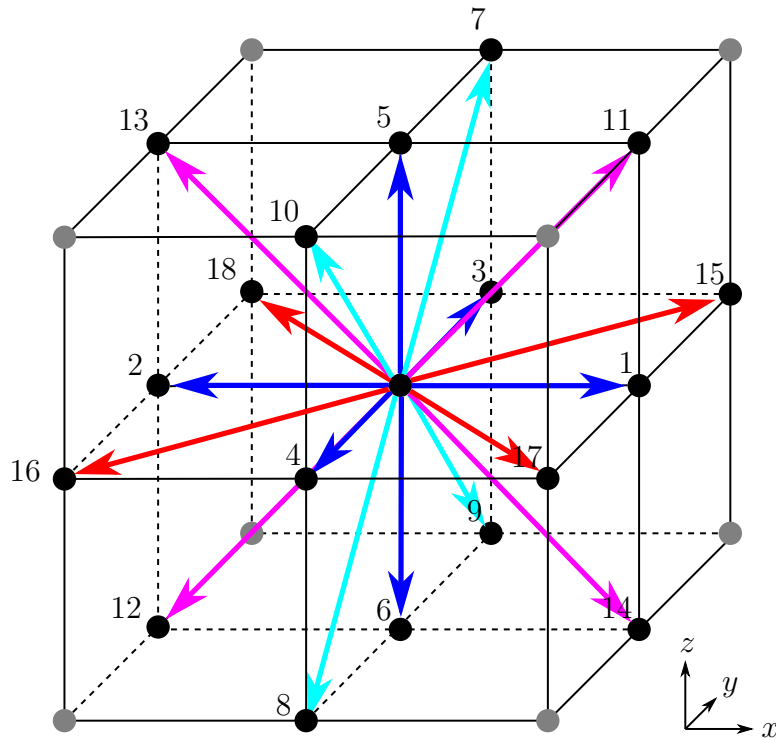

Figure 2.1: Schematic depiction of the D3Q19 stencil. The numbers represent the index i of the velocity vectors $\vec{c}_i$.

i	0	1	2	3	4
w_i	$\frac{1}{3}$	$\frac{1}{6}$	$\frac{1}{6}$	$\frac{1}{6}$	$\frac{1}{6}$
$c_{i,1}$	0	c	0	-c	0
$c_{i,2}$	0	0	c	0	-c
$\|\vec{c}_i\|$	0	c	c	c	c

Table 2.1: In the D2Q5 lattice stencil, $c_s = \frac{c}{\sqrt{3}}$. There are just lattice velocities in orthogonal direction of length c. This lattice stencil fits for advection-diffusion problems [19].

i	0	1	2	3	4	5	6	7	8
w_i	$\frac{4}{9}$	$\frac{1}{9}$	$\frac{1}{9}$	$\frac{1}{9}$	$\frac{1}{9}$	$\frac{1}{36}$	$\frac{1}{36}$	$\frac{1}{36}$	$\frac{1}{36}$
$c_{i,1}$	0	c	0	-c	0	c	-c	-c	c
$c_{i,2}$	0	0	c	0	-c	c	c	-c	$-c$
$\|\vec{c}_i\|$	0	c	c	c	c	$\sqrt{2}c$	$\sqrt{2}c$	$\sqrt{2}c$	$\sqrt{2}c$

Table 2.2: In the D2Q9 lattice stencil, $c_s = \frac{c}{\sqrt{3}}$ [13, 17]. The lattice velocities in orthogonal direction are of length c, the ones in diagonal direction are of length $\sqrt{2}\,c$ [31, 32].

i	0	1	2	3	4	5	6
w_i	$\frac{1}{4}$	$\frac{1}{8}$	$\frac{1}{8}$	$\frac{1}{8}$	$\frac{1}{8}$	$\frac{1}{8}$	$\frac{1}{8}$
$c_{i,1}$	0	c	0	0	-c	0	0
$c_{i,2}$	0	0	c	0	0	-c	0
$c_{i,3}$	0	0	0	c	0	0	-c
$\|\vec{c}_i\|$	0	c	c	c	c	c	c

Table 2.3: In the D3Q7 lattice stencil, $c_s = \frac{c}{\sqrt{3.5}}$ and the lattice velocities in orthogonal direction are of length c [13]. This lattice stencil fits for advection-diffusion problems.

i	0	1	2	3	4	5	6	7	8	9	10	11	12	13	14	15	16	17	18
w_i	$\frac{1}{3}$	$\frac{1}{18}$	$\frac{1}{18}$	$\frac{1}{18}$	$\frac{1}{18}$	$\frac{1}{18}$	$\frac{1}{18}$	$\frac{1}{36}$	$\frac{1}{36}$	$\frac{1}{36}$	$\frac{1}{36}$	$\frac{1}{36}$	$\frac{1}{36}$	$\frac{1}{36}$	$\frac{1}{36}$	$\frac{1}{36}$	$\frac{1}{36}$	$\frac{1}{36}$	$\frac{1}{36}$
$c_{i,1}$	0	c	-c	0	0	0	0	0	0	0	0	c	-c	-c	c	c	-c	c	-c
$c_{i,2}$	0	0	0	c	-c	0	0	c	-c	c	-c	0	0	0	0	c	-c	-c	c
$c_{i,3}$	0	0	0	0	0	c	-c	c	-c	-c	c	c	c	-c	c	-c	0	0	0	0
$\|\vec{c}_i\|$	0	c	c	c	c	c	c	$\sqrt{2}c$	$\sqrt{2}c$	$\sqrt{2}c$	$\sqrt{2}c$	$\sqrt{2}c$	$\sqrt{2}c$	$\sqrt{2}c$	$\sqrt{2}c$	$\sqrt{2}c$	$\sqrt{2}c$	$\sqrt{2}c$	$\sqrt{2}c$

Table 2.4: In the D3Q19 lattice stencil, $c_s = \frac{c}{\sqrt{3}}$ [17]. In addition, the lattice velocities in orthogonal direction are of length c, the ones in diagonal direction are of length $\sqrt{2}\,c$.

Time and space discretization

From the common $DdQq_f$ lattice stencils it is already known that in most cases the underlying lattice of the LBM is uniform, regular and structured [19]. The force-free discrete velocity BGK-BE (2.24) is an ordinary differential equation

$$\frac{\mathrm{d}\, f_i\,(t,\vec{x})}{\mathrm{d}\, t} = \frac{\partial\, f_i\,(t,\vec{x})}{\partial\, t} + \vec{c}_i \cdot \nabla f_i\,(t,\vec{x})\;. \tag{2.28}$$

According to He and Luo [33] and Krüger et al. [19] the integration of the above equation over the time step Δt using the method of characteristics results in

$$f_i(t+\Delta t, \vec{x}+\vec{c}_i\,\Delta t) = \exp\left(\frac{-\Delta t}{\tau_{\mathrm{BE}}}\right)\left(\frac{1}{\tau_{\mathrm{BE}}}\int_0^{\Delta t}\exp\left(\frac{t'}{\tau_{\mathrm{BE}}}\right)f_i^{\mathrm{eq}}(t+t', \vec{x}+\vec{c}_i\,t')\,\mathrm{d}\,t' + f_i\,(t,\vec{x})\right), \tag{2.29}$$

with $t' \le \Delta t$. Assuming that Δt is small and f_i^{eq} is sufficiently smooth, and additionally a forward Euler method (first order approximation) is chosen, the integral is replaced and it follows

$$f_i(t + \Delta t, \vec{x} + \vec{c}_i\,\Delta t) = \exp\left(\frac{-\Delta t}{\tau_{\mathrm{BE}}}\right)f_i(t,\vec{x}) + \frac{\exp\left(-\Delta t/\tau_{\mathrm{BE}}\right)}{\tau_{\mathrm{BE}}}f_i^{\mathrm{eq}}\,(t,\vec{x})\,\Delta t\,, \tag{2.30}$$

whereas terms of $\mathcal{O}(\Delta t^2)$ are neglected. The extension of $\exp\left(-\Delta t/\tau_{\mathrm{BE}}\right)$ by Taylor and keeping terms up to $\mathcal{O}(\Delta t)$ gives

$$f_i(t + \Delta t, \vec{x} + \vec{c}_i\,\Delta t) = \left(1 - \frac{\Delta t}{\tau_{\mathrm{BE}}}\right)f_i(t,\vec{x}) + \frac{\Delta t}{\tau_{\mathrm{BE}}}f_i^{\mathrm{eq}}\,(t,\vec{x}) + \mathcal{O}(\Delta t^2)\,. \tag{2.31}$$

Using the Chapman-Enskog extension it can be shown that the resulting scheme recovers both the continuity and the Navier-Stokes equation. The second-order scheme is accurate in space and time by simply changing the relaxation time τ_{BE} by $\Delta t/2$ [29, 31, 34, 35]:

$$\tau = \tau_{\mathrm{BE}} + \Delta t/2 = \mu/\rho\,c_s^2 + \Delta t/2\,. \tag{2.32}$$

This results in the final spatially and temporally discrete form of (2.24).

Lattice Boltzmann equation

The LBE is the discrete form of the BE and depends on a discrete velocity, position and time space. The discrete form of the isothermal and force-free BE is given here:

$$f_i(t + \Delta t, \vec{x} + \vec{c}_i \, \Delta t) = f_i(t, \vec{x}) - \Delta t \, \Omega_i \, (t, \vec{x}) \,, \tag{2.33}$$

for $t \in I_h$ and for $\vec{x} \in \Omega_h$. The discrete BGK collision term is

$$\Omega_i^{\mathrm{BGK}}(t, \vec{x}) = \frac{1}{\tau} \, (f_i(t, \vec{x}) - f_i^{\mathrm{eq}}(t, \vec{x})) \tag{2.34}$$

and is used in single relaxation time (SRT) methods. The SRT LBM scheme is the most commonly used model due to its simplicity and efficiency. However, its accuracy and stability that depend on the viscosities for fluid flows respective on the diffusivity for mass transport is reduced. For small diffusivity, the time steps are small and therefore it is computationally inefficient. The particles collide and relax in the direction of the discrete EDF $f_i^{\mathrm{eq}} : I_h \times \Omega_h \rightarrow \mathbb{R}_{\geq 0}$ according to the relaxation time $\tau = \mu/(\rho \, c_s^2) + \Delta t/2$ with

$$f_i^{\mathrm{eq}}(t, \vec{x}) = w_i \, \rho \left(1 + \frac{\vec{c}_i \cdot \vec{u}}{c_s^2} - \frac{\vec{u} \cdot \vec{u}}{2 \, c_s^2} + \frac{(\vec{c}_i \cdot \vec{u})^2}{2 \, c_s^4} \right). \tag{2.35}$$

c_s and the weights $w_i \in \mathbb{R}_{>0}$ depend on the underlying lattice stencil DdQq_f. f_i^{eq} must fulfill the requirements for the moments of the distribution function just like f_i. In the discrete case the macroscopic quantities are given by

$$\rho = \sum_i f_i^{\mathrm{eq}}(t, \vec{x}) = \sum_i f_i(t, \vec{x}) \,, \tag{2.36}$$

$$\rho \, \vec{u} \, (t, \vec{x}) = \sum_i \vec{c}_i \, f_i^{\mathrm{eq}}(t, \vec{x}) = \sum_i \vec{c}_i \, f_i(t, \vec{x}) \,. \tag{2.37}$$

Using the Chapman-Enskog analysis, the NSE is recovered from the LBM [26, 31, 36].

Chapman-Enskog analysis

To recover the governing equations from the LBE, the multiscale analysis of Chapman-Enskog is used as proposed in [19, 26, 31, 36]. First, the left hand side of (2.33) with (2.34) is expanded by a Taylor series

$$f_i(t + \Delta t, \vec{x} + \vec{c}_i \, \Delta t) = \sum_{n=0}^{\infty} \frac{(\Delta t \, D_{t,i})^n}{n!} \, f_i(t, \vec{x}) \,, \tag{2.38}$$

with $D_{t,i} = \left(\frac{\partial}{\partial t} + \vec{c}_i \cdot \nabla \right)$. Using only the terms up to the second order, $n = 0, 1, 2$, and including them in (2.33) gives

$$\Delta t \, D_{t,i} \, f_i(t, \vec{x}) + \frac{\Delta t^2}{2} \, D_{t,i}^2 \, f_i(t, \vec{x}) = -\frac{\Delta t}{\tau} \left(f_i(t, \vec{x}) - f_i^{\mathrm{eq}}(t, \vec{x}) \right) + \mathcal{O}(\Delta t^3) \,. \tag{2.39}$$

Assuming f_i is a solution of the LBE with respect to a small perturbation $\epsilon \approx \mathrm{Kn}$. The expansion of the perturbation of f_i around the equilibrium distribution f_i^{eq} is given by a power series of ϵ and non-equilibrium distribution functions $f_i^{(n)}$ with small deviation from equilibrium,

$$f_i(t, \vec{x}) = f_i^{\mathrm{eq}}(t, \vec{x}) + \epsilon \, f_i^{(1)}(t, \vec{x}) + \epsilon^2 \, f_i^{(2)}(t, \vec{x}) + \mathcal{O}(\epsilon^3) \,. \tag{2.40}$$

This perturbation does not affect the mass and momentum density, it is

$$\sum_i f_i^{(1)}(t, \vec{x}) = 0 \,, \qquad \text{respective} \qquad \sum_i f_i^{(2)}(t, \vec{x}) = 0 \,, \tag{2.41}$$

$$\sum_i \vec{c}_i \, f_i^{(1)}(t, \vec{x}) = 0 \,, \qquad \text{respective} \qquad \sum_i \vec{c}_i \, f_i^{(2)}(t, \vec{x}) = 0 \,. \tag{2.42}$$

The time deviation is expanded by the convective scale $t^{(1)}$ and the diffusive scale $t^{(2)}$,

$$\frac{\partial}{\partial t} = \epsilon \, \frac{\partial}{\partial t^{(1)}} + \epsilon^2 \frac{\partial}{\partial t^{(2)}} + \mathcal{O}(\epsilon^3) \,. \tag{2.43}$$

For the spatial expansion only a macroscopic scale is considered, since macroscopic processes like advection and diffusion occur on similar spatial scales [31]. It is depicted by

$$\frac{\partial}{\partial x_\alpha} = \epsilon \, \frac{\partial}{\partial x_\alpha^{(1)}} + \mathcal{O}(\epsilon^2) \,, \qquad \text{and} \qquad \nabla^{(1)} = \left(\frac{\partial}{\partial x_1^{(1)}}, \dots, \frac{\partial}{\partial x_d^{(1)}} \right) \tag{2.44}$$

for $\alpha = 1, \dots, d$.

Omitting terms of higher order than three, inserting (2.40), (2.43), (2.44) into (2.39) and splitting the latter into terms of different order in ϵ results in

$$\mathcal{O}(\epsilon^1): \qquad \left(\frac{\partial}{\partial t^{(1)}} + \vec{c}_i \cdot \nabla^{(1)} \right) f_i^{\text{eq}} = -\frac{1}{\tau} f_i^{(1)} , \qquad (2.45)$$

$$\mathcal{O}(\epsilon^2): \qquad \frac{\partial}{\partial t^{(2)}} f_i^{\text{eq}} + \left(\frac{\partial}{\partial t^{(1)}} + \vec{c}_i \cdot \nabla^{(1)} \right) \left(1 - \frac{\Delta t}{2\tau} \right) f_i^{(1)} = -\frac{1}{\tau} f_i^{(2)} . \qquad (2.46)$$

The conservation of mass and momentum is preserved by the moments of (2.45) and (2.46). The zeroth and first moment of (2.45) for $\mathcal{O}(\epsilon)$ results in the continuity and the Euler equation (no friction) [31]:

$$\frac{\partial \rho}{\partial t^{(1)}} + \nabla^{(1)} \cdot \rho \vec{u} = 0 , \qquad (2.47)$$

$$\frac{\partial \rho \vec{u}}{\partial t^{(1)}} + \nabla^{(1)} \cdot \Pi^{\text{eq}} = 0 , \qquad (2.48)$$

with the zero-order momentum flux tensor $\Pi_{\alpha\beta}^{\text{eq}} = \sum_i c_{i,\alpha} c_{i,\beta} f_i^{\text{eq}} = \rho u_\alpha u_\beta + p \delta_{\alpha\beta}$ and pressure $p = c_s^2 \rho$ [26]. Similar, the first and second order moments of (2.46) for $\mathcal{O}(\epsilon^2)$ lead to

$$\frac{\partial \rho}{\partial t^{(2)}} = 0 , \qquad (2.49)$$

$$\frac{\partial \rho \vec{u}}{\partial t^{(2)}} + \left(1 - \frac{\Delta t}{2\tau} \right) \nabla^{(1)} \cdot \Pi^{(1)} = 0 , \qquad (2.50)$$

with the first-order momentum flux tensor $\Pi_{\alpha\beta}^{(1)} = \sum_i c_{i,\alpha} c_{i,\beta} f_i^{(1)}$. $\Pi_{\alpha\beta}^{(1)}$ is obtained by the second moment of (2.45),

$$\Pi_{\alpha\beta}^{(1)} = -\tau c_s^2 \rho \left(\frac{\partial u_\beta}{\partial x_\alpha^{(1)}} + \frac{\partial u_\alpha}{\partial x_\beta^{(1)}} \right) . \qquad (2.51)$$

Here the terms $\mathcal{O}(\vec{u}^3)$ and $\vec{u} \cdot \nabla \rho$ have been neglected, since they must be consistent with the expansion of f_i^{eq} and $\mathcal{O}(\vec{u}^2)$. By inserting (2.51) into (2.50) and reversing the derivative expansion, the compressible continuity and NSE are obtained with $\mu = \rho c_s^2 (\tau - \frac{\Delta t}{2})$. In case of small Mach numbers, Ma $\to 0$, the incompressible NSE are finally obtained with an accuracy in the order of $\mathcal{O}(\vec{u}^2)$ in (2.4) and $\mathcal{O}(\vec{u}^3)$ in (2.5).

2.3.3   Lattice Boltzmann method

The LBE in (2.33) can be divided into two subsequent steps. During the *collision step*

$$f_i^{\text{collision}}(t, \vec{x}) = f_i(t, \vec{x}) - \Delta t \, \Omega_i (t, \vec{x}) \ , \tag{2.52}$$

the particles collide and f_i is redistributed to the discrete velocity directions $\vec{c}_i$ depending on the collision operator Ω_i. The post-collision distribution is given by $f_i^{\text{collision}}$. The collision is completely local on each node, information exchange with other nodes is not necessary. In the subsequent *streaming step*, $f_i^{\text{collision}}$ is propagated to the nearest neighbor node $\vec{x} + \vec{c}_i \, \Delta t$ in the corresponding direction $\vec{c}_i$ while time is progressing:

$$f_i(t + \Delta t, \vec{x} + \vec{c}_i \, \Delta t) = f_i^{\text{collision}} (t, \vec{x}) \ . \tag{2.53}$$

Such collide-stream approach provides LBM an inherent parallelization to the LBE algorithm.

There are several approaches to initialize the discrete density distribution functions f_i. In this thesis, the distribution functions are initialized using equilibrium density functions from initial macroscopic quantities. Boundary conditions are important and will be discussed later in this thesis.

Convergence and accuracy of the scheme

To guarantee the accuracy of the macroscopic equations even in the case of a change in the grid resolution, restrictions for Δx and Δt are given by the so-called diffusive (or parabolic) scaling. The diffusive scaling describes their relation by $\Delta x^2 \propto \Delta t$. By doubling the grid resolution, the new grid scale is half of the previous scale: $\Delta x' = \Delta x/2$, and the new discrete time step is a quarter of the previous time step: $\Delta t' = \Delta t/4$.

2.3.4   Boundary conditions

The boundary conditions in LBM are different from the boundary conditions used in conventional numerical techniques. Instead of the macroscopic quantities (pressure, velocity) the unknown mesoscopic quantities (distribution functions) need to be specified at the boundary. In case of a fluid-solid boundary, the incoming links are to be reconstructed, since they are not updated during the streaming step.
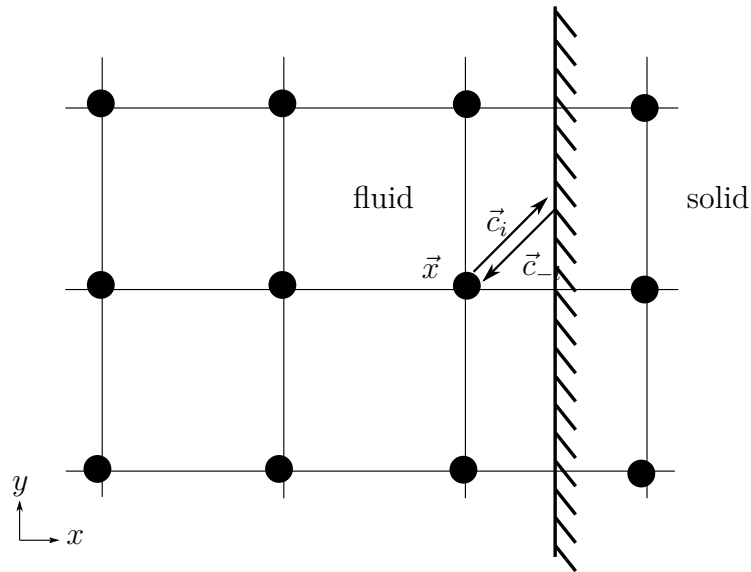
Figure 2.2: Schematic depiction of the half-way bounce-back boundary condition.

The lattice Boltzmann equivalent of a no-slip boundary condition (zero velocity) is the bounce-back condition as proposed by Zou and He [37], see also [17, 30, 36]. It follows the idea that the fluid particles hitting the boundary are reflected. This results in

$$f_i = f_{-i} \, . \tag{2.54}$$

If the boundary is exactly in the middle between fluid and solid nodes it is second order accurate in space [37], Figure 2.2.

An equivalent to the Dirichlet boundary condition with fixed value for e.g. velocity, pressure or concentration is proposed by the Zou-He boundary conditions [37]. It is based on the already described half-way bounce-back boundary conditions. In the following, the velocity boundary condition is derived in 2D for a given boundary velocity $\vec{u} = (u_1, \, u_2) \in \mathbb{R}^2$. The fluid nodes next to the boundary and the streaming directions $\vec{c}_0, \, \ldots, \, \vec{c}_8$ are schematically depicted in Figure 2.3. After the streaming step, the density distribution functions f_0, f_1, f_3, f_4, f_7, f_8 are known, whereas f_2, f_5, f_6 are to be determined. As (2.36) and (2.37) are to be satisfied, it is

$$f_2 + f_5 + f_6 = \rho - (f_0 + f_1 + f_3 + f_4 + f_7 + f_8) \, , \tag{2.55}$$

$$f_5 - f_6 = \rho \, u_1 - (f_1 - f_3 - f_7 + f_8) \, , \tag{2.56}$$

$$f_2 + f_5 + f_6 = \rho \, u_2 + (f_4 + f_7 + f_8) \, . \tag{2.57}$$

Using (2.55) and (2.57) gives

$$\rho = \frac{1}{1 - u_2} \Big(f_0 + f_1 + f_3 + 2 \left(f_4 + f_7 + f_8 \right) \Big). \tag{2.58}$$

Assuming that the bounce-back rule for the non-equilibrium part is correct for the flow directions perpendicular to the boundary ($f_2 - f_2^{\text{eq}} = f_4 - f_4^{\text{eq}}$), f_2, f_5 and f_6 are obtained:

$$f_2 = f_4 + \frac{2}{3} \rho \, u_2 \,, \tag{2.59}$$

$$f_5 = f_7 - \frac{1}{2} \left(f_1 - f_3 \right) + \frac{1}{2} \rho \, u_1 + \frac{1}{6} \rho \, u_2 \,, \tag{2.60}$$

$$f_6 = f_8 + \frac{1}{2} \left(f_1 - f_3 \right) - \frac{1}{2} \rho \, u_1 + \frac{1}{6} \rho \, u_2 \,. \tag{2.61}$$

The subsequent collision step is applied to both the fluid and the boundary nodes. In a similar manner, the pressure boundary condition is derived, see Zou and He [37]. Due to the connection of the density ρ and the pressure p by the speed of sound c_s,

$$p = c_s^2 \, \rho \,, \tag{2.62}$$

$c_s = \sqrt{RT}$ [33, 38], ρ serves as a reference value for the pressure p.
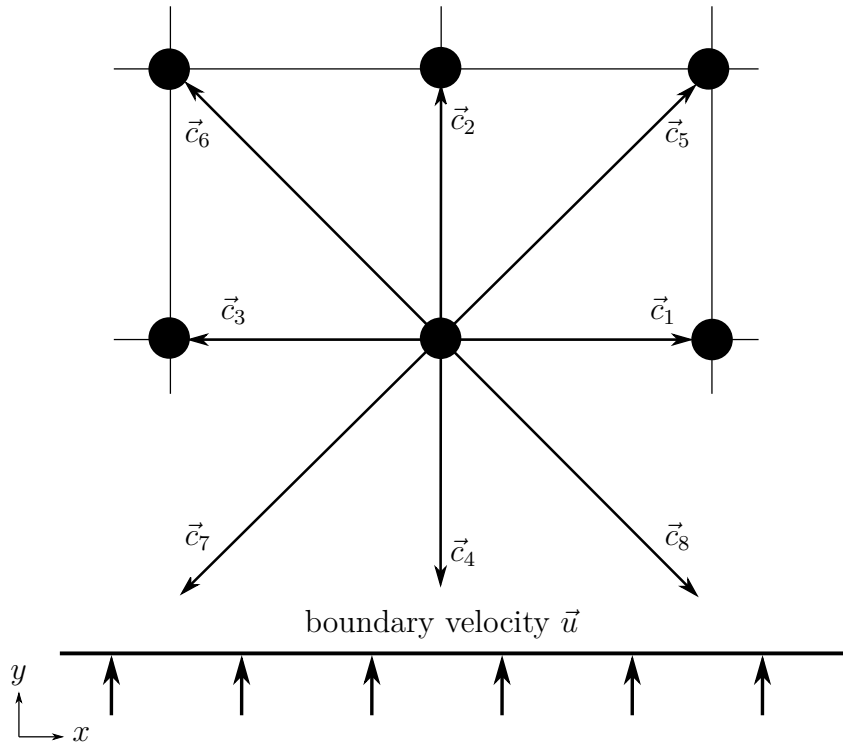

Figure 2.3: Schematic depiction of the velocity boundary condition.

For the mass transport of e.g. a reactive substance, an outlet boundary condition is chosen to obtain the missing distribution functions at the boundary nodes $\vec{x}_{\text{boundary}}$. They are evaluated by interpolating the neighboring nodes in the direction of the unit normal vector $\vec{n} \in \mathbb{R}^3$, pointing to the interior of the domain:

$$f_i(\vec{x}_{\text{boundary}},\, t) = 0.5 \left(f_i(\vec{x}_{\text{boundary}} + \vec{n}\,\Delta t) + f_i(\vec{x}_{\text{boundary}} + 2\,\vec{n}\,\Delta t) \right). \tag{2.63}$$

This interpolation holds approximately the following conditions

$$\frac{\partial\,\rho\,\vec{u}}{\partial\,\vec{n}} = 0 \qquad \text{and} \qquad \frac{\partial\,\rho}{\partial\,\vec{n}} = 0\,. \tag{2.64}$$

Thus, the Neumann boundary conditions are inferred:

$$0 = \frac{\partial\,\rho\,\vec{u}}{\partial\,\vec{n}} = \vec{u}\,\frac{\partial\,\rho}{\partial\,\vec{n}} + \rho\frac{\partial\,\vec{u}}{\partial\,\vec{n}} = \rho\frac{\partial\,\vec{u}}{\partial\,\vec{n}}\,. \tag{2.65}$$

More details can be found in Junk and Yang [39].

2.3.5 Forcing scheme

To consider the force densities $\vec{f}$ in (2.5), an additional term is added to the standard LBE in (2.33) as

$$f_i\left(t + \Delta t, \vec{x} + \vec{c}_i\,\Delta t\right) = f_i\left(t, \vec{x}\right) - \frac{\Delta t}{\tau}\left(f_i\left(t, \vec{x}\right) - f_i^{\text{eq}}\left(t, \vec{x}\right)\right) + \Omega_i^{\text{F}}\left(t, \vec{x}\right),$$

with forcing (F) term $\Omega_i^{\text{F}} : I_h \times \Omega_h \to \mathbb{R}$. An overview of available schemes to consider body forces in LBM can be found in Guo and Shu [17] In this thesis, the scheme of Guo, Zheng, and Shi [40] is used. The velocity $\vec{u}^{\text{eq}}$ entering into the EDF f_i^{eq} in (2.16) as well as the fluid velocity $\vec{u}$ is replaced by

$$\vec{u}^{\text{eq}} = \vec{u} = \frac{\sum_i \vec{c}_i\,f_i}{\rho} + \frac{\Delta t\,\vec{f}}{2\,\rho}\,. \tag{2.66}$$

The forcing term is given by

$$\Omega_i^{\text{F}}\left(t, \vec{x}\right) = \Delta t\,w_i\left(1 - \frac{\Delta t}{2\,\tau}\right)\left(\frac{\vec{c}_i - \vec{u}^{\text{eq}}}{c_s^2} + \frac{\vec{c}_i \cdot \vec{u}^{\text{eq}}}{c_s^4}\,\vec{c}_i\right) \cdot \vec{f}. \tag{2.67}$$

A two-scale analysis in time leads to the Navier-Stokes equation.

2.3.6   Smagorinsky-Lilly turbulence scheme

A distinction is made between laminar and turbulent flows. In laminar flows the Reynolds number is small. The fluid moves in an ordered manner in parallel layers, the flow is predictable and deterministic [41]. At higher Reynolds numbers, the flow behaviour is turbulent and always unsteady, random and chaotic [42]. The flow velocity $\vec{u}(t, \vec{x})$ is composed of a steady mean velocity $\vec{u}\,'(\vec{x})$ and a fluctuating velocity $\vec{u}_f(t, \vec{x})$,

$$\vec{u}(t, \vec{x}) = \vec{u}\,'(\vec{x}) + \vec{u}_f(t, \vec{x}) \ . \tag{2.68}$$

The turbulent eddies stretch, rotate and show a wide range of length scales. They cause a very effective exchange of heat, mass and momentum and can break up into further eddies due to the vortex stretching. Large eddies consist of a characteristic velocity and length $L_t \in \mathbb{R}_{>0}\ [L]$ of the same order of magnitude as the mean flow. Since the associated Reynolds number is large, large vortices are dominated by inertial effects, viscous effects are small. Their structure is anisotropic. Small vortices receive their energy from large vortices mainly through energy cascades. The smallest length scales are called Kolmogorov micro scales $\eta_t \in \mathbb{R}_{>0}\ [L]$. Their motion is dominated by both inertia and viscosity effects, the corresponding Reynolds number equals one. The smaller the vortex, the smaller the energy it contains. Its kinetic energy dissipates and transforms into internal thermal energy. Its structure is isotropic.

Since turbulent flows are irregular and possess enormous time and length scales, a detailed and completely resolved simulation like the direct numerical simulation is computationally intensive [43]. More cost effective simulations are possible by turbulence modeling, e.g. in large eddy simulations. The associated governing equations are the filtered incompressible continuity and the Navier-Stokes equation. This involves resolving the large scales and modeling the smallest scales as they are filtered in the governing equations, Figure 2.4. The Smagorinsky-Lilly scheme adds an eddy sub-grid scale viscosity

$$\mu_t = \rho\,(c_t\,\Delta x)^2\,\|S\| = \rho\,(c_t\,\Delta x)^2\,\sqrt{2\,S_{\alpha\beta}\,S_{\alpha\beta}} \tag{2.69}$$

to model the local sub-grid scale stresses that are proportional to the local strain rate

$$S_{\alpha\beta} = \frac{1}{2}\left(\frac{\partial\,u_\alpha}{\partial\,x_\beta} + \frac{\partial\,u_\beta}{\partial\,x_\alpha}\right) , \tag{2.70}$$
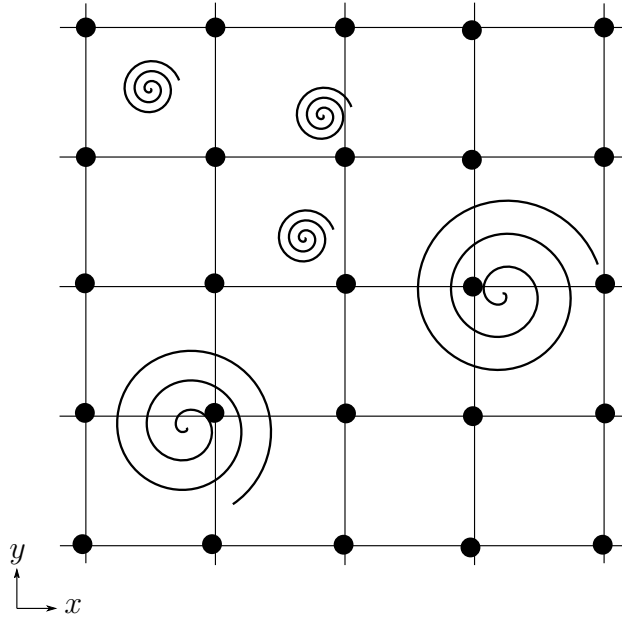
Figure 2.4: Schematic depiction of resolved (large scale) and unresolved (sub-grid scale) eddies of turbulence.

$\alpha, \beta \in \{1, \ldots, d\}$ [42]. $c_t \in \mathbb{R}_{\geq 0}$ is the Smagorinsky constant and depends on the flow problem. Different works suggest values of c_t from 0.1 to 0.24. μ_t enters into (2.34) by the modified relaxation time

$$\tau_t = (\mu_t + \mu)/(\rho \, c_s^2) + \Delta t/2 \,. \tag{2.71}$$

The Smagorinsky-Lilly scheme is applied to LBM by Hou et al. [44]. The strain rate

$$S_{\alpha\beta} = -\frac{1}{2 \, \rho \, \tau_t \, c_s^2} \, \Pi_{\alpha\beta} = -\frac{1}{2 \, \rho \, \tau_t \, c_s^2} \sum_i c_{i,\alpha} \, c_{i,\beta} \, (f_i - f_i^{\mathrm{eq}}) \tag{2.72}$$

is locally computed by the non-equilibrium stress tensor $\Pi_{\alpha\beta}$.

2.3.7 Lattice Boltzmann method for dissolved reactive substances

The LBM is also a suitable method for solving the mass transport equations for solutes given by the ADRE in (2.6) [19, 45]. In this case, the LBE is given by

$$g_j(t + \Delta t, \vec{x} + \vec{c}_j \, \Delta t) = g_j(t, \vec{x}) - \frac{\Delta t}{\tau_g}(g_j(t, \vec{x}) - g_j^{\mathrm{eq}}(t, \vec{x})) + \Delta t \, w_j \, R_j(t, \vec{x}) \,, \tag{2.73}$$

with the distribution function $g_j : I_h \times \Omega_h \to \mathbb{R}_{>0}$ [N L^{-3}], lattice weights $w_j \in \mathbb{R}$ and relaxation time $\tau_g = \frac{D}{c_s^2} + 0.5 \, \Delta t \in \mathbb{R}_{>0}$ [T]. Its dimensionless size is described by τ_g'. g_j

consists of $q_g \in \mathbb{N}$ discrete velocity directions $\vec{c}_j \in \Omega_c \subseteq \mathbb{R}^3$, $j = 0, \ldots, q_g - 1$. The particles collide and relax towards the linear EDF $g_j^{\mathrm{eq}} : I_h \times \Omega_h \to \mathbb{R}_{\geq 0}$ [N L^{-3}] [19, 46],

$$g_j^{\mathrm{eq}}(t, \vec{x}) = w_j \, c \left[1 + \frac{\vec{c}_j \cdot \vec{u}}{c_s^2} \right] . \tag{2.74}$$

The concentration is calculated by the zeroth moment of g_j, $c := c(t, \vec{x}) = \sum_j g_j(t, \vec{x})$. The source term R of the ADRE (2.6) is given by $R := R(t, \vec{x}) = \sum_j R_j(t, \vec{x})$ with the source term $R_j : I_h \times \Omega_h \to \mathbb{R}$. In this thesis, a linear first order rate kinetics for adsorption process is assumed which is given by

$$R_j(t, \vec{x}) = -K \, g_j(t, \vec{x}) , \tag{2.75}$$

with sink factor $K \in \mathbb{R}$ [T^{-1}].

2.4   Conclusion

First, an introduction into the different scales to describe fluid motion was given, followed by the continuity, the NSE and the ADRE. Subsequent, the LBM were derived and the Chapman-Enskog analysis showed that the governing equations are recovered from the LBM. Specifications to the LBM e.g. to handle turbulence models or to incorporate body forces were given. It was shown that the LBM also solve the mass transport with chemical reactions.

3 Modeling and simulation approaches of volume-averaged reactive flows[1]

Volume-averaged equations provide a way to model dense reactive particle fluid flows. In the following, the relevant equations for fluid flow and reactive mass transport through the VANSE and the VAADRE are given. Finally, the lattice Boltzmann schemes for these equations are discussed.

3.1 Governing equations

The conditions under which the methods of volume-averaging are applied are introduced by Whitaker [48]. The intrinsic volume-average of a fluid property $[\cdot]$ with averaging operator $\langle [\cdot] \rangle$ is defined as

$$\langle [\cdot] \rangle = \frac{1}{V_f} \int_{V_f} [\cdot] \, \mathrm{d}\, V \, ,$$

with fluid volume $V_f \in \mathbb{R}_{>0}$ [L^3] and cell volume $V \in \mathbb{R}_{>0}$ [L^3] [49, 50].

3.1.1 Volume-averaged Navier-Stokes equations

Following the volume-averaging procedure given by Whitaker [48] and Enwald et al. [49] the volume-averaged continuity equation is given as

$$\frac{\partial \, \rho \, \phi}{\partial \, t} + \nabla \cdot \left(\rho \, \phi \, \langle \vec{u} \rangle \right) = 0 \, . \tag{3.1}$$

The corresponding volume-averaged momentum equation is given as

$$\frac{\partial \rho \phi \langle \vec{u} \rangle}{\partial t} + \Big(\rho \phi \langle \vec{u} \rangle \cdot \nabla \Big) \langle \vec{u} \rangle = -\phi \nabla \langle p \rangle + \mu \nabla^2 \phi \langle \vec{u} \rangle + \vec{f}_{\text{ext.}} \,. \tag{3.2}$$

(3.1) and (3.2) together are referred to as the VANSE. $\phi : I \times \Omega \to [0, 1] \; [-]$ is the fluid volume fraction, also referred to as porosity of the media. A hydrodynamic drag force density $\vec{f}_{\text{d}} : I \times \Omega \to \mathbb{R}^3 \; [\text{M} \, \text{L}^{-2} \, \text{T}^{-2}]$ accounts for the back-coupling force of the solid particles to the fluid. $\vec{f}_{\text{body}} : I \times \Omega \to \mathbb{R}^3 \; [\text{M} \, \text{L}^{-2} \, \text{T}^{-2}]$ is an external body force density. The forces are combined in the external force density $\vec{f}_{\text{ext.}} = \vec{f}_{\text{d}} + \vec{f}_{\text{body}}$.

3.1.2   Volume-averaged advection-diffusion-reaction equation

Applying the volume-averaging procedure as described in Wood et al. [51], the VAADRE is given as

$$\frac{\partial \phi c}{\partial t} + \nabla \cdot \Big(\phi c \langle \vec{u} \rangle - D_{\text{e}} \nabla c \Big) = R \,. \tag{3.3}$$

In the equation above the dispersion term is neglected, a valid assumption for low to medium Peclet numbers. The coupling with the fluid flow is done in a passive-scalar manner by the averaged fluid velocity $\langle \vec{u} \rangle$, which is the solution of VANSE in (3.1) and (3.2). $D_{\text{e}} \in \mathbb{R}$ is the effective diffusion coefficient $[\text{L}^2 \, \text{T}^{-1}]$ that is related to the molecular diffusion coefficient of reacting substances $D \in \mathbb{R}$. The relationship is derived through differential effective media theory which provides analytical expression for effective diffusion which is valid for both moderate and high solid volume fractions [52, 53]. It is given by $D_{\text{e}} = \phi^{1.5} D$ [54]. The term on the right hand side of (3.3) is the source term $R : I \times \Omega \to \mathbb{R} \; [\text{N} \, \text{L}^{-3} \, \text{T}^{-1}]$ for reactions.

3.2   Lattice Boltzmann method for the volume-averaged Navier-Stokes equations

The LBM equation for VANSE is given as follows:

$$f_i(t + \Delta t, \vec{x} + \vec{c}_i \, \Delta t) = f_i(t, \vec{x}) + \Omega_i^{\text{BGK}}(t, \vec{x}) + \Omega_i^{\text{PCR}}(t, \vec{x}) + \Omega_i^{\text{F}}(t, \vec{x}) \,. \tag{3.4}$$

The above equation depicts the evolution of the discrete particle density distribution function $f_i : I_h \times \Omega_h \to \mathbb{R}_{>0}$ for a specific time $t \in I_h$ and position $\vec{x} \in \Omega_h$. During the collision step, f_i is redistributed by the BGK-collision operator [23]

$$\Omega_i^{\mathrm{BGK}}(t, \vec{x}) = -\frac{\Delta t}{\tau}(f_i(t, \vec{x}) - f_i^{\mathrm{eq}}(t, \vec{x}))$$

among $q_f \in \mathbb{N}$ discrete lattice velocity directions $\vec{c}_i \in \mathbb{R}^3$, $i \in \{0, \ldots, q_f - 1\}$. It relax towards the EDF

$$f_i^{\mathrm{eq}}(t, \vec{x}) = w_i\, \phi(t, \vec{x})\, \rho \left(1 + \frac{\vec{c}_i \cdot \langle \vec{u} \rangle^{\mathrm{eq}}(t, \vec{x})}{c_s^2} - \frac{\langle \vec{u} \rangle^{\mathrm{eq}}(t, \vec{x}) \cdot \langle \vec{u} \rangle^{\mathrm{eq}}(t, \vec{x})}{2\, c_s^2} + \frac{(\vec{c}_i \cdot \langle \vec{u} \rangle^{\mathrm{eq}}(t, \vec{x}))^2}{2\, c_s^4} \right) \tag{3.5}$$

with respect to the relaxation time

$$\tau = \frac{\mu}{\rho\, c_s^2} + \frac{\Delta t}{2}\,.$$

$$\langle \vec{u} \rangle^{\mathrm{eq}}(t, \vec{x}) = \frac{\sum_i f_i(t, \vec{x})\, \vec{c}_i}{\phi(t, \vec{x})\, \rho} + \frac{\Delta t\, \vec{f}_{\mathrm{d}}(t, \vec{x})}{2\, \phi(t, \vec{x})\, \rho}\,, \tag{3.6}$$

is the equilibrium velocity with the speed of sound $c_s \in \mathbb{R}$ and the lattice weights $w_i \in \mathbb{R}$. f_i^{eq} is given by a Maxwell-Boltzmann distribution and is scaled by ϕ [55]. The second term in (3.6) is added to apply force density $\vec{f}_{\mathrm{ext.}}$ using Guo forcing scheme [40]. The forcing term is written as

$$\Omega_i^{\mathrm{F}}(t, \vec{x}) = \Delta t\, w_i \left(1 - \frac{\Delta t}{2\,\tau} \right) \left(\frac{\vec{c}_i - \langle \vec{u} \rangle^{\mathrm{eq}}(t, \vec{x})}{c_s^2} + \frac{\vec{c}_i \cdot \langle \vec{u} \rangle^{\mathrm{eq}}(t, \vec{x})}{c_s^4}\, \vec{c}_i \right) \cdot \vec{f}_{\mathrm{ext.}}(t, \vec{x})\,. \tag{3.7}$$

Furthermore, the first moments of the distribution are scaled by ϕ to achieve the macroscopic quantities

$$\phi(t, \vec{x})\, \rho = \sum_i f_i(t, \vec{x}) \qquad \text{and} \qquad \phi(t, \vec{x})\, \rho\, \langle \vec{u} \rangle(t, \vec{x}) = \sum_i f_i(t, \vec{x})\, \vec{c}_i\,. \tag{3.8}$$

The pressure is obtained by $p(t, \vec{x}) = c_s^2\, \rho/\phi(t, \vec{x})$. It can be shown through the Chapman-Enskog analysis that the above lattice Boltzmann scheme would recover following equation in the macroscopic limits [55, 56]:

$$\frac{\partial\, \rho\, \phi\, \langle \vec{u} \rangle}{\partial t} + \left(\rho\, \phi\, \langle \vec{u} \rangle \cdot \nabla \right) \langle \vec{u} \rangle = -\nabla\, \phi\, \langle p \rangle + \mu\, \nabla^2 \phi\, \langle \vec{u} \rangle + \vec{f}_{\mathrm{ext.}}\,. \tag{3.9}$$

Note that the above equation leads to incorrect pressure term for the case with varying spatial porosity. Therefore a pressure correction term has been introduced in (3.4). The pressure correction term (PCR) in this thesis is taken as follows

$$\Omega_i^{\mathrm{PCR}}(t, \vec{x}) = w_i\, \rho \left(\phi(t, \vec{x} + \vec{c}_i\, \Delta t) - \phi(t, \vec{x}) \right).\tag{3.10}$$

This term upon Taylor-series expansion and Chapman-Enskog analysis would add $\langle p \rangle \nabla \phi$ to the right hand side of (3.9) thus correcting the pressure term. This is a more simple approach for implementation in the existing LB code than the modification of the streaming step through scaling as suggested in Höcker et al. [56].

3.3   Lattice Boltzmann method for the volume-averaged advection-diffusion-reaction equation

For the VAADRE, the two relaxation time (TRT) LBM is used [10, 13, 57] which is given by

$$g_j(t + \Delta t, \vec{x} + \vec{c}_j\, \Delta t) = g_j(t, \vec{x}) + \Omega_j^{\mathrm{TRT}}(t, \vec{x}) + \Omega_j^{\mathrm{RXN}}(t, \vec{x}).\tag{3.11}$$

The TRT LBM scheme has some advantages compared to the SRT scheme while maintaining algorithmic simplicity. One of the two relaxation parameters is linked to the physical quantity, the other one adjusted to control the errors. Nevertheless, stability of simulations is not necessary assured by switching from SRT to TRT [19]. Here, $g_j : I_h \times \Omega_h \to \mathbb{R}_{>0}$ is the discrete particle density distribution function for the reactive mass transport with $j \in \{0, \ldots, q_g - 1\}$, $q_g \in \mathbb{N}$ and the discrete lattice velocity directions $\vec{c}_j \in \mathbb{R}^3$.

The general idea of the TRT scheme is to relax the symmetric (g_j^+), respective the anti-symmetric (g_j^-) part of g_j,

$$g_j^+ = \frac{g_j + g_{-j}}{2}, \qquad \text{respective} \qquad g_j^- = \frac{g_j - g_{-j}}{2},$$

towards the appropriate EDF in (3.12),

$$g_j^{\mathrm{eq}+} = \frac{g_j^{\mathrm{eq}} + g_{-j}^{\mathrm{eq}}}{2}, \qquad \text{respective} \qquad g_j^{\mathrm{eq}-} = \frac{g_j^{\mathrm{eq}} - g_{-j}^{\mathrm{eq}}}{2},$$

using the two different relaxation parameters τ^+ and τ^-. The index $-j$ refers to the opposite

velocity direction of $j \in \{1, \ldots, q_g - 1\}$, i.e. $\vec{c}_j = -\vec{c}_{-j}$. In the equation above, the TRT collision operator is given by following equation

$$\Omega_j^{\mathrm{TRT}}(t, \vec{x}) = -\frac{\Delta t}{\tau^+}(g_j^+(t, \vec{x}) - g_j^{\mathrm{eq}+}(t, \vec{x})) - \frac{\Delta t}{\tau^-}(g_j^-(t, \vec{x}) - g_j^{\mathrm{eq}-}(t, \vec{x})) . \qquad (3.12)$$

The source or sink operator is given by

$$\Omega_j^{\mathrm{RXN}}(t, \vec{x}) = \Delta t \, w_j \, R(t, \vec{x}) , \qquad (3.13)$$

where $w_j = c_\phi / 2$ for $j \in \{1, \ldots, q_g - 1\}$ and $w_0 = (1 - 2 \, c_\phi)$ [57]. $c_\phi \in \mathbb{R}_{>0}$ is a constant parameter that is used to adjust the diffusion coefficient. It is necessary that $c_\phi \leq \min(\phi)/3$ [10]. Here, it is given by $c_\phi = 1/3.5$. The two relaxation parameters τ^+ and τ^- are linked together through the magic parameter (Λ) which is given as

$$\Lambda = (\tau^+ - 0.5)(\tau^- - 0.5) .$$

τ^+ is a free parameter which is chosen to have a stable and accurate simulation. In the thesis it is set to $1/4$ which ensures optimal stability [58].

To recover (3.3), the appropriate EDF for orthogonal lattice [13, 57] is given as

$$g_j^{\mathrm{eq}}(t, \vec{x}) = \frac{c(t, \vec{x})}{2}\left(c_\phi + \phi(t, \vec{x}) \, \vec{c}_j \cdot \langle \vec{u} \rangle(t, \vec{x})\right) , \qquad (3.14)$$

$$g_0^{\mathrm{eq}}(t, \vec{x}) = \phi(t, \vec{x}) \, c(t, \vec{x}) - \sum_{j>0} g_j^{\mathrm{eq}}(t, \vec{x}) . \qquad (3.15)$$

The zeroth moment of g_j is

$$\phi(t, \vec{x}) \, c(t, \vec{x}) = \sum_j g_j(t, \vec{x}) . \qquad (3.16)$$

With above LBE it can be shown that (3.3) can be recovered through the multi-scale Chapman-Enskog analysis [13, 57]. The effective diffusion coefficient D_{e} is linked to τ^- through following relation:

$$D_{\mathrm{e}} = \phi(t, \vec{x}) \, D = c_\phi \left(\tau^- - \frac{\Delta t}{2}\right) .$$

3.4   Conclusion

In this chapter, fluid flow and reactive transport processes around disperse and moving particles were recovered in kind of a continuum framework through a volume-averaging procedure. The displacement of the fluid and the reactive mass was considered by the VANSE and the VAADRE. Specifications of the LBM to solve the equations were presented.

4 Newton's equations of motion for particles

The motion of the solid particles is modeled using the DEM. It solves particle motions by integrating Newton's second law. While coupling with the fluid flow, e.g. hydrostatic (buoyancy force) and hydrodynamic forces (drag force) are included. Particle interaction is modeled using contact laws which account for forces due to particle-particle contacts and friction between particles.

4.1 Newton's equation of motion

Newton's equation of motion is the governing equation for each of the finite number $n \in \mathbb{N}$ of particles submerged in fluid. Depending on the desired setup, the motion of an immersed particle is influenced by different forces. The equation for the force defines the translational dynamics of the particle by the sum of all acting forces $\vec{F}_l : I \to \mathbb{R}^3$ $[\mathrm{M\,L\,T^{-2}}]$:

$$m_l \frac{\mathrm{d}\,\vec{u}_l(t)}{\mathrm{d}\,t} = m_l \frac{\mathrm{d}^2 \vec{x}_l(t)}{\mathrm{d}\,t^2} = \vec{F}_l(t)\,, \tag{4.1}$$

for $t \in I$. The particles are numbered consecutively by the index $l = 1,\, 2,\, \ldots,\, n$. In this thesis each particle is treated as a spherical particle with mass $m_l \in \mathbb{R}_{>0}$ [M], radius $r_l \in \mathbb{R}_{>0}$ [L], particle position $\vec{x}_l : I \to \Omega$ [L] and particle velocity $\vec{u}_l : I \to \mathbb{R}^3$ $[\mathrm{L\,T^{-1}}]$. To consider rotational dynamics of a particle, the sum of all torques $\vec{T}_l : I \to \mathbb{R}^3$ $[\mathrm{M\,L^2\,T^{-2}}]$ influences its orientation by

$$J_l \frac{\mathrm{d}\,\vec{\omega}_l(t)}{\mathrm{d}\,t} = \vec{T}_l(t)\,. \tag{4.2}$$

with the moment of inertia $J_l \in \mathbb{R}^3$ $[\mathrm{M\,L^2}]$ and the angular velocity $\vec{\omega}_l : I \to \mathbb{R}^3$ $[\mathrm{T^{-1}}]$. In case of a massive sphere it is $J_l = 2/5\,m_l\,r_l^2$.

4.2   Forces on particles

The forces occurring in the equation of Basset [59], Boussinesq [60] and Oseen [61] describe the movement of a sedimenting sphere under gravity in an initially resting fluid. The equation was later extended to unsteady and non-uniform flows [62]. In the following, the hydrostatic (buoyancy), hydrodynamic (drag), gravitational, additional mass and body forces caused by pressure gradients are presented. The basset force is excluded since its influence is small here. More detailed descriptions can be found in [63, 64] or in the original literature.

The drag force $\vec{F}_{d,l} : I \to \mathbb{R}^3$ $[\mathrm{M\,L\,T^{-2}}]$ depends on the relative acceleration between particle and fluid,

$$\vec{F}_{d,l}(t) = 0.5\,\rho_l\,c_{d,l}\,A_l \left\| \vec{u}(t,\vec{x}_l(t)) - \vec{u}_l(t) \right\|_2 \Big(\vec{u}(t,\vec{x}_l(t)) - \vec{u}_l(t) \Big), \tag{4.3}$$

for $t \in I$ and $l = 1, 2, \ldots, n$. $A_l = \pi\,r_l^2 \in \mathbb{R}_{>0}$ is the cross-sectional area of a spherical particle. For non-rotating, spherical objects in an incompressible fluid flow, the dimensionless drag coefficient $c_{d,l} = c_{d,l}(\mathrm{Re}_l) \in \mathbb{R}_{>0}$ $[-]$ depends on the Reynolds number of the particle,

$$\mathrm{Re}_l = \frac{2\,r_l\,\rho\,\|\vec{u} - \vec{u}_l\|}{\mu} \in \mathbb{R}_{>0}\,. \tag{4.4}$$

The *standard drag curve* represents the drag coefficient as a function of Re_l and is shown in Figure 4.1. It is approximated by a large number of empirical or semi-empirical equations [65]. The dimensionless *Stokes number* $\mathrm{St} \in \mathbb{R}_{\geq 0}$ describes the relationship between the relaxation time $T_l \in \mathbb{R}$ $[\mathrm{T}]$ of a particle and the characteristic time $T_{\mathrm{ch}} \in \mathbb{R}$ $[\mathrm{T}]$ of the fluid:

$$\mathrm{St} = \frac{T_l}{T_{\mathrm{ch}}} = \frac{2\,\rho_l\,\rho\,r_l^2\,U_{\mathrm{ch}}}{9\,\mu\,L_{\mathrm{ch}}}\,. \tag{4.5}$$

T_l is the time a particle needs to reach a steady velocity under the influence of external forces. For $\mathrm{St} \ll 1$ the particle adapts directly to the fluid flow. In contrast, for $\mathrm{St} \gg 1$ the particle is hardly affected by changes in the fluid flow. In the Stokes flow regime ($\mathrm{Re}_l < 1$), the drag coefficient is given by

$$c_{d,l} = 24/\mathrm{Re}_l = \frac{24\,\mu}{2\,r_l\,\rho_l \left\| \vec{u}(t,\vec{x}_l(t)) - \vec{u}_l(t) \right\|_2}\,. \tag{4.6}$$

In combination with (4.3) this results in the Stokes drag force [66]

$$\vec{F}_{\text{Stokes},l}(t) = 6\,\pi\,\mu\,r_l\left(\vec{u}(t,\vec{x}_l(t)) - \vec{u}_l(t)\right).\tag{4.7}$$

In Chapter 6, the drag coefficient of Schiller and Naumann [67] is used as proposed in [68]:

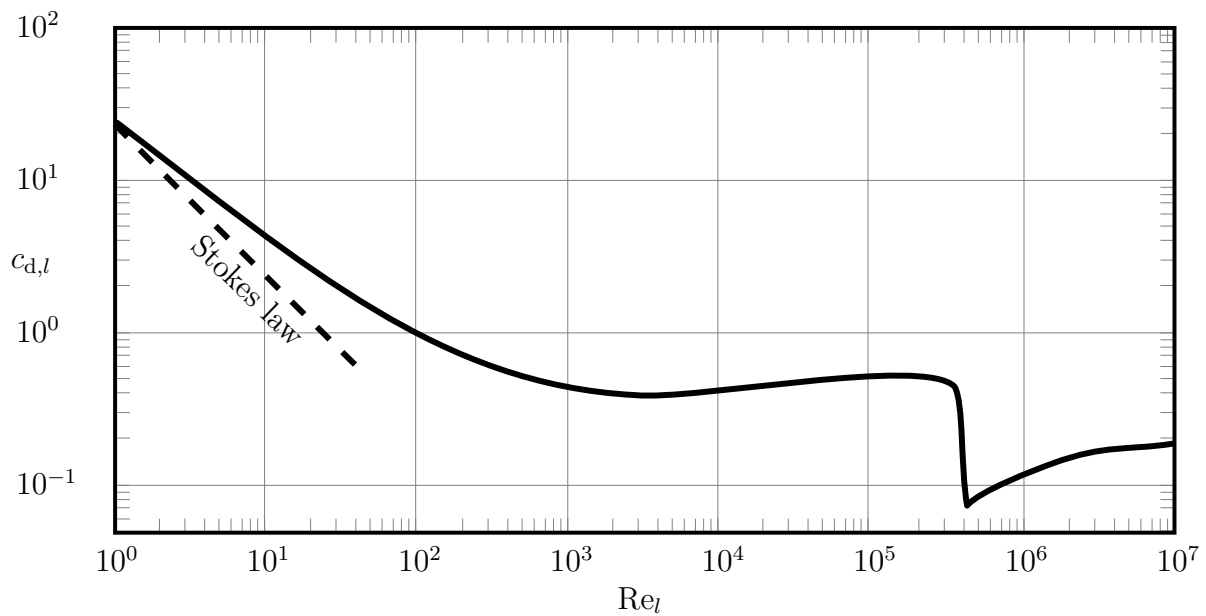$$c_{\text{d},l} = \frac{24}{\text{Re}_l}\left(1 + 0.15\,\text{Re}_l^{0.687}\right)\quad\text{for }\text{Re}_l \leq 1{,}000\,.\tag{4.8}$$

Figure 4.1: Representation of the drag coefficient $c_{\text{d},l}$ as a function of Re for a sphere. The curve is also called *standard resistance curve* (adapted from [65]).

The weight $\vec{F}_{\text{g},l}: I \to \mathbb{R}^3$ and buoyancy force $\vec{F}_{\text{b},l}: I \to \mathbb{R}^3$ $[\text{M}\,\text{L}\,\text{T}^{-2}]$ is given by

$$\vec{F}_{\text{g},l}(t) + \vec{F}_{\text{b},l}(t) = \left(m_l - 4/3\,\pi\,r_l^3\,\rho\right)\vec{g}\tag{4.9}$$

with the gravitational acceleration $\vec{g} \in \mathbb{R}^3$ $[\text{L}\,\text{T}^{-2}]$. The buoyancy force results from hydrostatic pressure fluctuations [69] and acts in the opposite direction to gravity.

The body force $\vec{F}_{\text{pg},l}: I \to \mathbb{R}^3$ $[\text{M}\,\text{L}\,\text{T}^{-2}]$ resulting from the pressure gradient around a particle along the fluid flow is given by

$$\vec{F}_{\text{pg},l}(t) = -\frac{m_l}{\rho_l}\,\nabla p\,.\tag{4.10}$$

The added mass force $\vec{F}_{\mathrm{am},l} : I \to \mathbb{R}^3$ $[\mathrm{M\,L\,T^{-2}}]$ is considered to account for the resistance of the surrounding water during acceleration,

$$\vec{F}_{\mathrm{am},l}(t) = 0.5 \left(4/3\,\pi\,r_l^3\,\rho \right) \left(\frac{\mathrm{D}\,\vec{u}(t, \vec{x}_l(t))}{\mathrm{D}\,t} - \frac{\mathrm{d}\,\vec{u}_l(t)}{\mathrm{d}\,t} \right), \tag{4.11}$$

as given in [70, 71].

4.3   Particle interaction

To describe particle contacts, there exist the hard- and the soft-sphere model [72]. The hard-sphere model considers impulse-maintaining binary collisions of rigid spheres occurring instantaneously and pairwise additively. The contacts are calculated in a chronological order, making the model more suitable for low particle concentrations. In this thesis, the soft-sphere model is applied that resolves a particle contact in time. Simultaneous contacts of one particle with others are possible. After all contacts have been detected, the sum of all contact forces enters into Newton's equations of motion.

To compute the total contact force $\vec{F}_{\mathrm{c},l} : I \to \mathbb{R}^3$ $[\mathrm{M\,L\,T^{-2}}]$ on particle l, the individual inter-particle contact forces $\vec{F}_{\mathrm{c},lk} : I \to \mathbb{R}^3$ $[\mathrm{M\,L\,T^{-2}}]$ of the particles k inside the contact list of particle l are summed up:

$$\vec{F}_{\mathrm{c},l}(t) = \sum_{k=1}^{k_l} \vec{F}_{\mathrm{c},lk}(t), \tag{4.12}$$

$k = 1, 2, \ldots, k_l \in \mathbb{N}_{\leq n}$, $k, k_l \neq l$, $k_l \geq k$. $\vec{F}_{\mathrm{c},lk}$ depends on the virtual displacement $\delta_{\mathrm{n},lk} : I \to \mathbb{R}_{\leq 0}$ [L] between the interacting particles which is given by

$$\delta_{\mathrm{n},lk} = \begin{cases} (r_l + r_k) - \|\vec{x}_{lk}\|, & \text{for } \|\vec{x}_{lk}\| < (r_l + r_k) \\ 0, & \text{for } \|\vec{x}_{lk}\| \geq (r_l + r_k) \end{cases} \tag{4.13}$$

with conjunction vector $\vec{x}_{lk} : I \to \mathbb{R}_{\leq 0}$ [L], see Figure 4.2. Several models exist for the description of $\vec{F}_{\mathrm{c},l}$. For more information about DEM and contact forces, see, for example, [73, 74].

In *Yade* that is used in Chapter 6, the contact force $\vec{F}_{\text{c},lk}$ is divided into the normal force $\vec{F}_{\text{n},lk} : I \to \mathbb{R}^3$ and the shear force $\vec{F}_{\text{t},lk} : I \to \mathbb{R}^3$,

$$\vec{F}_{\text{c},lk}(t) = \vec{F}_{\text{n},lk}(t) + \vec{F}_{\text{t},lk}(t) , \tag{4.14}$$

$$\vec{F}_{\text{n},lk}(t) = k_{\text{n},lk}\, \delta_{\text{n},lk}\, \vec{n}_{lk} , \tag{4.15}$$

$$\vec{F}_{\text{t},lk}(t) = k_{\text{t},lk}\, \vec{\delta}_{\text{t},lk} . \tag{4.16}$$

They depend on the normal $k_{\text{n},lk} \in \mathbb{R}\,[\text{M}\,\text{L}^{-2}\,\text{T}^{-2}]$ and the shear stiffness $k_{\text{t},lk} \in \mathbb{R}\,[\text{M}\,\text{L}^{-2}\,\text{T}^{-2}]$ as well as on the normal $\delta_{\text{n},lk} \in \mathbb{R}_{\geq 0}\,[\text{M}]$ and the shear displacement $\vec{\delta}_{\text{t},lk} \in \mathbb{R}^3_{\geq 0}\,[\text{M}]$. The latter is perpendicular to the normal $\vec{n}_{lk} \in \mathbb{R}^3\,[-]$ of the conjunction vector $\vec{x}_{lk} \in \mathbb{R}^3$. $k_{\text{n},lk}$ and $k_{\text{t},lk}$ are determined by the particle's material properties and are related to the macroscopic Young's modulus and the Poisson's ratio [75]. The contact force $\vec{F}_{\text{c},l}$ is taken into account by the contact laws of Cundall and Strack [73] and results from the sum of the contact forces $\vec{F}_{\text{c},lk}$ in (4.14), (4.15) and (4.16) of the particles k that are in the contact list of particle l, $\vec{F}_{\text{c},l}(t) = \sum_{k=1, k \neq l}^{k_l} \vec{F}_{\text{c},lk}$ with $k = 1, 2, \ldots, k_l \in \mathbb{N}_{\leq n}$ [75]. As the contact force acts on the virtual contact point of the particles, the torque is considered by

$$\vec{T}_{\text{c},l}(t) = -d_l\, \vec{n}_{lk} \times \vec{F}_{\text{c},lk} , \tag{4.17}$$

with distance $d_l \in \mathbb{R}$ from particle center to the contact point. Since periodic boundaries are used in this thesis, interactions between particles and walls are neglected. More information about the contact detection and the contact laws in *Yade* is given in Smilauer et al. [76, 77].
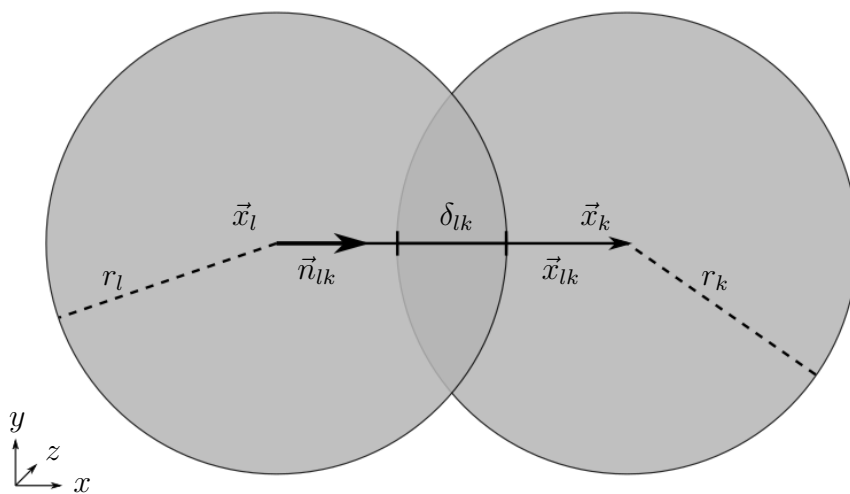

Figure 4.2: Schematic depiction of a particle-particle contact.

4.4   Coupling of the components[1]

For the computation of the drag force and the added mass forces on particles in (4.3) and (4.11), the fluid velocity $\vec{u}$, respective the average fluid velocity $\langle \vec{u} \rangle$, at particle position $\vec{x}_l(t) = (x_{l,1}, x_{l,2}, x_{l,3})$ is obtained through linear interpolation commonly used by different authors [78–80] and is performed as

$$\vec{u}\left(t, \vec{x}_l(t)\right) = \Sigma_{\vec{x} \in \Omega_h}\, s_l\left(t, \vec{x}\right)\, \vec{u}\left(t, \vec{x}\right)\,, \tag{4.18}$$

respective as

$$\langle \vec{u} \rangle\left(t, \vec{x}_l(t)\right) = \Sigma_{\vec{x} \in \Omega_h}\, s_l\left(t, \vec{x}\right)\, \langle \vec{u} \rangle\left(t, \vec{x}\right)\,, \tag{4.19}$$

where the interpolation operator $s_l : I_h \times \Omega_h \rightarrow [0, 1]$ is performed as

$$s_l\left(t, \vec{x}\right) = \begin{cases} \Pi_{d=1}^{3}\left(1 - \frac{|x_{l,d}(t) - x_d|}{\Delta x}\right) & \text{if } |x_{l,d}\left(t\right) - x_d| \leq \Delta x \text{ for } d \in \{1, 2, 3\}\,, \\ 0 & \text{otherwise}\,. \end{cases} \tag{4.20}$$

Here, it is $\vec{x} = (x_1, x_2, x_3) \in \Omega_h$, the Euler grid spacing $\Delta x > 0$ and the product operator Π.

The drag force acting on the fluid is computed through the momentum exchange principle, i.e. the force acting on the fluid points is equal to that on the particles as given in (4.3) but acting in reverse direction. The force enters into (3.2) through the force density which is linearly interpolated by s_l given in (4.20) on the fluid cell volume from the particle drag force as follows

$$\vec{f}_{\mathrm{d}}(t, \vec{x}) = -\frac{\Sigma_{l \in \{1,\ldots,n\}}\, s_l\left(t, \vec{x}\right)\, \vec{F}_{\mathrm{d},l}(t)}{\Delta x^3}\,, \tag{4.21}$$

with the volume $\Delta x^3 \in \mathbf{R}_{>0}$ of a grid cell of the homogeneous Euler grid with spacing Δx [50, 81].

The porosity $\phi : I \times \Omega \rightarrow [0, 1]\ [-]$ which accounts for the change in the volume of fluid due to presence of solid particles in the Euler grid volume in (3.1), (3.2) and (3.3) is computed by following equation

$$\phi\left(t, \vec{x}\right) = 1 - \frac{\Sigma_{l \in \{1,\ldots,n\}}\, s_l\left(t, \vec{x}\right)\, 4/3\,\pi\, r_l^3}{\Delta x^3}\,. \tag{4.22}$$

The specific surface area $A_{\mathrm{s}} : I \times \Omega \to \mathbb{R}$ [L^{-1}] needed to get the source term R in (3.3) is computed from the solid particle location,

$$A_{\mathrm{s}}\left(t, \vec{x}\right) = \frac{\Sigma_{l \in \{1, \ldots, n\}}\, s_l\left(t, \vec{x}\right)\, 4\,\pi\, r_l^2}{\Delta x^3}\,. \tag{4.23}$$

4.5 Conclusion

In this chapter, Newton's equations of motion for solving particle motions were presented. Considered forces acting on the particles were hydrostatic (buoyancy), hydrodynamic (drag), gravitational, body force due to the pressure gradient, added mass forces as well as particle-particle contact forces. The coupling of the components closes the chapter.

Part 2

Research and applications

5 One-way coupled reactive particle fluid flows

- The contents of this chapter are published in the following reference and are adapted for this dissertation:

  M.-L. Maier, S. Milles, S. Schuhmann, G. Guthausen, H. Nirschl, and M. J. Krause. "Fluid flow simulations verified by measurements to investigate adsorption processes in a static mixer". In: *Computers & Mathematics with Applications* 76 (2018), pp. 2744–2757. DOI: `10.1016/j.camwa.2018.08.066`

- My contribution according to the contributor role taxonomy system [82] included conceptualization, data curation, formal analysis, investigation, methodology, project administration, software, validation, visualization and writing – original draft preparation.

The aim of this chapter is to introduce reactive particle fluid flows in a one-way coupled Euler-Lagrange approach. In order to validate the simulation of the fluid flow field and the mixing of the components, both *in-situ* studies using MRI and optical investigation are performed. The applicability of the method to reactive particle fluid flows is demonstrated by reactions on the surface of moving particles.

There are several studies that consider adsorption processes by a LBM. Agawar et al. [8] and Manjhi et al. [9] consider adsorption processes on solid particles in a packed bed, as those occur in the adsorption chromatography. They do not resolve the particles of the packed bed, but assume a global reduction of the reactive substance concentration. Thus, they only consider the water and the reactive substance by a coupled Euler-Euler approach that is solved by a LBM. The reduction takes place in each grid cell of the Euler grid. Levesque et al. [83] consider the reactive substance dissolved in the fluid and compute its transport by the LBM with the size-spreading method. For this purpose, the adsorbed density and the free density on the particle surface and the surrounding fluid are considered. The particles are fixed and resolved. The validation of LBM simulations by MRI measurements is already performed by Mantle et al. [84]. They compare their simulation results performed in a packed bed with the measurements and achieve a good agreement. Manz et al. [85] use MRI measurements to validate the simulations of the velocity field through a random packing of spheres. To the authors knowledge, there exist no publications of adsorption processes onto the surface of moving particles computed by LBM.

In this work, the overall objective is a novel Euler-Euler-Lagrange approach to consider adsorption processes on moving particles. The fluids (water and reactive substance) of the three-component flow are described by an Euler approach. As the reactive substance concentration is high, the continuous model is used as it has a better order of convergence and the coupling to the velocity field is easier and more efficient than a Lagrange approach [46, 86]. In contrast, the particles are considered as point particles and described with a Lagrange approach. They are suspended in and carried by the water. The main aim of this paper is to verify the Euler-Euler submodel describing the water and the reactive substance as this is the base of the above mentioned approach. A further goal is to show the feasibility of the Euler-Euler-Lagrange adsorption model.

This chapter is structured as follows. First, the model equations for the three components (water, reactive substance, particles) are named (Section 5.1). Second, the LBM and implementation aspects relevant to this work for both the water and the reactive substance is briefly provided (Section 5.2). The realization of the adsorption by a sink term

is introduced. Third, a quick overview about the measurement of the fluid flow velocity with MRI is given. MRI allows an *in-situ* study during the flow through the meandering channel and is an established and proven method, e.g. in medical as well as in engineering applications. Following, the results of the velocity field (Section 5.4.1) and the fluid mixing experiments (Section 5.4.2) are presented, both obtained by simulations and measurements. The convergence of the reactive substance is confirmed by determining the experimental order of convergence (EOC) (Section 5.4.3). A simulation of the adsorption process on moving particles shows the feasibility of the proposed approach (Section 5.4.5).

5.1 Governing equations and model assumptions

The dynamics of the three-component flow (water, reactive substance, particles) are considered as follows. The carrier fluid water is described with the incompressible and force-free NSE (Section 2.2.1, $\vec{f} = 0$). The reactive substance is assumed to be dissolved in water and is given by the ADRE (Section 2.2.2). The adsorption is considered by the sink as follows. Of the different types of adsorption processes, only the physical sorption is taken into account [87]. That means, by varying e.g. the concentration of the reactive substance, the temperature or the pH value, the adsorbed species can be removed from the surface. This removal is also called desorption. Here, a sudden adsorption to the particle is assumed, as shown e.g. in Manjihi et al. or Anderl et al. [9, 88]. Finally, the sink term in (2.6) is given by

$$R = -K \, c \ \text{in} \ I \times \Omega \, , \tag{5.1}$$

with adsorption coefficient $K \in \mathbb{R} \ [T^{-1}]$. The adsorption is carried out locally at the location of the particles that are described by a discrete particle method. As the load on the particle surface by adsorption is only little compared to the particle mass, both the particle mass and the radius are assumed to be constant. Each particle is treated as a spherical particle and rotation is neglected. The total force in (4.1) is given by the Stokes drag force (4.7),

$$\vec{F}_l(t) = \vec{F}_{\text{Stokes},l}(t) \, . \tag{5.2}$$

Here, the fluid velocity $\vec{u}(t, \vec{x}_l(t))$ is interpolated from the directly surrounding Euler grid points to the discrete particle position $\vec{x}_l(t)$. Certainly, other forces can be considered, e.g. the gravitational force. As they are of minor importance here, their influence is neglected. Here, one-way coupling from the fluid forces to the particles suffices, as the particles are

small and the suspension is assumed to be dilute. Interactions between the particles and the walls can be neglected. During the adsorption processes, the load on the particle surface is neglected as it is little compared to the particle mass. Just the information about the particle position is important for (2.75) as the concentration is reduced at the neighboring Euler grid point next to the particle position.

5.2   Numerical approach and implementation aspects

The computation of the fluids is based on the SRT-LBM [89, 90]. Newton's equations of motion for the particles are solved with the explicit Euler approach [86, 91]. For the fluid flow simulation, the D3Q19 stencil ($q_f = 19$) is used. The corresponding values for $\vec{c}_i$, w_i and c_s are given in Table 2.4. For the reactive mass transport, a D3Q7 stencil ($q_g = 7$) is used. The corresponding properties of the stencils are given in Table 2.3. All simulations are realized in OpenLB (http://www.openlb.net) where the computational performance can be improved by domain decomposition methods [92, 93].

5.3   Velocity mapping by magnetic resonance imaging

In order to verify the simulated flow velocities, MRI measurements such as velocity mapping is provided. More detailed description of the method can be found in the literature [94, 95]. MRI velocity mapping is a well-established method to determine flow. It employs the phase shift induced by moving molecules that are exposed to a flow encoding magnetic gradient field. These phase shifts are proportional to the velocity of the moving fluid. Comparison of encoding and decoding phases allows the computation of so-called velocity maps. They usually consist of two or three dimensional velocity-encoded images and magnitude images (color maps), which reflect the velocity at each pixel or voxel. To obtain this information, the radio frequency excitation pulse of the MRI sequence is followed by a bipolar encoding gradient. The spatially varying encoding gradient pulse $\vec{G} : I \to \mathbb{R}^3$ superimposes the static magnetic field $\vec{B}_0 \in \mathbb{R}^3$ of strength $B_0 \in \mathbb{R}$ of the MRI tomograph. This causes a shift in the Lamor frequency $\omega_L : I \times \Omega \to \mathbb{R}_{>0}$ of the spins, depending on their location $\vec{x}$ in the magnetic field:

$$\omega_L(t, \vec{x}(t)) = \gamma\, B_0 + \gamma\, \vec{x}(t) \cdot \vec{G}(t)\,. \tag{5.3}$$

The gyrometric ratio $\gamma \in \mathbb{R}$ is a natural constant and characteristic for the measured isotope. The integral of (5.3) results in the phase of the precessing magnetization $\phi_k : I \to \mathbb{R}$

with the index $k = 1, 2, 3$ for the different directions in space [94], $\vec{x} = (x_1, x_2, x_3)$ and $\vec{u} = (u_1, u_2, u_3)$. Assuming constant flow, Taylor expansion approximates the integral to

$$\phi_k(t) = \gamma \, M_{0,k} \, x_k(t) + \gamma \, M_{1,k} \, u_k(t) + \phi_{0,k} \, . \tag{5.4}$$

The first term on the right hand side of (5.4) defines the magnetization phase due to the position of a volume element, the second term describes its motion by a constant flow velocity. The additional background phase $\phi_{0,k} \in \mathbb{R}$ depends on the experiment. The zeroth and first order gradient moments $M_{0,k}$ and $M_{1,k} \in \mathbb{R}$ are integrals of the magnetic field gradient, $M_{1,k}$ depends on the length, direction and amplitude of the flow encoding gradient. By measuring two images with different $M_{1,k}$ (e.g. $M_{1,k} = 0$ and $M'_{1,k} \neq 0$), the resulting phase difference

$$\Delta\phi_k(t) = \gamma \, (M_{1,k} - M'_{1,k}) \, u_k$$

can be used to calculate the flow velocity $\vec{u}$ [94].

5.4   Results and discussion

For reasons of simplification, the investigations of the flow properties are carried out in a passive mixer, a simple meandering channel. Passive mixing takes place by diffusion and advection. Static mixers usually have a simple structure and are easy to handle [96]. A direct comparison of the simulation results with the measurements is possible. To investigate the adsorption processes in the mixer by simulation, the flow field and the mixing of the fluids are of particular interest. Table 5.1 gives a short overview of the individual experiments that are all performed by the simulations. In addition, the velocity field and the fluid mixing are examined by the measurements to verify the simulations. Figure 5.1 shows the static mixer that is used for the velocity and adsorption experiments (Section 5.4.1, Section 5.4.5). It is a serpentine mixer with 90 degree curves and a rectangular channel cross section of 1.0×10^{-3} m to 2.0×10^{-3} m. It consists of two inlets, one outlet and has a total length of 2.7×10^{-2} m. For the fluid mixing, the geometry is slightly modified as explained in Section 5.4.2. The EOC is investigated in a T-shaped mixer that is used for reasons of simplicity (Section 5.4.3). In the following, the setups of the different simulations and measurements are described.

experiment	velocity field	fluid mixing	EOC	adsorption
Subsection	5.4.1	5.4.2	5.4.3	5.4.5
simulation	yes	yes	yes	yes
measurement	MRI	ink solution	no	no
geometry	Figure 5.1	Figure 5.1 (modified)	T-shape	Figure 5.1

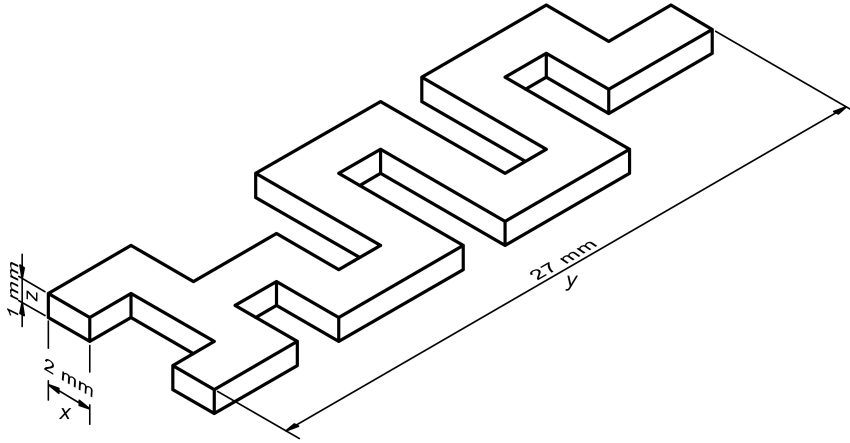**Table 5.1:** Overview of the different experiments.

Figure 5.1: Geometry of the static serpentine mixer with a rectangular channel cross section of 1.0×10^{-3} m to 2.0×10^{-3} m and a total length of 2.7×10^{-2} m.

5.4.1 Velocity field experiments

As the velocity field is the base of all further investigations concerning the fluid mixing or the adsorption processes, its correct computation is of great importance. The verification of the simulation results is carried out by MRI measurements. Since the phosphate solution is a highly dilute aqueous solution, water is used for both the simulations and the measurements, with density $\rho = 1.0 \times 10^3 \, \mathrm{kg \, m^{-3}}$ and dynamic viscosity $\mu = 10^{-3} \, \mathrm{kg \, m^{-1} \, s^{-1}}$ and the volumetric flow $\dot{V} = 1.0 \times 10^{-7} \, \mathrm{m^3 \, s^{-1}}$ at the outlet. Further physical model parameters are shown in Table 5.2. The parameter $L \in \mathbb{R}_{>0}$ is the characteristic length and equals the hydraulic diameter of the flow channel in the mixer. The characteristic velocity $U \in \mathbb{R}_{>0}$ corresponds to the maximum flow velocity of the fluid at the outlet of the mixer assuming a Poiseuille profile. In a channel with a rectangular cross section, the mean velocity is computed by U as described in [97] and results in the Reynolds number Re = 66.5.

parameter	values
L	1.33×10^{-3} m
U	9.96×10^{-2} m s^{-1}
$\dot{V}$	1.00×10^{-7} m^3 s^{-1}
Re	66.5

Table 5.2: Model parameters for the velocity field experiments.

Setup of the LBM simulations

For the LBM simulation of the NSE, the spatial discretization in physical units is set to $\Delta x = 2.5 \times 10^{-5}$ m, the temporal discretization to $\Delta t = 1.3 \times 10^{-6}$ s. The value of the dimensionless relaxation time $\tau' = 0.506024$ is fixed and remains unchanged for both the variations in time and space resolution. Standard boundary conditions are applied for the simulation. Dirichlet boundary conditions for the velocity computation are defined at both inlets, at which a Poiseuille inflow profile is assumed. The maximum velocity of $0.5\,U$ is reached after a certain build-up period at the inlet. At the outlet, the same boundary condition applies for the pressure with a given density of one. On the channel wall, half-way bounce-back conditions are defined. The steady state is obtained and the simulation is stopped after the residual of the maximum velocity in the mixer is reached and a certain physical time is passed.

Setup of the MRI measurements

The real mixer for the velocity field experiments (see Figure 5.1) as well as the connectors for the inlets and the outlet are fabricated by a 3D printer using fused deposition modeling. The connectors open parallel to the flow plane in the mixing channel. The top of the channel is sealed by an acrylic glass to provide optical transparency into the mixer. The glass is fixed by a low viscous acrylic adhesive that is cured with ultraviolet light. To measure the flow velocities, water is fed into the two inlets of the mixer.

The experimental verification of the simulated velocities is provided by MRI with a velocity mapping method (see Section 5.3). The *FLOWMAP_velocity* pulse sequence (Bruker BioSpin GmbH, Rheinstetten, Germany) uses a bipolar flow encoding gradient that is applied in between the radio frequency excitation pulse and the signal readout (see Section 5.3). The parameters used for image acquisition are summarized in Table 5.3. The MRI measurements are performed on a 200 MHz MRI tomograph (Bruker Avance 200 SWB, Bruker BioSpin

GmbH, Rheinstetten, Germany) with a magnetic flux density of 4.7 T. The tomograph has a vertical bore of 1.5×10^{-1} m. In the radio frequency probe head with an inside diameter

parameter	coronal slice	axial slice
matrix	128×256	128×128
echo time	7×10^{-3} s	7×10^{-3} s
recycle delay	1 s	1 s
number of averages	2	4
field of view / 10^{-3}	13×26	5×5
slice thickness	0.5×10^{-3} m	1.0×10^{-3} m

Table 5.3: MRI sequence parameters for the flow velocity measurements.

of 2.5×10^{-2} m the mixer is fixed vertically. To ensure equal volumetric flow rates at the two inlets of the mixer, two high-performance liquid chromatography (HPLC) pumps are utilized (HPLC Pump P580, Dionex Softron GmbH, Germering, Germany). The high accuracy and low pulsation of the flow is one main advantage of these pumps that are often used in chromatography. The velocity measurements are performed in a coronal slice (x-y plane) in the middle of the mixing channel and in an axial slice (x-z plane) between two 90 degree curves of the mixer. For each component of the velocity vector, a single measurement with a different direction of the flow encoding gradient is carried out.

Results and discussion

Figure 5.2 to Figure 5.4 show that the velocity magnitude of the simulation is in a very good agreement with the one of the measurements. Deviations may occur due to the fact that the planes of the signal detection in the MRI measurements are placed by optical criteria. Furthermore, the MRI signal is measured in a layer of 5.0×10^{-4} m thickness for the coronal slice, respective 1.0×10^{-3} m thickness for the axial slice. As the shape of the real mixer may differ from its original geometry within the scope of the 3D-print precision, that may influence the real flow field. Nevertheless, the flow field analysis in the coronal and axial slice shows sufficiently good agreement in both the MRI measurements and the simulation.

Figure 5.2 shows the magnitude of the velocity $\vec{u}$ by simulation (a) and measurement (b) in the coronal cut of the channel (x-y plane, $z = 5.0 \times 10^{-4}$ m). In contrast to the simulation, there are dark blue areas within the channel in the experiments. They appear in the corners and at the edge of the mixing channel and are caused by air bubbles that cannot be removed

by tapping against the mixer. Since the air bubbles are small and located on the walls, their influence on the fluid flow is negligible. The connections of the hoses attached to the inlets and the outlet influence the flow profile, too. Therefore, exact comparison of measurement and simulation is not possible. Nevertheless, the velocity magnitude ranges to 1.4×10^{-1} m s^{-1} in both cases and is represented by a color scale that goes from blue to red in Figure 5.2. Red colored parts depict high velocities of about 1.1×10^{-1} m s^{-1} to 1.4×10^{-1} m s^{-1}, blue parts symbolize low values of about zero to 4.0×10^{-2} m s^{-1}. For both experiment and simulation, the flow velocity at the inner curve is larger than the one on the outside. All in all, the results show very good agreement.
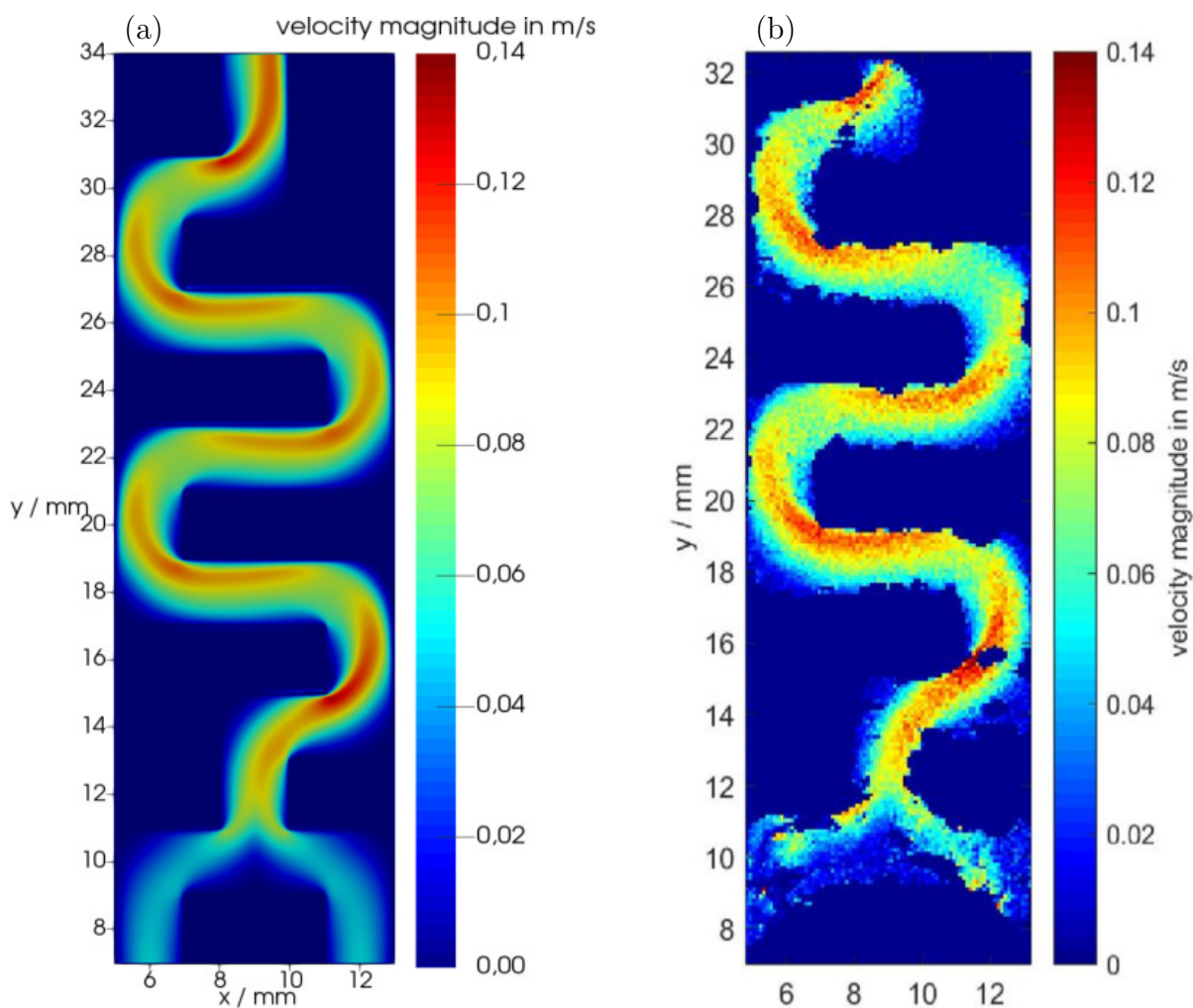
Figure 5.2: Magnitude of the simulated (a) and measured (b) velocity $\vec{u}$ in the coronal cut (x-y-plane, $z = 5.0 \times 10^{-4}$ m). The dark blue areas within the channel are obvious in (b) and are caused by air bubbles at the walls.

Referring to the axial cut between two 90 degree curves in the middle of the mixer (x-z-plane, $y = 2.0 \times 10^{-2}$ m), the velocity components u_x, u_y, u_z of the simulation results are

depicted in Figure 5.3 (a)-(c), corresponding MRI results are shown in Figure 5.3 (d)-(f). In Figure 5.3 (d)-(f), the points outside the rectangular channel cross-section arise from noise of the MRI measurements and are not taken into account. In Figure 5.3 (a) and (d), u_x is shown.
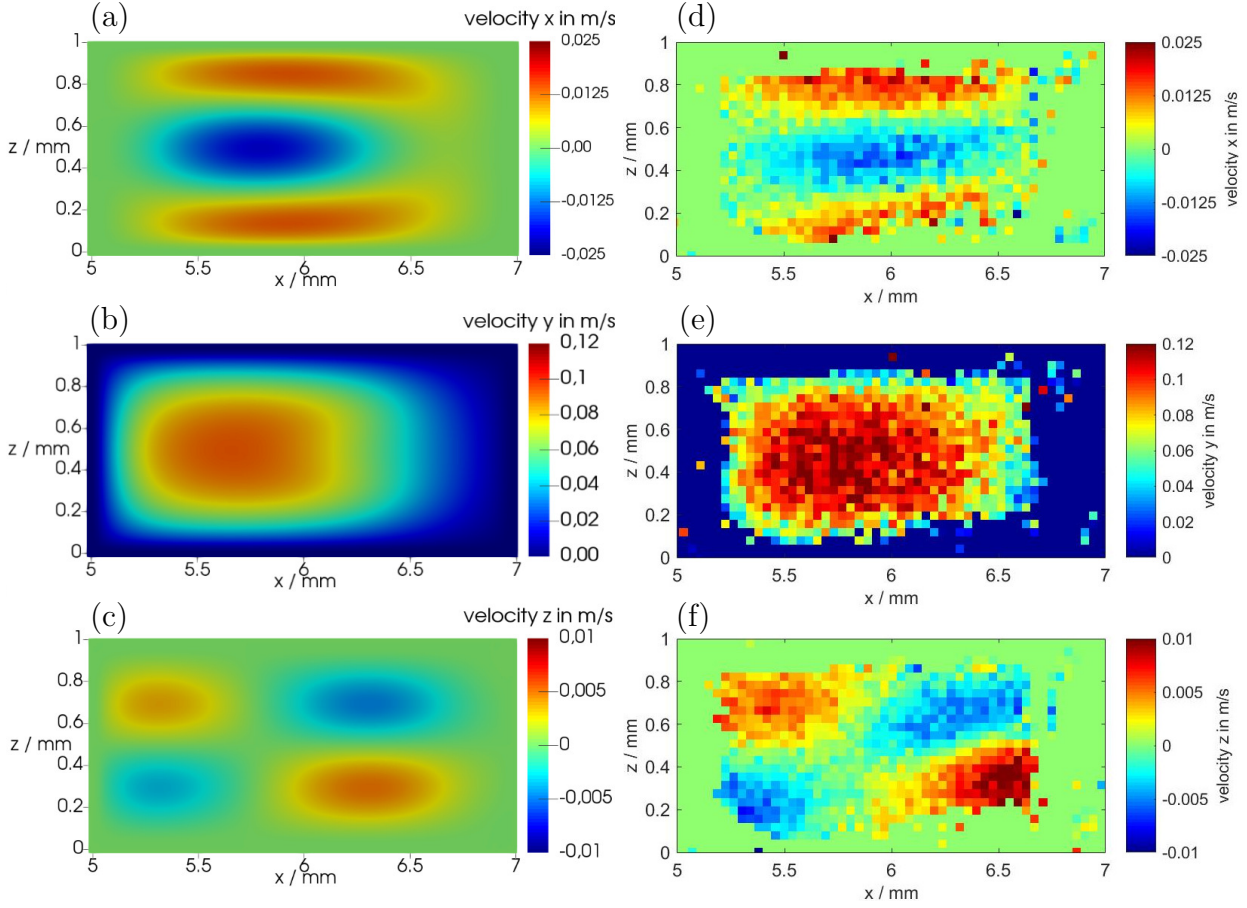

Figure 5.3: Velocity components u_x, u_y, u_z of $\vec{u}$ (from top to bottom) in the axial cut (x-z-plane, $y = 2.0 \times 10^{-2}$ m) by simulation (a)-(c) and MRI measurements (d)-(f).

Its values range from -2.5×10^{-2} m s^{-1} to 2.5×10^{-2} m s^{-1} for both the simulation and the MRI results. On top as well as at the bottom, the values are larger or equal to zero, negative values occur in the middle of the channel height. The results coincide very well with those of the simulation. The maximum of the velocity component u_y, depicted in Figure 5.3 (b) and (e), is shifted more to the outside of the curve (to the left, $x \approx 5.7 \times 10^{-3}$ m). This shift is based on the centrifugal forces that occur in the curves. At the wall, the values tend to zero but still remain positive. Differences between the measured and simulated flow velocities are most noticeable for u_y, the main flow direction at the position of the considered cross-sectional area. The maximum values of the MRI measurement (dark red colored in Figure 5.3 (e), about 1.1×10^{-1} m s^{-1}) are larger compared to those of the simulation (red colored in Figure 5.3 (b), about 1.0×10^{-1} m s^{-1}). The relative error is about 9%. Besides

slight fluctuations in the feed pressure, differences in the results of the measurement and the simulation might be caused by inaccuracies in the 3D-printed mixer geometry. Considering the velocity component u_z in Figure 5.3 (c) and (f), the range is between -1.0×10^{-2} m s^{-1} and 1.0×10^{-2} m s^{-1} and is a lot smaller than in case of the other two components. The z-plane is divided into four regions. u_z is positive in the upper left and lower right quarter, whereas it is negative in the bottom left and upper right parts. On the whole, the velocity components of the MRI measurements are in good agreement with the simulation results in the axial cross-sectional area of the mixer.

In addition to Figure 5.2 and Figure 5.3, the quantitative agreement between of MRI measurement and simulation is highlighted in Figure 5.4 by the plot of the magnitude of $\vec{u}$ over x for $y = 2.0 \times 10^{-2}$ m and z $= 5.0 \times 10^{-4}$ m. It is evident that the maximum of the velocities, that are in good accordance, are shifted to smaller x-values because of the right turn of the mixer.
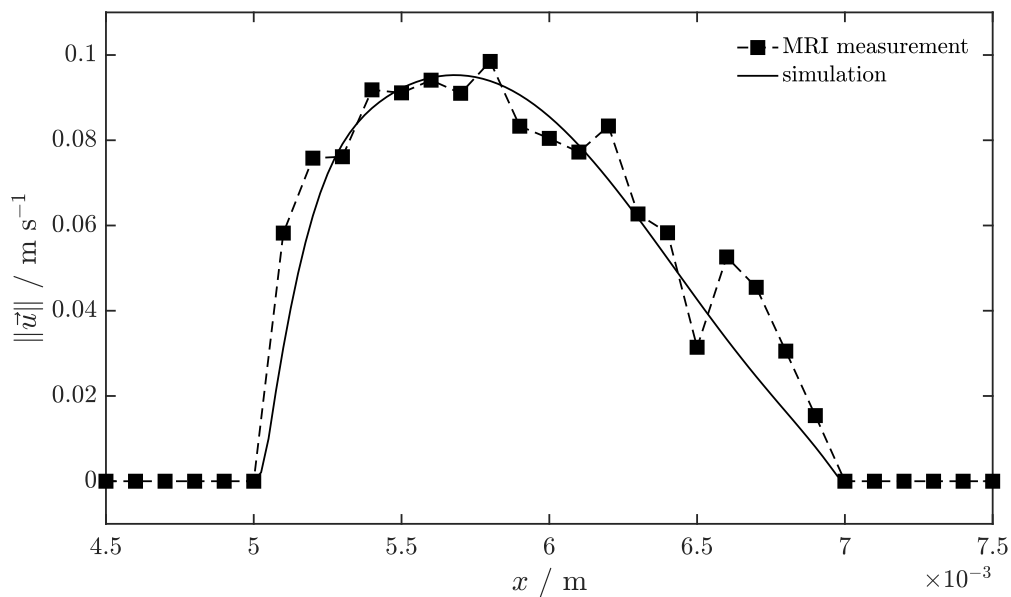
Figure 5.4: Magnitude of the velocity $\vec{u}$ over x for $y = 2.0 \times 10^{-2}$ m and $z = 5.0 \times 10^{-4}$ m obtained by MRI measurement and simulation.

The projection of $\vec{u}$ on the axial cross-section plane, depicted by black arrows in Figure 5.5, shows a symmetrical double vortex extended across the entire cross section. This vortex is called Dean vortex [98].

5.4.2 Fluid mixing experiments

In order to gain insight into the reactive substance transport due to mixing effects in the mixer, the mixing process is examined by comparison between simulation and measurement.
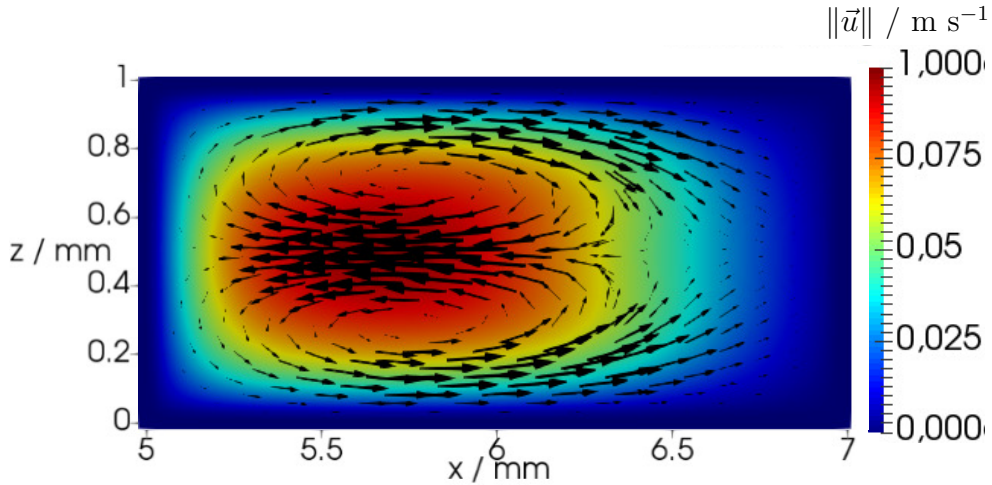
Figure 5.5: The Dean vortex is visualized by the velocity vectors projected into the cross-sectional plane that is colored by the magnitude of $\vec{u}$.

An ink solution and water are used to enable optical examination. To qualitatively compare both experiments, it does not matter whether an ink or a phosphate solution is utilized as the ink pigments are chemically dissolved in the water. The diffusion coefficients of the ink molecules and the phosphate ions are of the same order and set to $D = 1.0 \times 10^{-9}\,\mathrm{m^2\,s^{-1}}$. To achieve a volume flow of $3.30 \times 10^{-8}\,\mathrm{m^3\,s^{-1}}$ at the outlet, the maximum velocity $U = 3.32 \times 10^{-2}\,\mathrm{m\,s^{-1}}$ is chosen. The physical model parameters are shown in Table 5.4.

parameter	values
L	1.33×10^{-3} m
U	3.32×10^{-2} m s^{-1}
$\dot{V}$	3.30×10^{-8} m^3 s^{-1}
Re	22.21

Table 5.4: Model parameters for the fluid mixing experiments.

Setup of the LBM simulations

First, the velocity field is computed as described in Section 5.4.1 with $\tau' = 0.50602$ and $\Delta x = 5.0 \times 10^{-5}\,\mathrm{m}$, $\Delta t = 5.2 \times 10^{-5}$ s. The velocity field is stored for each grid point of the lattice. Subsequently, it is linked to the computation of the concentration transport according to Section 2.3.7. For both the velocity and the concentration simulation, the space discretization is the same. In case of the concentration transport, the time resolution ($\Delta t = 4.5 \times 10^{-5}$ s) is larger than in the velocity simulation. This results in $\tau'_g = 0.5008$

which is just large enough to avoid numerical instabilities that occur for values of τ'_g towards 0.5.

At the right inlet where the reactive substance enters the mixer, a Dirichlet boundary condition is set with fixed value for the concentration as proposed by Zou and He [37]. At the outlet, a convection boundary condition is chosen that computes g_j at the boundary nodes by interpolation of the adjacent nodes, see Trunk et al. [46] and Junk and Yang [39]. As the wall of the mixing channel is impermeable for the concentration, a bounce-back condition is employed for the walls as well as at the second inlet where the water flows in.

Setup of the ink experiments

For the real mixing experiments, a predecessor mixer model similar to the one in Figure 5.1 is used. The main differences are the dead volume in the rear part (Figure 5.6) and the connections perpendicular to the mixer plane. For the mixing experiments, a syringe pump (Twin Syringe Pump 33, HARVARD Apparatus) is utilized. In order to investigate the mixing process in real experiments, the mixer is vertically mounted to ensure similar conditions to the velocity measurements in the MRI tomograph. Optical experiments show no differences in the mixing quality depending on the mounting.

Results and discussion

The comparison of Figure 5.6 (a) and (b) shows that the simulation of the reactive substance transport (a) coincides well with the mixing experiments with ink and water (b). In the simulation, the reactive substance enters the mixer at the right inlet. As already mentioned in Section 5.4.2, the utilized geometries of the simulation and the ink experiment differ. In the real mixer, the air cannot escape the dead volume at the end of the mixer. As this does not disturb the mixing process in the rest of the channel, it is not significant for the performed investigations.

In Figure 5.6 (b), the mixer is presented in top view. Depending on the direction of the mixer's curve, the interfaces of the water and the ink are pushed one into the other. At the transition zone, the violet coloring is more transparent because the layers of the ink solution are smaller compared to the parts where no transition of ink and water takes place. Because of the transparency of water, the observer is able to see into the mixer and does not only look at the upper layer of the mixed components. As a result, the mixing width seems to be more pronounced compared to the simulation results in Figure 5.6 (a), left, where the horizontal center cross-sectional plane is depicted. In Figure 5.6 (a), right, the distribution of
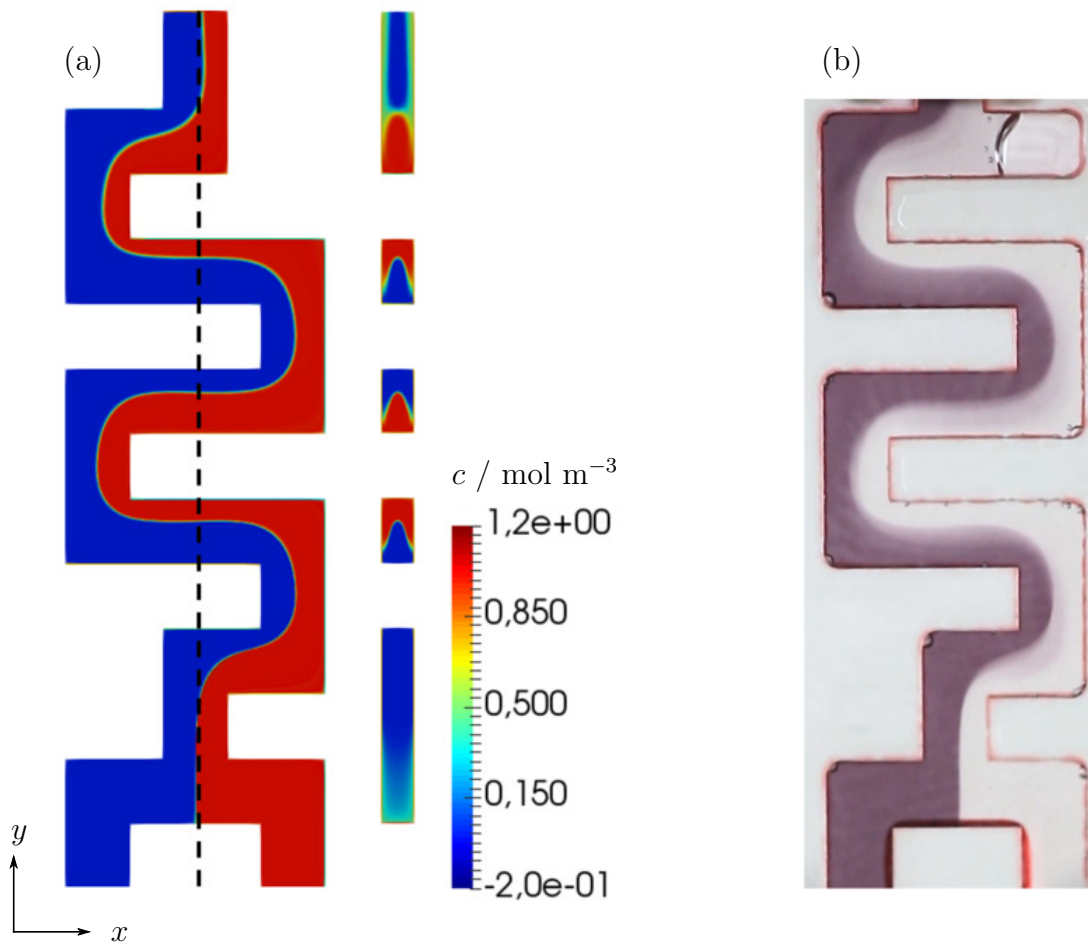
Figure 5.6: Fluid mixing by simulation (a) (water and reactive substance) and ink experiment (b) (water and ink solution) with a volume flow of $3.3 \times 10^{-8}\,\mathrm{m^3\,s^{-1}}$ and a maximum velocity of 3.32×10^{-2} m s^{-1} at the outlet. An air bubble is trapped in the dead volume at the end of the mixer.

the reactive substance and water is illustrated within the cross section normal to the x-axis of the mixer (black dashed line). In the horizontal parts of the channel, a clear interface of the two fluids is visible due to the centrifugal forces. The diffusive mixing occurs as a fluent transition from high (red colored) to low (blue colored) reactive substance concentration. The layering of the two components points to a convective mixing phenomenon through the 90 degree deflections and indicates the Dean effect. Both experiment and simulation shows the layering of the components in a very well manner.

5.4.3   Error determination of the reactive substance

To confirm that the simulation of the reactive substance converges, a series of five simulations is performed to determine the EOC of the mean reactive substance concentration at the outlet

of the T-shaped mixer. This geometry is used for reasons of simplification. In contrast to the serpentine mixer, it consists of a straight channel instead of a meandering one. The velocity and concentration computation is performed as already described in Section 5.4.2 with $U = 1.00 \times 10^{-2}\,\mathrm{m\,s^{-1}}$, respectively with a volume flow of $1.03 \times 10^{-8}\,\mathrm{m^3\,s^{-1}}$ at the outlet. While the relaxation time $\tau'_g = 0.5008$ remains constant for all five simulations, both the space ($\Delta x = 1.0 \times 10^{-4}$ m) and the time resolution ($\Delta t = 2.0 \times 10^{-3}$ s) are refined successively by diffusive scaling [19]. That means the refinement is conducted by $\Delta x\, h^{-1}$ and $\Delta t\, h^{-2}$ for the spacing $h \in \{1,\, 2,\, 3,\, 4\}$. The relative error

$$err(h) := \sqrt{\frac{\left(\sum_{\Omega_{h,\mathrm{outlet}}} \frac{c(t,\vec{x})}{\#\Omega_{h,\mathrm{outlet}}} - \sum_{\Omega_{8,\mathrm{outlet}}} \frac{c(t,\vec{x})}{\#\Omega_{8,\mathrm{outlet}}}\right)^2}{\left(\sum_{\Omega_{8,\mathrm{outlet}}} \frac{c(t,\vec{x})}{\#\Omega_{8,\mathrm{outlet}}}\right)^2}}$$

is the error of the computed mean reactive substance concentration

$$\bar{c}_h = \sum_{\Omega_{h,\mathrm{outlet}}} \frac{c(t,\vec{x})}{\#\Omega_{h,\mathrm{outlet}}} \tag{5.5}$$

for the spacing h with respect to the computed mean reactive substance concentration of the spacing $h = 8$ at the outlet.

It is confirmed that the simulation of the reactive substance converges by computing the EOC at the outlet of the T-shaped mixer. The values of $\bar{c}_h$ obtained at the outlet are listed in Table 5.5 and converge towards 0.5. Since equal amounts of water and reactive substance are mixed, this value is reasonable. In Figure 5.7, $err(h)$ is depicted as a function of h in a

h	$\bar{c}_h$
1	0.480458
2	0.494237
3	0.496553
4	0.497250
8	0.498994

Table 5.5: Mean concentration of the reactive substance at the outlet of a T-shaped mixer computed with different spacings h.

double logarithmic representation. It decreases with increasing lattice refinement. The EOC equals the slope of a straight line in the double logarithmic plot. This reduction corresponds

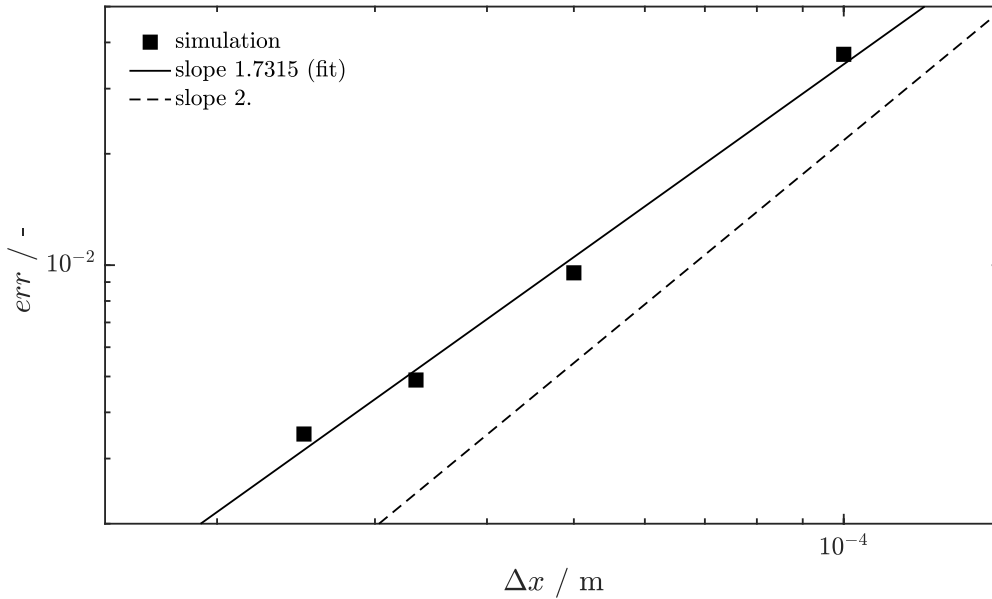to the expected value of two for the EOC referring to the calculation of the ADRE with LBM [99].

Figure 5.7: Double logarithmic representation of the relative error $err(h)$ as a function of the resolution h with EOC = 2.

5.4.4 Validation of a global sink by an analytical solution[1]

To validate the reactive substance transport inclusive reactions by an error study, a 3D test case of transport and reaction is chosen. The simulation is compared with the analytical solution given by Bear [100] and Van Genuchten and Alves [101]:

$$c_{\text{analytic}}(t,x) = \frac{c_0}{2} \left(\exp\left(\frac{x\,(u_1 - U)}{2\,D} \right) \text{erfc}\left(\frac{x - U\,t}{2\,\sqrt{D\,t}} \right) + \exp\left(\frac{x\,(u_1 + U)}{2\,D} \right) \text{erfc}\left(\frac{x + U\,t}{2\,\sqrt{D\,t}} \right) \right),$$

$$(5.6)$$

with $U = \sqrt{u_1^2 + 4\,K\,D}$ and complementary error function denoted as erfc.

The size of the domain is $(50, 5, 5)$ m for the (x, y, z)-direction, Figure 5.8. The initial concentration is $c_{\text{in}} = 1\,\text{mol}\,\text{m}^{-3}$ at the inlet $(x = 0\,m)$ and $c = 0\,\text{mol}\,\text{m}^{-3}$ in the rest of the domain, with $D = 0.1667\,\text{m}^2\,\text{s}^{-1}$, constant velocity $\vec{u} = (0.01, 0, 0)\,\text{m}\,\text{s}^{-1}$ and globally executed reaction $R = K\,c$ in (2.6) with $K = -0.01\,\text{s}^{-1}$ and $K = 0\,\text{s}^{-1}$. The boundaries in x-direction are fixed concentration boundary conditions, in y- and z-direction, bounce-back is applied. The simulation duration is $t = 200\,\text{s}$. The dimensionless relaxation time is $\tau_g' = 0.542$ and is kept constant for the grid convergence study by diffusive scaling.

---

[1]The contents of this section was generated during the research stay at Paul Scherrer Institute, Villigen, Switzerland, and is not part of [91].
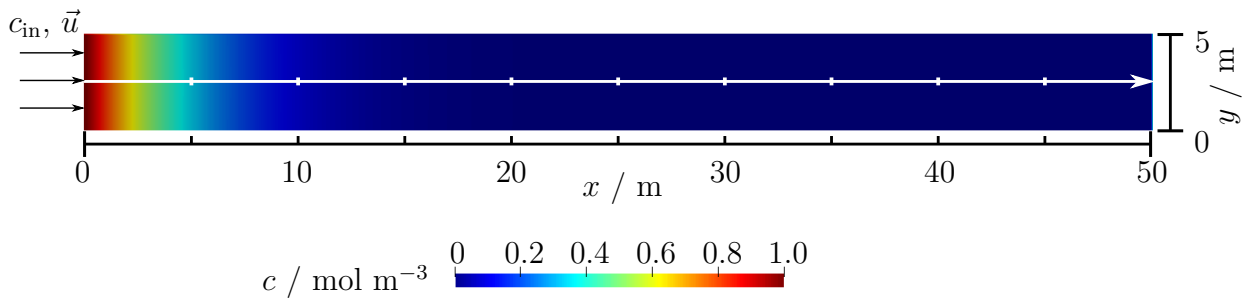
Figure 5.8: Setup of the validation case for the global sink.

The error study is conducted at nine points ($x = 5, 10, \ldots, 45\,\text{m}$, $y = z = 2.5\,\text{m}$). The relative error in concentration $err_c(h)$ is computed by

$$err_c(h) := \sqrt{\frac{\sum_{x=5,\,10,\,\ldots,\,45\,\text{m}} \left(c_{\text{analytic}}(200\,\text{s}, x) - c_h(200\,\text{s}, x) \right)^2}{\sum_{x=5,\,10,\,\ldots,\,45\,\text{m}} \left(c_{\text{analytic}}(200\,\text{s}, x) \right)^2}}, \tag{5.7}$$

at nine points within the simulation domain and with grid resolution $h = \{25, 50, 100, 150, 200\}$ and comparison to the analytical solution. It is smaller than about $0.1\,\%$ for $K = -0.01\,\text{s}^{-1}$. For no sink ($K = 0\,\text{s}^{-1}$), it is smaller than about $0.01\,\%$. The EOC is given by the slope of the error fit line of $err_c(h)$ over Δx in the double-logarithmic plot in Figure 5.9 and is about 1.2. This might result from bounce-back boundaries. Nevertheless, the simulation converges in both cases.

5.4.5 First adsorption simulation

To perform the simulation of the adsorption on moving particles suspended in water, the maximum velocity at the outlet is set to $U = 1.00 \times 10^{-2}\,\text{m s}^{-1}$, $\text{Re} \approx 7$. This corresponds to a volume flow of $1.03 \times 10^{-8}\,\text{m}^3\,\text{s}^{-1}$ at the outlet, the dimensionless relaxation time is $\tau_g' = 0.5016$. The velocity and concentration simulation is performed as already described in Section 5.4.2 with $\Delta x = 5.0 \times 10^{-5}\,\text{m}$ and $\Delta t = 1.0 \times 10^{-3}\,\text{s}$. The adsorption is modeled by a linear reduction of the reactive substance concentration at the Euler grid point that is the direct neighbor of the discrete particle positions. In the experiment, the adsorption rate (2.75) is set to $K = 0.1\,s^{-1}$.

After the steady state in the concentration simulation is reached, the particles are generated at the left inlet of the mixer. Before the particles are injected, the initial mean concentration at the outlet is referred to as $\bar{c}(0)$. The temporal decrease in the concentration is given by $\bar{c}(t)$. During a time of 60 s, every hundredth of a second 38 particles are
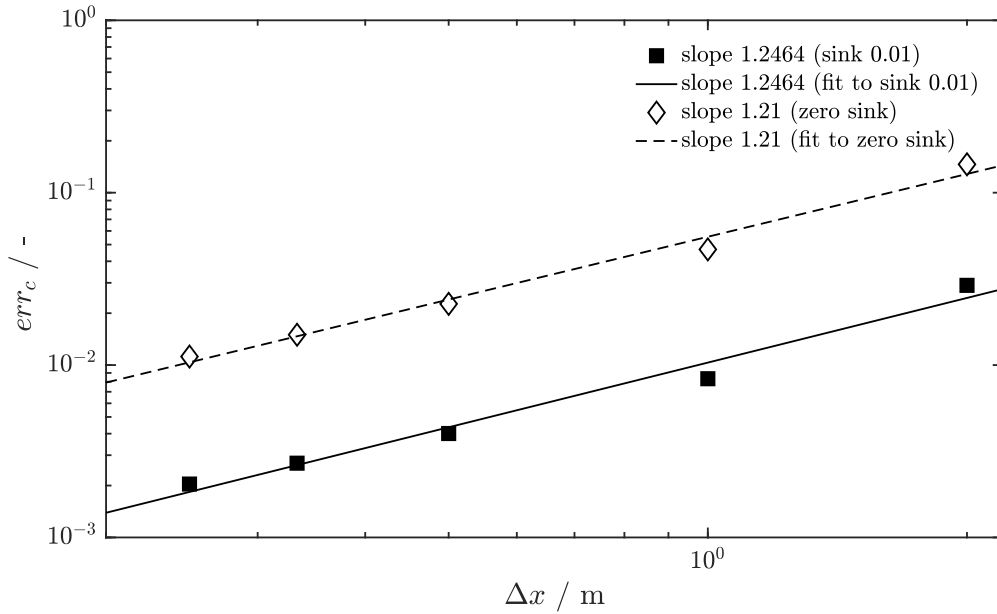
Figure 5.9: The relative error err_c of the concentration computed at nine points within the simulation domain is smaller than about $0.1\,\%$ for $K = -0.01\,\mathrm{s}^{-1}$. For no sink ($K = 0\,\mathrm{s}^{-1}$), it is smaller than about $0.01\,\%$.

generated at the left inlet of the mixer until a total amount of 76,836 particles is reached. The particles are assumed to be ideal round with radius $r_l = 9.5 \times 10^{-5}$ m and density $\rho_l = 3.25 \times 10^3\,\mathrm{kg\,m^{-3}}$.

The results of the first simulation of the adsorption process on moving particles in the meandering mixer are presented. By increasing number of simulated particles, the concentration decreases at the outlet of the mixer. Figure 5.10 shows the temporal progress of the adsorption concentration in response to an injection pulse of particles. The maximum number of 44,321 particles within the mixer is reached at about 20 s, then the number decreases to zero during the next 40 s. Six seconds after the first particle injection, the relative concentration $\bar{c}(t)/\bar{c}(0)$ decreases. With increasing particle number the relative concentration decreases until it reaches its minimum value of about 0.9 after 26 s.

5.5   Conclusion

In this work, an adsorption model is proposed that consists of a novel Euler-Euler-Lagrange approach. It considers adsorption processes of a solute (reactive substance) on moving particles suspended in water. The experiments are performed in a static mixer. The mixer
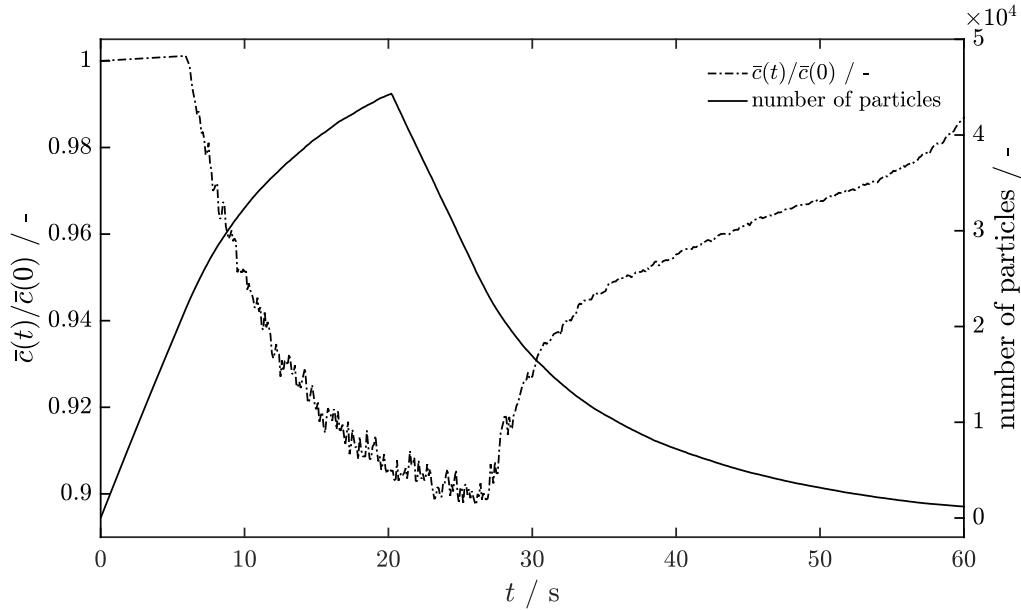
Figure 5.10: Response to an injection pulse: temporal progress of the first adsorption experiments.

is chosen as it is an appropriate geometry to perform both the simulations and the measurements. As the fluid flow field and the mixing of the three components influence the adsorption, the verification of the simulations are conducted by measurements.

First, the models for the three components were introduced. The water flow was modeled by the NSE, the reactive substance concentration by the ADRE. The adsorption was modeled by a sink term in the ADRE. The Henry adsorption isotherm was used as a simple linear adsorption model. All particles were assumed to be point particles and described with a discrete particle method. Their trajectories were modeled with Newton's equation of motion. Second, both the velocity field and the reactive substance concentration in the mixer were simulated using a LBM. The realization of the sink term was introduced. The adsorption was performed at the neighbor point on the Euler grid next to the position of the Lagrange particles.

The simulation and the MRI measurements of the velocity field experiments show good accordance in the magnitude of the velocity (in the coronal cross-section) and its components (in the axial cross-section). The results match very well, qualitatively and quantitatively. The largest differences are most noticeable for the main flow direction u_y, the relative error is about 9%. For the fluid mixing, experiments were conducted with water and an ink solution. Simulations and measurements show a similar concentration profile in the mixer. In the cross section of the simulation result, the convective and the diffusive mixing of the fluid components is visible. In the ink experiments, there are transparent violet colored areas

that indicate the layering of the ink and the water. Then, the EOC of the reactive substance transport was confirmed to be two. Based on this, the adsorption process of a phosphate solution on in water suspended particles was conducted in a first numerical experiment. The temporal progress of the change in the reactive substance concentration by the adsorption processes depending on the particle number shows the feasibility of the chosen approach.

As the measurements of the velocity field and the fluid mixing show, the models and the simulations of the novel Euler-Euler-Lagrange approach perform very well. In addition, the computation of the EOC for the concentration confirms this statement. The simulation of the adsorption process on the surface of the moving particles proves the feasibility of the chosen approach by a real application. Based on this results, the received knowledge can be transferred to other applications, e.g. the high gradient magnetic separator.

6 Two-way coupled volume-averaged reactive particle fluid flows

- The contents of this chapter are accepted for publication in the following reference and are adapted for this dissertation:
  M.-L. Maier, R. A. Patel, N. I. Prasianakis, S. V. Churakov, H. Nirschl, and M. J. Krause. "Coupling of multiscale lattice Boltzmann discrete-element method for reactive particle fluid flows". In: *Phys. Rev. E* 103 (3 2021), p. 033306. DOI: `10.1103/PhysRevE.103.033306`

- Acknowledgments referring to this reference:
  The authors thank the Karlsruhe House of Young Scientists (KHYS) of the Karlsruhe Institute of Technology (KIT) that supported Marie-Luise Maier by the Research Travel Grants to Junior Researchers to stay at Paul Scherrer Institute (PSI), Switzerland for a research period of three months to work within the framework of her research project.

- My contribution according to the contributor role taxonomy system [82] included conceptualization, data curation, formal analysis, investigation, methodology, project administration, software, validation, visualization and writing – original draft preparation.

In this chapter, the volume-averaged equations are applied to reactive particle fluid flows. This is the key difference between the previously proposed model and the present model. The method is applied to the single particle sedimentation in a steady fluid inclusive grid convergence studies. Comparative studies are performed for validation purposes of the reactive particle fluid flow simulations. Finally, a demonstration case shows the potential of the model.

According to Blais et al. [4], appropriate equations that model the fluid flow of dense particle fluid flows or flows in porous media are the VANSE as they allow to handle large porosity gradients. Höcker et al. [56] developed the model of Blais et al. [4] for Euler-Euler multi-phase flows with both spatially and temporally fluctuating particle concentrations. Most studies conducted on reactive flows previously has been focused on the static solid particles which are considered as adsorbent media in packed bed reactor [5–7]. Reactions to moving particles are rare [11]. The use of consistent equations derived from volume averaging theory for reactive particle fluid flows is the key difference between the previously proposed models and the present model. In addition, we demonstrate that the proposed model is numerical grid convergent which as previously been not shown in any proposed model which uses LBM for equations in the Eulerian frame.

To conclude to our knowledge at present, there is no modeling framework for fully coupled multi-scale LBM and DEM for reactive particle fluid flows. Key contribution of this study is a robust LBM-based Euler-Lagrange algorithm for reactive particle fluid flows which handles a two-way coupling and a demonstrated numerical convergence. In this model the flow of the Newtonian fluid and the reactive transport processes are not resolved around the disperse particles but rather treated in a continuous framework through a volume-averaging procedure. The multi-scale problem originate from the fact that the discrete particle size is much smaller than the macro-scale domain of interest for fluid flow [102].

This chapter is structured as follows. First, the governing equations for the three physical processes are named (Section 6.1). It is followed by details about the numerical model and implementation aspects (Section 6.2). Finally, a series of benchmarks are presented to offer validation of the model and a demonstration case is simulated to show the potential of the developed model (Section 6.3).
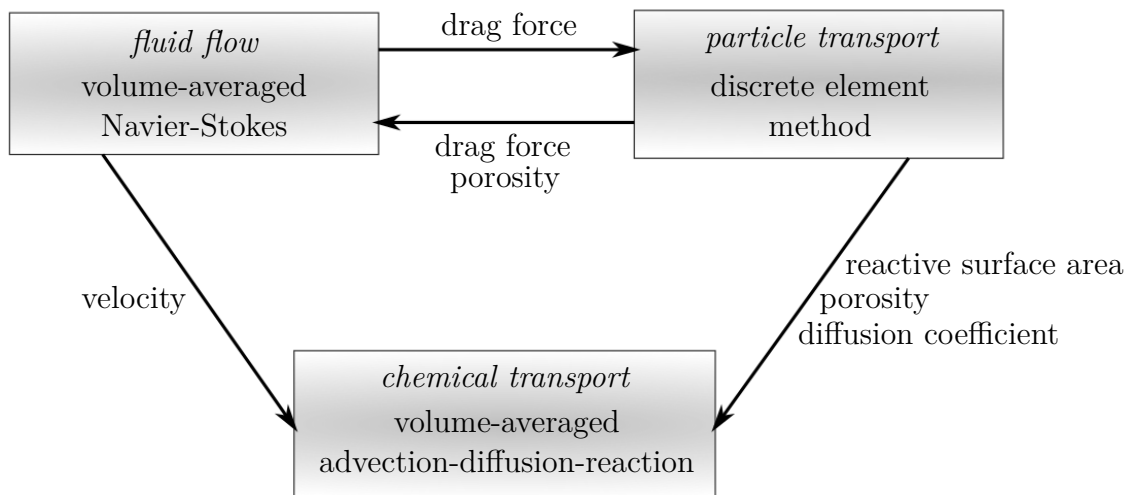
Figure 6.1: Scheme of the fully coupled system of fluid, reactive substance and particles.

6.1 Governing equations and model assumptions

The model consists of three components viz., fluid (water), reactive substance dissolved in water and solid suspended particles. The flow of water and the transport of the reactive substance is modeled within the framework of Euler mechanics, the particles with the Lagrange approach. Interaction with solid particles within the control volume is considered using volume-averaging theories. The fluid flow is governed by the VANSE (Section 3.1.1) which recover the Darcy-Brinkman equations in systems with a sufficiently slow fluid flow. The reactive mass transport is modeled by the VAADRE (Section 3.1.2) in absence of electro-kinetic effects. The particles are considered spherical and their motion is modeled using the DEM (Chapter 4). This model provides a very accurate coupling between Euler and Lagrange models. The governing equations of the fluid, the reactive mass transport and the particles are fully and accurately coupled to account for the relevant processes, Figure 6.1. For the particles, the interaction with the fluid flow is governed by a drag force. The effect of the particles on the fluid is realized through a change of porosity and drag force. The effect of the particles on the fluid is represented through a change of porosity and drag force. For the reactive mass transport equation, the porosity is included in the diffusion coefficient, the formulation of the reaction term depends on the specific surface area. The dispersion in the diffusive solid phase is neglected. In the following, the detailed formulation of the adsorption term in the VAADRE, of the considered forces in the DEM and of the coupling of the component is presented.

6.1.1 Adsorption reaction

In this study, the reaction term $R : I \times \Omega \to \mathbb{R} \, [\mathrm{N \, L^{-3} \, T^{-1}}]$ in (3.3) accounts for the adsorption reaction occurring at the surface of the particles. The adsorption process is considered as a heterogeneous reaction taking place at the fluid-solid interface. This reaction can be written as

$$R = -k \, A_s \, c \,. \tag{6.1}$$

Here, $A_s : I \times \Omega \to \mathbb{R} \, [\mathrm{L^{-1}}]$ is the specific surface area and $k \in \mathbb{R} \, [\mathrm{L \, T^{-1}}]$ is the rate constant for a heterogeneous reaction. Additional assumptions made in deriving above rate equation are

- The reaction process is kinetically controlled. The kinetics of the reaction is assumed to be linear. In the case of phosphate uptake on C-S-H particles it is a reasonable assumption as demonstrated in literature [103]. Second order kinetics might provide slightly better fit for phosphate uptake in C-S-H [103]. However, as this study does not focus on developing experimentally validated simulations, a first order assumption is justifiable.

- Only adsorption processes are considered on the surface of the particles, desorption is neglected as there is continuous supply of phosphate in case of P-RoC$^{\copyright}$ process at the inlet.

- The reaction, being a weak adsorption, does not change the geometry of the particle.

- The shape of the solid particle is spherical.

- The particles are mono disperse as a working assumption but is not the limitation of the model.

6.1.2 Discrete element method

DEM solves particle motion by integrating Newton's second law (Chapter 4). Interaction between particles is modeled using contact laws, which account for forces due to particle-particle contacts and friction between particles. While coupling with the fluid flow, additional forces need to be included, e.g. hydrostatic (buoyancy force) and hydrodynamic forces (drag force), etc. Following Mordant and Pinton [70], the acting force $\vec{F}_l : I \to \mathbb{R}^3 \, [\mathrm{M \, L \, T^{-2}}]$ on a solid spherical particle in initial resting water exposed to the earth's gravity field is the sum of the drag force $\vec{F}_{\mathrm{d},l}$ in (4.3) with $c_{\mathrm{d},l}$ as given in (4.8), the weight and buoyancy force $\vec{F}_{\mathrm{g},l}$ and $\vec{F}_{\mathrm{b},l}$ (4.9), the added mass force $\vec{F}_{\mathrm{am},l}$ (4.11), the contact force $\vec{F}_{\mathrm{c},l}$ and the history

force. In (4.3) and (4.11), the fluid velocity $\vec{u}$ is replaced by the intrinsic volume-averaged velocity $\langle\vec{u}\rangle$. The history force is neglected here as Mordant and Pinton show that especially for the terminal stationary settling velocities the influence of the history force is little. For each of the $n \in \mathbb{N}$ particles, that are assumed to be spherical and of the same size, Newton's equation of motion for the force $\vec{F}_l$ in (4.1),

$$m_l \frac{\mathrm{d}\,\vec{u}_l(t)}{\mathrm{d}\,t} = \vec{F}_l = \vec{F}_{\mathrm{d},l}(t) + \vec{F}_{\mathrm{g},l}(t) + \vec{F}_{\mathrm{b},l}(t) + \vec{F}_{\mathrm{am},l}(t) + \vec{F}_{\mathrm{c},l}(t)\,, \qquad (6.2)$$

and for the torque $\vec{T}_l : I \to \mathbb{R}^3$ in (4.2) ,

$$\vec{T}_l(t) = \vec{T}_{\mathrm{c},l}(t)\,, \qquad (6.3)$$

is solved to obtain the trajectories and the rotational dynamics for the particles. $\vec{T}_{\mathrm{c},l} \in \mathbb{R}^3$ results from the contact forces given in (4.17).

For the formulation of the Reynolds number in (4.8), the expression

$$\mathrm{Re}_l = \frac{2\,r_l\,\vec{u}_{\mathrm{exp.},l}}{0.89 \times 10^{-6}\,\mathrm{m}^2\,\mathrm{s}^{-1}}$$

is used as given in Habte and Wu [68]. $\vec{u}_{\mathrm{exp.},l} \in \mathbb{R}^3$ [M T^{-1}] is the particular sedimentation velocity of particle l obtained from experimental studies [70].

Since in this study periodic boundaries are utilized, interactions between particles and walls are neglected.

6.2 Numerical approach and implementation aspects

In the present study, the VANSE and VAADRE are solved using the LBM coupled to the DEM. The lattice Boltzmann schemes for these equations are discussed further in Section 3.2 and Section 3.3. The simulations are realized in the LBM framework *Yantra* that is coupled with the DEM open-source framework *Yade*. The latter utilizes the Verlet scheme to integrate (6.2) which is second-order accurate. For detailed description of implementation aspects e.g. contact detection, contact force computation, etc., the readers are referred to the *Yade* manual [77]. The coupling between the solvers is done in staggered manner with global time step equal to the minimal time step of the DEM or LBM computation. After the initialization, the DEM computation is performed, followed by the VANSE computation. Finally, the VAADRE computation is run if needed. The overall scheme for the coupling

between different components is presented in Figure 6.1. The overall coupling algorithm is as shown in Algorithm 1 in Appendix A.

For the flow simulation for the first and third simulation, a three-dimensional (3D) D3Q19 stencil ($q_f = 19$) and for the second one, a two-dimensional (2D) D2Q9 stencil ($q_f = 9$) is used. The corresponding values for $\vec{c}_i$, w_i and c_s are given in Table 2.4 and Table 2.2. For the reactive mass transport for the first and third simulation, a D3Q7 stencil ($q_g = 7$) and for the second simulation, a D2Q5 stencil ($q_g = 5$) is used. The corresponding properties of the stencils are given in Table 2.3 and Table 2.1.

6.3 Results and discussion

In this section, the validation of the model and the results from numerical experiments are presented. Firstly, the settling of a single sub-grid particle in a cavity filled with water is compared to the experimental results of the literature (Section 6.3.1). Grid convergence studies are performed for both the fluid and the particle velocity. It is also demonstrated that the proposed model is convergent on grid refinement for both the fluid and the particle velocity. This has not been demonstrated for any models proposed in literature before. Secondly, the approach is used to compute the change in the reactive substance concentration because of reactions to sub-grid particles with fixed position in a channel (Section 6.3.2). It is validated by comparing the results with a simulation of fully resolved pore-scale particles of the same specific surface area [104]. Finally, the simulation is conducted for a suspension of 1,000, 2,000, respective 3,000 particles, water and reactive substance in a segment of a channel (Section 6.3.3). The change in the concentration of the reactive substance at the outlet due to reaction processes is compared with the one-way coupled simulation.

6.3.1 Two-way coupled single particle sedimentation

Two-way coupling of VANSE and DEM was validated against the experiments of Mordant and Pinton [70]. They investigated the settling of a single particle in resting water ($\rho = 1,000 \, \text{kg m}^{-3}$, $\mu = 0.89 \times 10^{-4} \, \text{kg m}^{-1} \text{s}^{-1}$) by experimental studies. The size of the simulation domain is chosen to be (0.5, 1.0, 0.5) m for the (x, y, z)-direction, Figure 6.2. Table 6.1 gives an overview of the radius r_l and the density ρ_l of three exemplary particles of small, medium and large size. It also provides the corresponding drag coefficients $c_{\text{d},l}$. Drag coefficients are computed using (4.8) and $u_{\text{exp.},l}$, (given in Table 6.2). The initial particle position is $\vec{x}_l = (0.25, 0.75, 0.25)$ m, the initial particle and fluid velocity is set to zero in all directions.
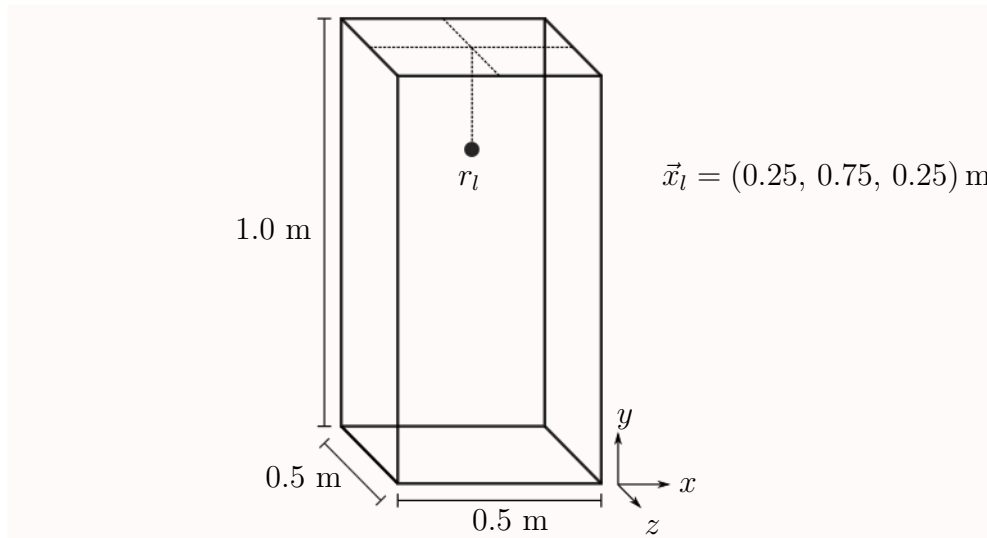
Figure 6.2: Physical setup of the single particle settling experiment.

The gravitational acceleration is taken as $\vec{g} = (0, 9.80665, 0)\,\mathrm{m\,s^{-2}}$. The duration of the simulation is $t = 1\,\mathrm{s}$. For DEM all boundaries are set as periodic. For fluid flow the boundaries in x- and z-direction are periodic and in y-direction a zero flux boundary is applied through half-way bounce-back [36, 105]. The dimensionless relaxation time is $\tau = 0.50006$ which is kept constant while performing the grid convergence study. Doing so, both Δx and Δt are refined successively by diffusive scaling [19].

particle	r_l / 10^{-4} m	ρ_l / kg m^{-3}	$c_{\mathrm{d},l}$ / -
small	2.5	2,560	1.697
medium	7.5	2,560	0.632
large	10.0	2,480	0.523

Table 6.1: Overview over the properties of the particles that were also investigated by Mordant and Pinton [70].

For the grid convergence study the relative error in particle velocity is given by

$$err_p(h) := \sqrt{\frac{\sum_{t \in I_h} \left(u_{l,2,200}(t) - u_{l,2,h}(t) \right)^2}{\sum_{t \in I_h} \left(u_{l,2,200}(t) \right)^2}}, \qquad (6.4)$$

respective in fluid velocity by

$$err_f(h) := \sqrt{\frac{\sum_{\vec{x} \in \Omega_h} \left(\langle u_{2,200} \rangle (t, \vec{x}) - \langle u_{2,h} \rangle (t, \vec{x}) \right)^2}{\sum_{\vec{x} \in \Omega_h} \left(\langle u_{2,200} \rangle (t, \vec{x}) \right)^2}} \, , \tag{6.5}$$

with $h < 200$, $\vec{u}_{l,h} = (u_{l,1,h}, u_{l,2,h}, u_{l,3,h})$ and $\langle \vec{u}_h \rangle = (\langle u_{1,h} \rangle, \langle u_{2,h} \rangle, \langle u_{3,h} \rangle)$. For $err_p(h)$, the particle velocities $u_{l,2,200}$ are interpolated to the points in time, $t \in I_h$, of the less resolved simulation of resolution h. For $err_f(h)$, the fluid velocities are interpolated to the lattice positions $\vec{x} \in \Omega_h$ of the less resolved simulation. In case of the particle velocity, the EOC is determined by the slope of the error fit line of $err_p(h)$ over Δt. The EOC of the fluid velocity is the slope of the error fit line of $err_f(h)$ over Δx. $\Delta x = 0.5 \, \text{m}/h$ changes for $h \in \{120, 140, 160, 180, 200\}$ with corresponding $\Delta t \in \{1.56, 1.15, 0.878, 0.694, 0.562\} \times 10^{-3}$ s.

particle	$u_{\text{exp.},l}$ / m s^{-1} [70]	$\text{Re}_{\text{exp.},l}$ / - [70]	$u_{l,2,h=200}$ / m s^{-1}	$\frac{u_{l,2,h=200} - u_{\text{exp.},l}}{u_{\text{exp.},l}}$ / -
small	-0.074	41	-0.078	0.0541
medium	-0.218	360	-0.221	0.0138
large	-0.271	600	-0.274	0.0111

Table 6.2: Comparison of the simulated terminal settling velocity $u_{l,2}$ with the measured data $u_{\text{exp.},l}$ of [70] and the resulting relative error.

The terminal particle velocity $u_{l,2}$ of the three particle sizes small, medium and large ($h = 200$: $\Delta t = 5.62 \times 10^{-4}$ s, $\Delta x = 2.5 \times 10^{-3}$ m) and the measured results of Mordant and Pinton [70] show good agreement (refer to Table 6.2). The larger the particle, the higher its negative velocity and the smaller the relative error. The latter decreases from about 5 % for the small particle to about 1 % for the medium and the large particle. Smaller particles reach their terminal velocity in a short time compared to larger particles. A higher temporal resolution might decrease the error. The error reported in this study is higher than that for the similar size particles carried out previously by other researchers. Maier et al. [91] reported the relative error to $u_{\text{exp.},l}$ is about 1.8 %. Habte and Wu [68] enlarged the particle to $r_l = 2.62 \times 10^{-4}$ m but compared it to $u_{\text{exp.},l}$ of the small particle and got an error of about 3.8 %. One reason for the different results are that both studies used slightly larger $c_{\text{d},l} = 1.83$ than the one used here ($c_{\text{d},l} = 1.697$). As $c_{\text{d},l}$ is related to $u_{\text{exp.},l}$ by (4.8), this has direct impact on the results. It is remarkable that the relative error of a simulation with $c_{\text{d},l} = 1.83$ is only 1.4 % as the terminal velocity is about $-0.075 \, \text{m s}^{-1}$. Rettinger et al. [106] run a similar simulation for a spherical particle of radius $r = 1.75 \times 10^{-4}$ m

with density $\rho = 2,500\,\mathrm{kg\,m^{-3}}$. Their results agree very well with the experimental results of [107]. Nevertheless, nobody checked different particle sizes. Additionally, there exists no work where the EOC is computed neither for the particle nor for the fluid velocity.
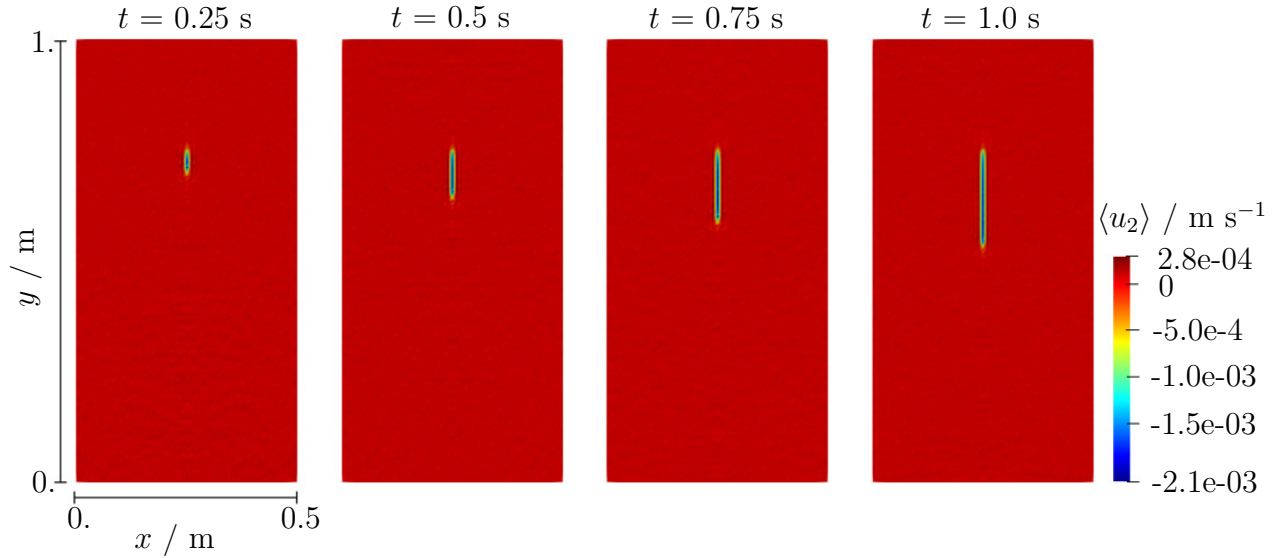

Figure 6.3: The averaged velocity $\langle u_2 \rangle$ of the fluid in y-direction is accelerated by the settling of the medium sized particle. Four different times are depicted in the centered x-y-plane ($\Delta t = 5.62 \times 10^{-4}$ s, $h = 200$).
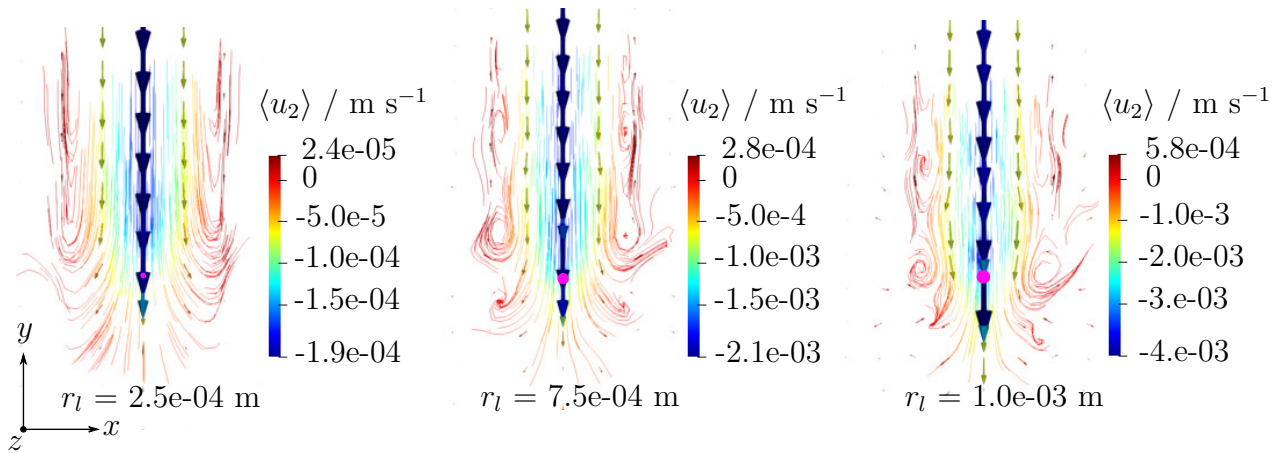
Figure 6.4: Depending on the size of the violet colored particle small vortexes in the fluid arise next to it (left: $r_l = 2.5 \times 10^{-4}$ m, middle: $r_l = 7.5 \times 10^{-4}$ m, right: $r_l = 1.0 \times 10^{-3}$ m, $\Delta t = 5.62 \times 10^{-4}$ s, $h = 200$). The vectors located at every Euler grid point depict the direction and are scaled by a multiple of the magnitude of the fluid velocity.

The effect of the two-way coupling is depicted both in the whole domain and in the direct surrounding of the particle. The settling particle induces the force density $\vec{f}_\mathrm{d}$ on the fluid that is accelerated in the area touched by the particle. This is clearly visible in the velocity field

plot of the fluid for the medium particle at four different times in the centered x-y-plane for the finest grid resolution ($\Delta t = 5.62 \times 10^{-4}$ s, $h = 200$), Figure 6.3. In case of the medium sized particle, the trail of accelerated fluid directly behind the particle has a maximum negative velocity of $\langle u_2 \rangle = -2.1 \times 10^{-3}$ m s^{-1}. Besides the downward directed speed, the positive fluid velocity $\langle u_2 \rangle \approx 2.8 \times 10^{-4}$ m s^{-1} occurs next to the particle, Figure 6.4. For the medium and the large particle, small vortexes arise next to the particle, Figure 6.4 (middle, right). For the small particle, the transition to the back-flow is more laminar, Figure 6.4 (left). This behavior depends on Re$_l$, Table 6.2. The streamlines are computed by *ParaView* version 5.5.0 by use of the filter *stream tracer* with integrator type *forward Runge-Kutta 4*.

A convergence study on both the particle and the fluid velocity is performed. For the medium particle, the curves of the settling velocity over time appear to be similar for all Δt, Figure 6.5. A detailed look into the transition area of acceleration state to steady state ($t = 0.09$ s to $t = 0.14$ s) shows that the magnitude of $u_{l,2}$ decreases for decreasing Δt. However, for decreasing Δt the curves approach each other. The small and the large sized particle show a similar behavior.
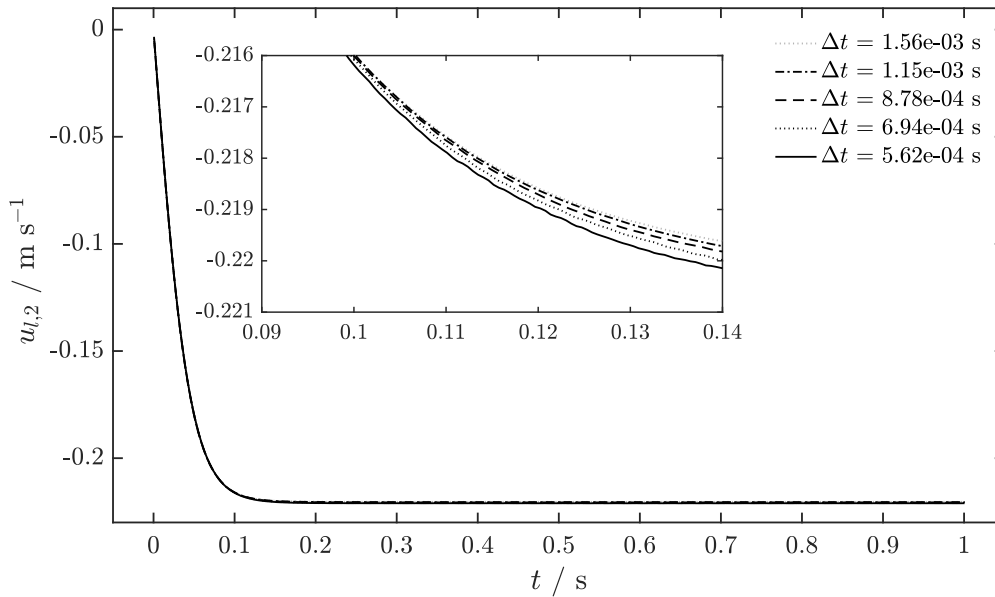

Figure 6.5: For the medium sized particle, the settling velocity over time differs little for simulations of different Δt. A convergence of the velocity towards the results of the simulation with the finest Δt is obvious by a more detailed look.

To determine whether the simulation converges, the relative error in particle velocity, $err_p(h)$ in (6.4), is computed for the grid resolutions $h \in \{120, 140, 160, 180\}$. Figure 6.6 (a) shows the plot of error versus the time increment in a double logarithmic scaling. $err_p(h)$ is smaller than 0.3 %. The slope of the errors is about 1.5 and equals the particle EOC.

Theoretically, the leapfrog scheme is second order convergent. Deviation from theoretical order of convergence might stem from the forces, especially the drag force, that are time dependent and computed based on interpolation.
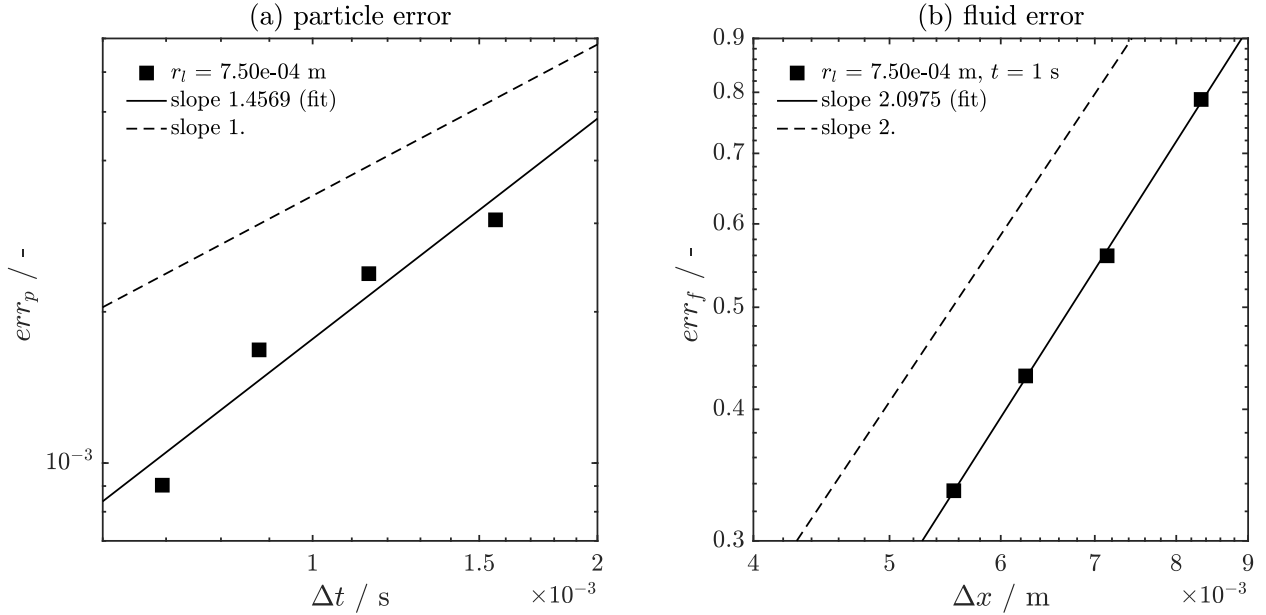

Figure 6.6: (a) The relative error $err_p(h)$ is plotted over the time increment. It is smaller than 0.3 %. The slope of the fit to err_p, the particle EOC, is ~ 1.5. (b) The simulation converges for decreasing Δx. The slope of the fit to err_f, the fluid EOC, is ~ 2.
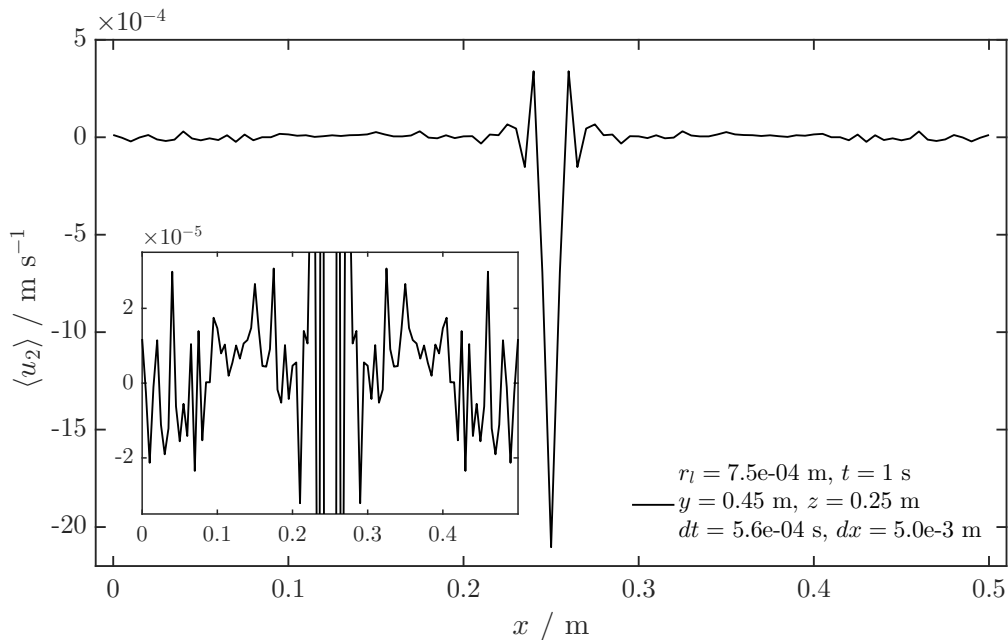
Figure 6.7: The fast increase of the particle settling velocity generates kind of a momentum perturbation. This results in a noise throughout the whole domain with values of about 2.5×10^{-5} m s^{-1} for $h = 200$ for the medium sized particle at $t = 1$ s.

For the fluid velocity grid convergence study, only grid points with velocities of larger magnitude are involved. The fast increase of the particle settling velocity creates a fast increase of the drag force acting on the fluid. That generates kind of a momentum perturbation and results in a noise on the whole grid with values of a magnitude of about 2.5×10^{-5} m s^{-1} ($h = 200$). To depict this, $\langle u_{2,200} \rangle (t = 1 \text{ s})$ is plotted along a horizontal line in the center of the simulation domain, $(y, z) = (0.45, 0.25)$ m, Figure 6.7. As the noise does not directly depend on h, it is not considered for the error computation. The grid convergence of the fluid velocity is given by $err_f(h)$, $h \in \{120, 140, 160, 180\}$, Figure 6.6 (b). In the double logarithmic plot, the fit to the errors has a slope of ~ 2. The relative errors are large, however, the simulation converges. More refined simulations ($h > 200$) might be helpful to further decrease the errors while keeping Δx larger than r_l for the sub-grid particle method ($h = 200$: $\frac{\Delta x}{r_l} = 10$ for the largest particle size).

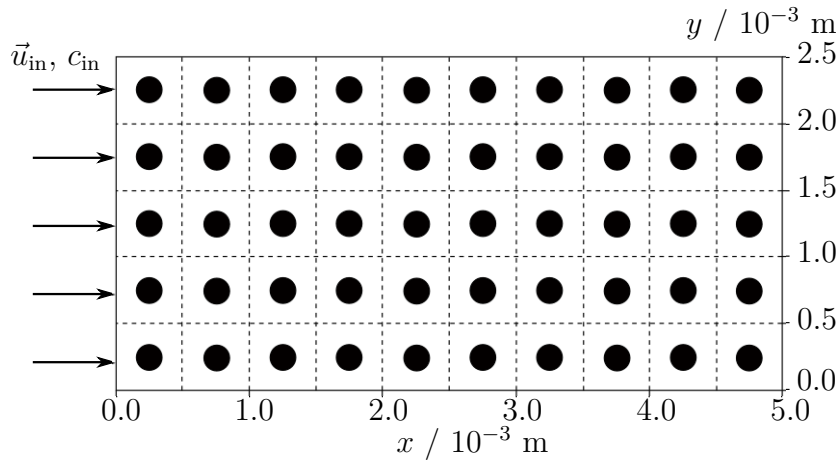## 6.3.2 Validation case for volume-averaged reactive particle fluid flows

Figure 6.8: The validation test case consists of a rectangular domain in 2D and contains 50 spherical particles where the reaction takes place. The dashed lines depict the computational grid for the coarsest resolution ($\Delta x = 5 \times 10^{-4}$ m).

To validate the application of the VANSE-VAADRE coupling for reactive sub-grid particles, a 2D test case of 50 fixed and evenly arranged particles with $r_l = 10^{-4}$ m is chosen. The simulation from the VANSE-VAADRE coupled model, also referred to as unresolved simulation due to the homogenized volume representation of the particle, are compared with a fully resolved pore-scale simulations with heterogeneous reactions. For the fully resolved simulation the pore-scale modeling approach with explicit geometrical description of the particle
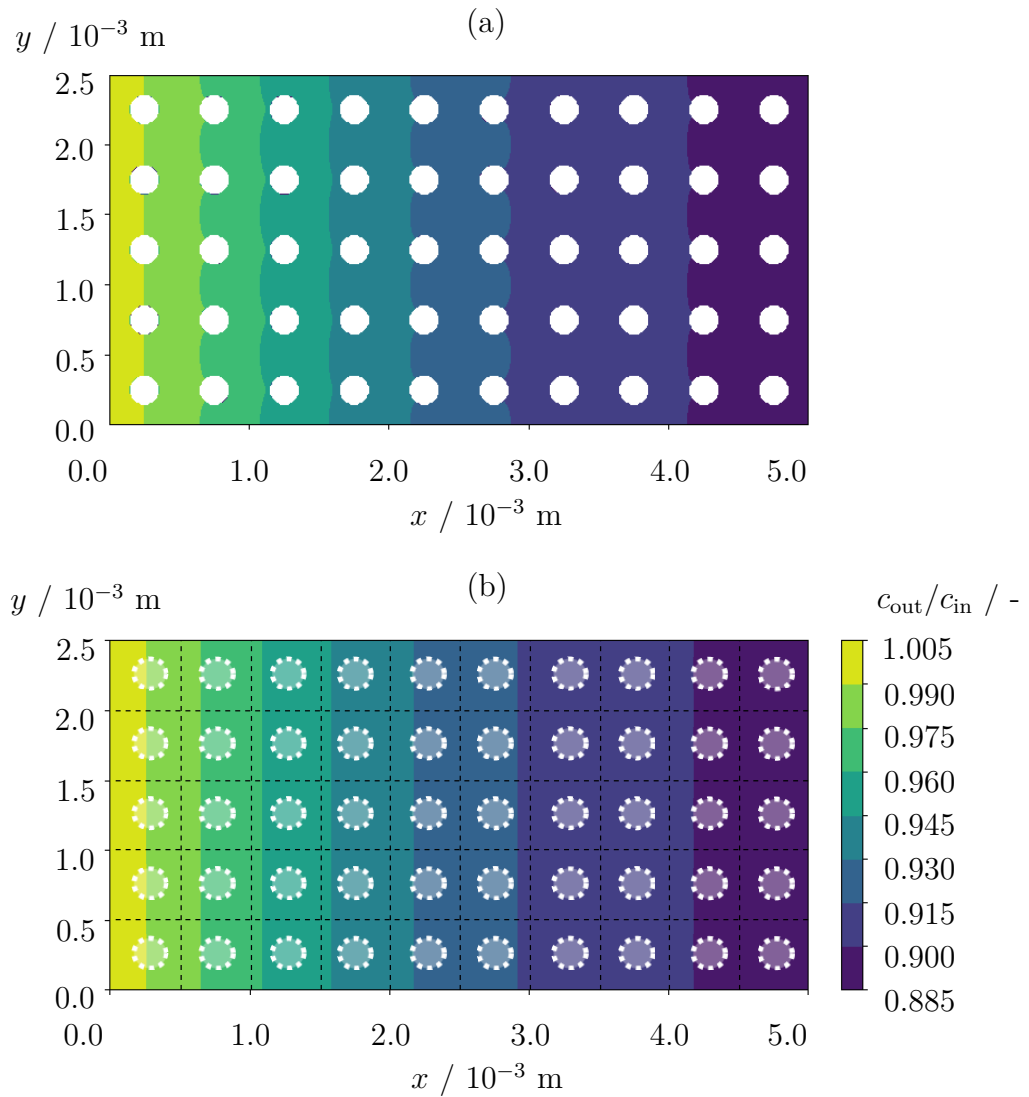
Figure 6.9: Comparison of the resolved (a) and the unresolved (b) particle simulations for about 2×10^{-4} s ($\Delta x = 5 \times 10^{-4}$ m) in a filled contour plot. In (b), the position of the particles is indicated by a white dotted line, the underlying grid is given by the black dotted lines.

formulated by Patel et al. [13, 104] is used. There, the heterogeneous reaction is modeled as a pseudo-homogeneous reaction and takes place in the fluid node adjacent to the solid node by a source term. The size of the domain is $(5.0, 2.5) \times 10^{-3}$ m for the (x, y)-direction, Figure 6.8. The global porosity is $\phi = 0.8743$. Only the drag force is considered. The duration of the simulation is about 2×10^{-4} s. For the test case, the properties of the fluid are set to be $\rho = 1\,\text{kg\,m}^{-3}$ and $\mu = 166\,\text{kg\,m}^{-1}\,\text{s}^{-1}$ with an initial velocity of $u_{\text{in},2} = 10^{-3}\,\text{m\,s}^{-1}$. The initial concentration of the reactive substance is $c_{\text{in}} = 1\,\text{mol\,m}^{-3}$, with $D = 0.1667\,\text{m}^2\,\text{s}^{-1}$ and $k = 5 \times 10^{-1}\,\text{m\,s}^{-1}$. The boundary in y-direction is periodic for the VANSE. For VANSE, periodic fixed velocity ($u_{\text{in},2} = 10^{-3}\,\text{m\,s}^{-1}$) at the inlet and fixed pressure at the
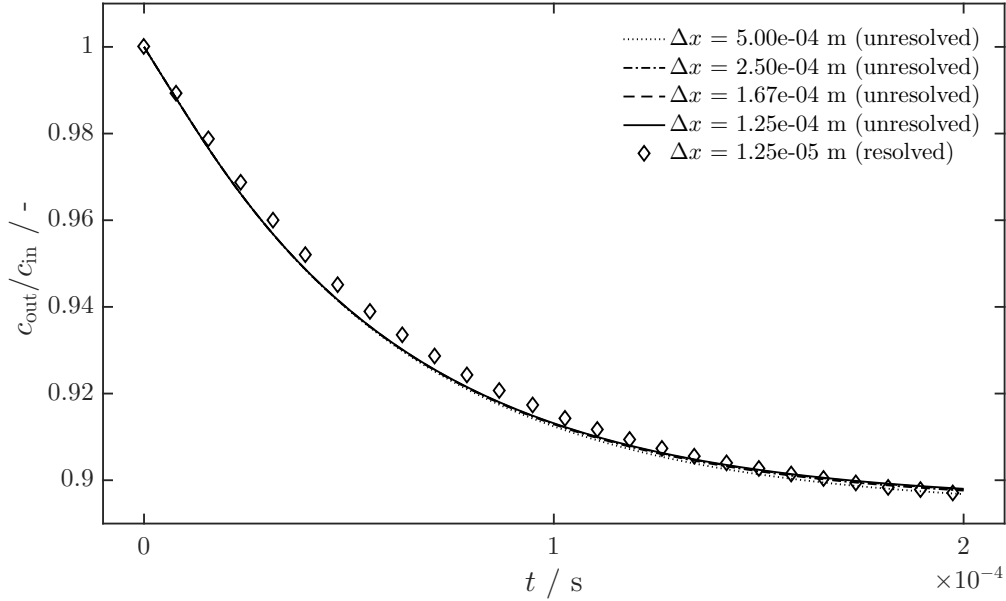
Figure 6.10: Comparison of the resolved and the unresolved particle simulations for about 2×10^{-4} s.

outlet is applied in x-direction. For VAADRE, fixed concentration ($c_{in} = 1 \, \mathrm{mol \, m^{-3}}$) at inlet and open boundary at outlet is applied. Open boundary condition for the concentration is set by copying the unknown distribution function from the next neighbor grid cell. The dimensionless relaxation time is $\tau^- = 0.6$.

The final concentration distribution in the domain at 2×10^{-4} s is similar for both the unresolved and the resolved simulation, Figure 6.9. At the inlet, $c_{out}/c_{in} = 1$ and decreases to $c_{out}/c_{in} = 0.885$ to 0.9 at the outlet. The mean concentration at the outlet normalized by the mean concentration at the inlet, c_{out}/c_{in}, plotted over the time decreases in an exponential manner by a tenth and reaches a steady state after about 2×10^{-4} s, Figure 6.10. Additionally, simulations are conducted for four different resolutions ($\Delta x = 5.0 \times 10^{-4}$ m, 2.5×10^{-4} m, 1.67×10^{-4} m, 1.25×10^{-4} m) for sub-grid particles which are in good agreement with each other. The results of the resolved simulation ($\Delta x = 1.25 \times 10^{-5}$ m) are similar but slightly larger than the unresolved values during the decrease. In transition to the steady state they are again in good agreement.
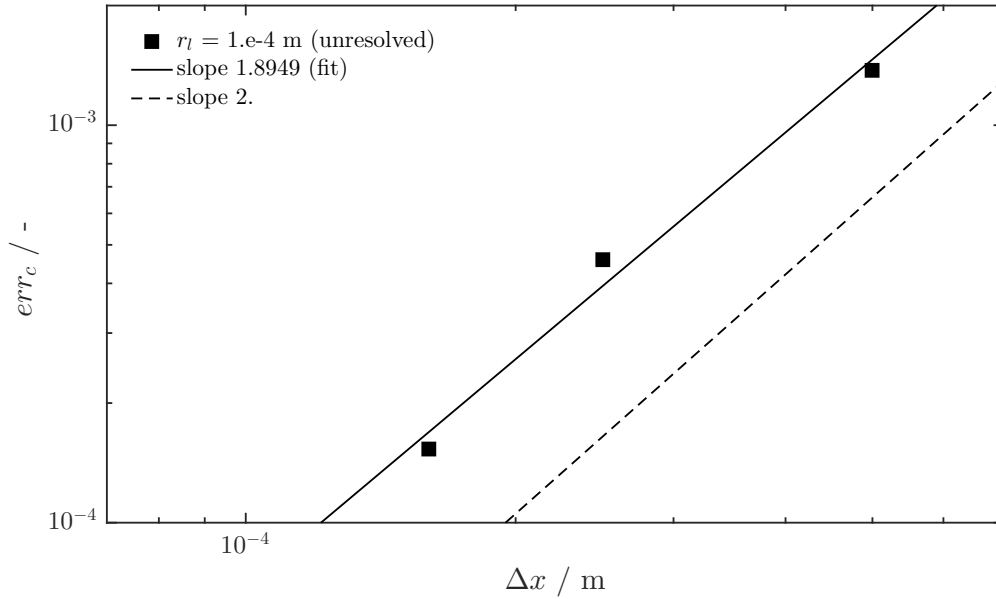
Figure 6.11: The relative error err_c of the concentration at the outlet at time $t = 2 \times 10^{-4}\,\mathrm{s}$ is smaller than $\sim 0.1\%$. The slope of the fit to err_c is about 2.

To determine whether the simulation converges, the relative error in concentration, err_c, is computed for the grid resolutions $h \in \{5, 10, 15\}$ and compared to resolution $h = 20$. It is computed as follows

$$
err_c(h) := \sqrt{\frac{\sum_{\vec{x} \in \Omega_h|_{\mathrm{outlet}}} \left(c_{20}(t, \vec{x}) - c_h(t, \vec{x}) \right)^2}{\sum_{\vec{x} \in \Omega_h|_{\mathrm{outlet}}} \left(c_{20}(t, \vec{x}) \right)^2}},
\tag{6.6}
$$

with $h \in \{5, 10, 15\}$. The EOC of the concentration is the slope of the error fit line of $err_c(h)$ over Δx. Figure 6.11 shows the plot of error versus Δx in a double logarithmic scaling. err_c is smaller than 0.1 %. The slope of the errors, also referred to as EOC, is about two.

6.3.3 Fully coupled model with multiple reactive particles

The applicability of the fully coupled VANSE-VAADRE-DEM model is shown for a setup of 1,000, 2,000 and 3,000 spherical solid particles that flow in a segment of a channel of size $(5, 5, 5) \times 10^{-3}\,\mathrm{m}$ for the (x, y, z)-direction, Figure 6.12. The particle phase is mono-disperse with radius $r_l = 10^{-4}\,\mathrm{m}$ and density $\rho_l = 2{,}550\,\mathrm{kg\,m^{-3}}$. In this setup, drag force $\vec{F}_{\mathrm{d},l}$ is considered to act on the particles with $c_{\mathrm{d},l} = 1.8$. Besides, the contact forces of particle-particle collisions are included with a Young's modulus of $10^2\,\mathrm{kg\,m^{-1}\,s^{-2}}$ and Poisson's ratio of 0.3. They are chosen to enable a DEM-time step size of $10^{-3}\,\mathrm{s}$ and soft collisions. The

properties of water are $\rho = 1,000\,\mathrm{kg\,m^{-3}}$ and $\mu = 10^{-4}\,\mathrm{kg\,m^{-1}\,s^{-1}}$. The initial concentration of the reactive substance is $c_{\mathrm{in}} = 2.6 \times 10^{-1}\,\mathrm{mol\,m^{-3}}$, with $D = 10^{-9}\,\mathrm{m^2\,s^{-1}}$ and $k = 5 \times 10^{-4}\,\mathrm{m\,s^{-1}}$. For the fluid flow, an initial velocity $\vec{u}_{\mathrm{in}} = (0,\,8 \times 10^{-3},\,0)\,\mathrm{m\,s^{-1}}$ is generated by an external body force $\vec{f}_{\mathrm{body}} = \frac{0.2}{\Delta x^3}\,\mathrm{kg\,m\,s^{-2}}$ to mimic a pressure gradient [108]. The simulation domain consists of periodic boundaries in x-z-direction for the fluid flow, the concentration and the particle simulation. For the particles and the fluid flow, the boundaries in y-direction are periodic, too. The duration of the simulation is $t = 2.5\,\mathrm{s}$.
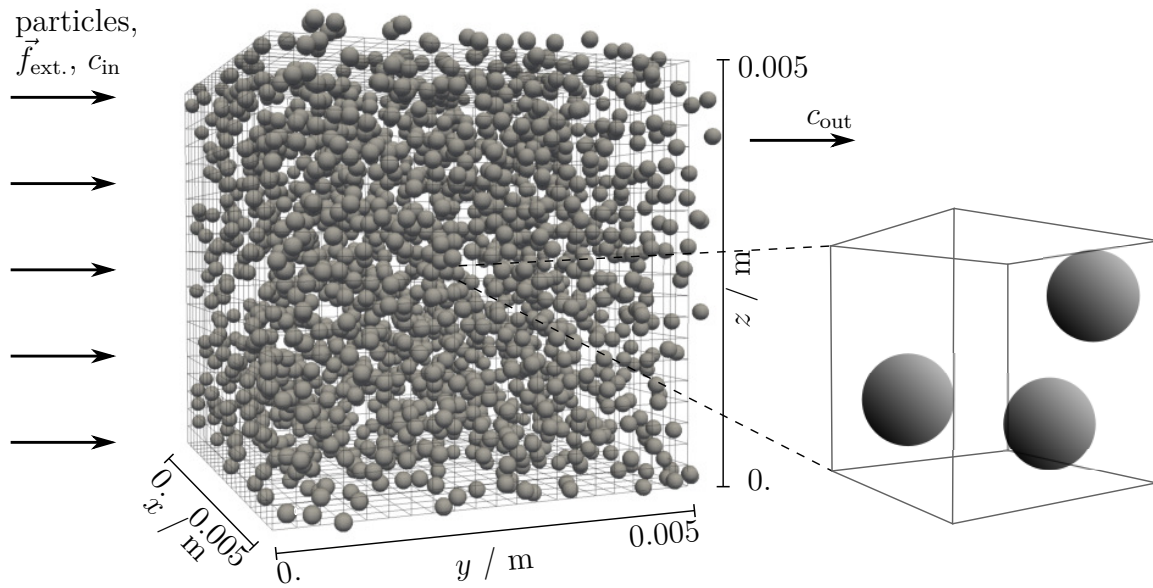

Figure 6.12: Discretization of the simulation domain and depiction of 2,000 particles. Some particles protrude from the box because of the periodicity of the boundaries in x-, y- and z-direction for fluid and particles (left). In case of the concentration the boundaries are periodic in y- and z-direction. Crop of one Euler grid cell that contains three Lagrange particles (right).

First, the pure fluid velocity is computed until a steady state is reached ($\tau = 0.7$, $\Delta x = 2.5 \times 10^{-4}\,\mathrm{m}$, $\Delta t = 4.16 \times 10^{-3}\,\mathrm{s}$). In a second step, the particles are randomly distributed over the domain and are initialized with fluid velocity. Finally, the concentration is injected in the x-z-plane ($y = 0\,\mathrm{m}$) ($\tau^- = 0.50016$, $\Delta x = 2.5 \times 10^{-4}\,\mathrm{m}$, $\Delta t = 1.8 \times 10^{-3}\,\mathrm{s}$). The velocity and the concentration transport computation is resumed and carried on together with the particle simulation.

In Figure 6.13, the concentration (top) and the magnitude of the associated velocity (bottom) of the 2,000 particles simulation is depicted in a three dimensional manner at $t = 2.4\,\mathrm{s}$. Due to the high number of particles, more particle-particle contacts occur that cause locally higher flow velocities. The two-way coupled simulation is compared to an one-way coupled system that does not consider the displacement of fluid by particles. This means
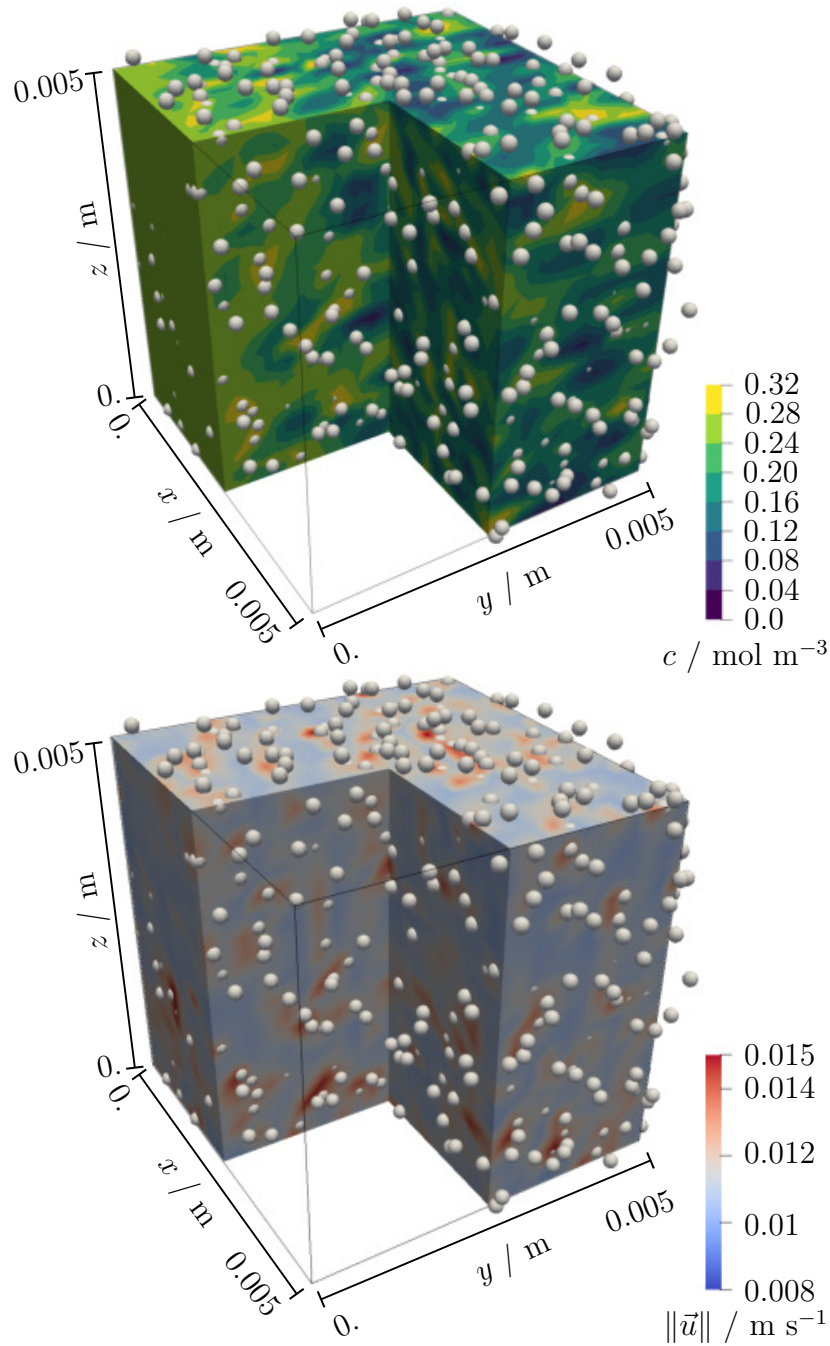
Figure 6.13: Three dimensional depiction of the concentration c after $t = 2.4\,\text{s}$ for 2,000 particles (top) and magnitude of the associated velocity $\|\vec{u}\|$ (bottom).

the particles do neither affect the fluid by a drag force nor change the diffusivity by changing porosity, i.e. $\vec{f}_d = 0$ and $\phi = 1$. The two- and one-way coupled simulations are compared for 3,000 ($\phi = 0.899$), 2,000 ($\phi = 0.933$) and 1,000 ($\phi = 0.967$) particles, Figure 6.14. In all cases, the temporal development of the mean concentration at the outlet of the domain, c_{out}, shows an increase after $0.5\,\text{s}$. The increase is caused by the concentration transport towards the outlet. In the following second, c_{out} fluctuates around $0.19\,\text{mol}\,\text{m}^{-3}$ (1,000

particles), $0.15\,\mathrm{mol\,m^{-3}}$ (2,000 particles) and $0.11\,\mathrm{mol\,m^{-3}}$ (3,000 particles). As expected, c_{out} is the smallest for the 3,000 particles and the largest for the 1,000 particles as the reactive surface increases with increasing particle number. In case of the one-way coupling, a slight fluctuation remains for the rest of the simulation duration in all experiments. The results of the two-way coupled 1,000 particles simulation are similar to the one-way coupled results. The porosity is high and thus the impact of the particles on the fluid flow small. Additionally, the probability of particle-particle contacts is little. The results of the two-way coupled 1,000 particles simulation are similar to the one-way coupled results. The porosity is high and thus the impact of the particles due to two way coupling is small. In case of the two-way coupled 2,000 and 3,000 particles simulations, the fluctuations even out and c_{out} becomes larger compared to the one-way coupling results. After $1.5\,\mathrm{s}$ to $2\,\mathrm{s}$, c_{out} raises. Since the transport of chemical species to region with more particles slows down due to the two-way coupling, less reactions take place and thus c_{out} increases as observed in Figure 6.14 for two-way coupling case. The effect of the two-way coupled simulation is small for high porosity and increases for lower ones which is a logical outcome and qualitatively demonstrates that two way coupling is working properly.
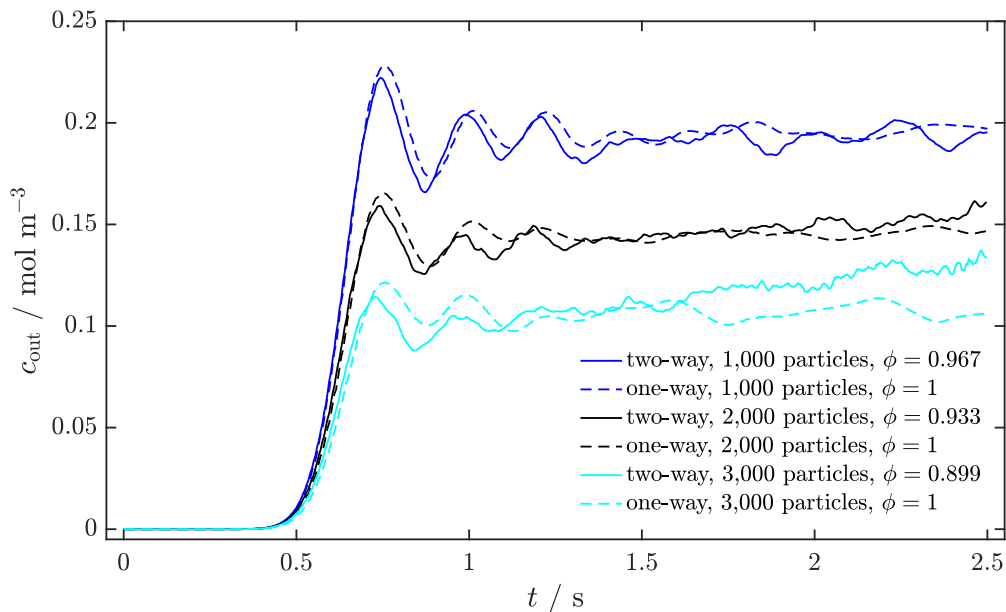

Figure 6.14: Temporal progress of the mean concentration c_{out} at the outlet of the channel segment. For both the one- and the two-way coupling, the concentration decreases because of the reaction that takes place at the surface of the 1,000, 2,000 and 3,000 particles.

6.4 Conclusion

This work presents a novel fully two-way coupled multi-scale lattice Boltzmann and the discrete element method of in fluid suspended multi-particles combined to reaction simulations. It recovers fluid flow and reactive transport processes around disperse and moving particles in kind of a continuum framework through a volume-averaging procedure. The main feature is the proper coupling that has been validated by experimental data from literature, comparative simulations by thoroughly tested approaches and of course grid studies. The fluid was modeled by the volume-averaged Navier-Stokes equations, the reactive mass transport by the volume-averaged advection-diffusion-reaction equation to account for the displacement of the fluid and the reactive mass by the particles. The discrete element method was used for the suspended, solid, sub-grid particles. Fluid and particles were two-way coupled by the drag force.

The simulation of our approach show good accordance to experimental results from the literature in case of a single sub-grid particle that sinks in a cavity filled with water. Performed grid studies for both the fluid and the particle velocities prove the convergence of the simulations. The simulation results of the reactive substance transport and adsorption taking place at the surface of sub-grid particles with fixed position in a channel correspond very well to the results of a fully resolved pore-scale simulation. This demonstrates the correctness of the fully coupled volume-averaging process. The multi-scale approach applied to a suspension of thousands of particles demonstrates the benefit of the presented model to be an efficient simulation tool for larger particle fluid and reactive flow systems for industrial or engineering applications. The comparison of two-way and one-way coupling demonstrate the need for a two-way coupled model to handle dense particle fluid systems. The encouraging results obtained in this study would pave the way to apply the model to reactive particulate systems such as the P-RoC process by numerical simulations and further validate the model with experimental studies such as the one presented in [11]. As the data is not complete (e.g. exact kinetics are not known yet) the validation is part of future work.

7 Magnetic particle separation

To study a real case scenario in a complete device by simulation, the magnetic particle separation is chosen. It is studied for two different volume flows, two different particle fractions and two different saturation magnetizations by one-way coupled particle fluid flow simulations.

Devices for the separation of particles from fluids, e.g. magnetic separators or other filtering systems are used in the recycling industry, the chemical industry or in process engineering. Magnetic separators have a wide range of uses although their applicability is limited to magnetizable material systems. For example, they can be used to remove metal abrasion from gear oil [109] or, in a more specialized application, to separate specific proteins in biotechnological processes where surface-functionalized magnetic carriers are employed [16]. The motivation of the study conducted in this chapter is to acquire information about the influence of different process parameters on the quality of the particle separation in a spiral magnetic separator developed by Weschke et al. [110] at Dürr Systems GmbH, as depicted in Figure 7.1. This type of magnetic separator removes the separated particles continuously from the device using a rotating magnetic field.
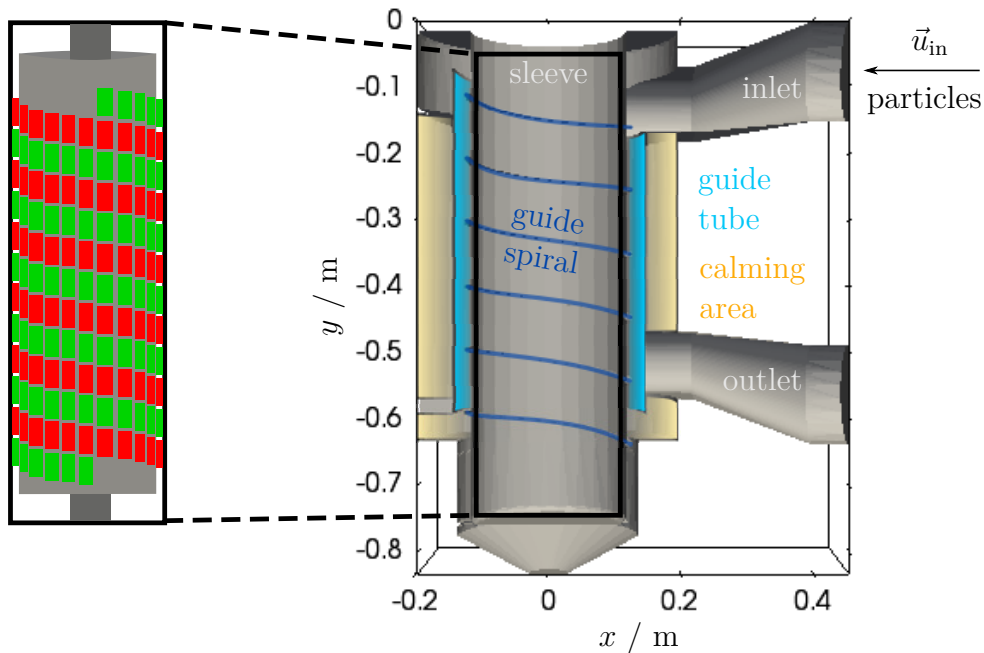

Figure 7.1: Clipped depiction of the simulation domain of the spiral magnetic separator given in stl-format (right). The device is composed of an inlet, an outlet and a cylindrical fluid domain. The fluid enters the device by the inlet with velocity $\vec{u}_{\text{in}}$. The sleeve with the guide spiral is located in the center of the device. It is surrounded by a second cylinder, the guide tube, that partitions the fluid domain into the annular gap and the calming area. Permanent magnets are arranged in a double helical pattern on the iron drum that is located within the sleeve (left). The north and south poles are alternately positioned (red, respectively green).

First, a short overview about the history of magnetic separators is given. The first high-gradient magnetic separator was patented by Frantz in 1939 [111]. Different types of separators followed, mostly consisting of low capacity and an associated discontinuous or quasi-continuous mode of operation [112]. Magnetically enhanced centrifugation patented by Fuchs et al. [113] allows a discharge of the wire filter by centrifugation. A continuous separation of a feed suspension without switching off the magnetic field is realized on laboratory scale by high-gradient magnetic centrifugation [114]. The separation quality of a magnetic separator depends on different process parameters e.g. the flow velocity or the specific particle properties. Three dimensional numerical simulations are a valuable tool to understand the process of particle separation within the device. The target of this study is to comprehend the dependence of the particle separation quality on the particle properties and on the volume flow of the feed suspension by studying the deposition structures. The parameters investigated by numerical simulations of the complete device are particle size, volume flow and saturation magnetization. The simulations are based on discrete particle methods and on the lattice Boltzmann method and focus on the representation of the changes in the particle deposition.

The structure of this chapter is as follows. First, the principles of magnetism and FEM are presented. Then, the utilized model equations and simulation methods are introduced (Section 7.2). Afterwards, the results of the magnetic field (Section 7.3.1) and of the flow field simulations for two different parameter settings (Section 7.3.2) are given. Finally, the resulting particle depositions are examined and discussed (Section 7.3.3).

7.1 Magnetism

In the following, the basics of magnetostatics are introduced. More detailed information is available e.g. in [115–117]. As the Maxwell equations are solved by FEM, a short overview is given.

7.1.1 Physical principles

Maxwell's equations for magnetostatics are used as the magnetic field is generated by permanent magnets. The Gaussian law for magnetism states that the divergence of the magnetic flux density $\vec{B}$ $[\mathrm{M\,T^{-2}\,I^{-1}}]$ is zero:

$$\nabla \cdot \vec{B} = 0 \,, \tag{7.1}$$

as the field is free of sources and sinks. Following Ampère's law of the Maxwell's equations, the curl of the magnetic field $\vec{H}$ $[\mathrm{I\,L^{-1}}]$ is zero:

$$\nabla \times \vec{H} = \vec{J}_{\mathrm{ext.}} = 0 \,, \tag{7.2}$$

as the external current density $\vec{J}_{\mathrm{ext.}}$ $[\mathrm{I\,L^{-2}}]$ is zero. Thus $\vec{H}$, respective $\vec{B}$, can be described by a scalar potential Ψ, or respective a vector potential $\vec{A}$, as follows:

$$\vec{H} = -\nabla\Psi \,, \qquad \text{resp.} \qquad \vec{B} = \nabla \times \vec{A} \,. \tag{7.3}$$

The relation between $\vec{B}$ and $\vec{H}$ is given by the constitutive relation

$$\vec{B} = \mu_0 \, (\vec{H} + \vec{M}) = \mu_0 \, \mu_r \, \vec{H} \,, \tag{7.4}$$

with the vacuum permeability (magnetic field constant) μ_0 $[-]$ and the relative permeability μ_r $[-]$. The magnetization $\vec{M} = \chi \, \vec{H}$ $[\mathrm{I\,L^{-1}}]$ depends on the magnetic susceptibility $\chi = \mu_r - 1$ $[-]$. In case of saturation, $\chi = \frac{\partial \vec{M}}{\partial \vec{H}} = 0$. Depending on the material exposed to the magnetic field, the magnetic field inside the material is changed by the material specific relative permeability μ_r, respective by the magnetic susceptibility χ. In vacuum and approximately also in air, $\mu_r = 1$ and the magnetic field remains unchanged. In case of a spherical magnetic particle l with radius r_l $[\mathrm{L}]$, the magnetic dipole moment $\vec{\mu}_l$ $[\mathrm{L^2\,I}]$ of the particle is given by

$$\vec{\mu}_l = 4/3 \, \pi \, r_l^3 \, \vec{M}_l \tag{7.5}$$

with magnetization $\vec{M}_l = \chi_l \, \vec{H} = (\mu_l - 1) \, \vec{H}$ and μ_l being the relative permeability of said particle. In case of a saturated magnetization that often occurs in ferromagnetic materials, the magnetic dipole moment is

$$\vec{\mu}_{\mathrm{sat.},l} = 4/3 \, \pi \, r_l^3 \, \left\| \vec{M}_{\mathrm{sat.},l} \right\| \, \left\| \vec{M}_l \right\|^{-1} \, \vec{M}_l \,. \tag{7.6}$$

In case the magnetization $\vec{M}_l$ is aligned with the direction of the magnetic field $\vec{H}$, the force $\vec{F}_{\mathrm{mag.},l} : I \to \mathbb{R}^3$ of the external magnetic field on a particle is given by [118]

$$\vec{F}_{\mathrm{mag.},l} = 4/3 \, \pi \, r_l^3 \, \mu_0 \, \left(\vec{M}_l \cdot \nabla \right) \vec{H} \,. \tag{7.7}$$

Diamagnetic materials ($\chi < 0$, resp. $\mu_r < 1$) cause a local weakening of the external magnetic field, while para- ($\chi > 0$, resp. $\mu_r > 1$) and ferromagnetic ($\chi \gg 0$, resp. $\mu_r \gg 1$) materials strengthen the magnetic field locally. In diamagnetic materials, e.g. water, nitrogen, noble metals and organic substances, the magnetic behavior is small. Here, the magnetic moments that are caused by the electrons in the orbit around an atomic nucleus compensate each other. Diamagnetism occurs in all materials. In paramagnetic or ferromagnetic materials, it is superimposed by the stronger paramagnetic or ferromagnetic effects. Paramagnetic materials, e.g. alkali, alkaline earth, transition and rare earth metals as well as oxygen, amplify an external magnetic field by aligning the single magnetic moments parallel to the external magnetic field. Without an external magnetic field, the magnetic moments are distributed homogeneously by thermal motion. Ferromagnetic materials are e.g. iron, nickel, cobalt. Ferrimagnetic materials are e.g. magnetite (Fe_3O_4). Antiferromagnetic materials are metal oxides such as hematite, manganese oxide, iron oxide [117]. Ferro-, ferri- and antiferromagnetic materials consist of magnetic moments that interact among each other over larger areas within a material, that are called Weiss domains. Due to anisotropic lattice structures, certain spin directions are preferred within such areas. In ferromagnetism, the electron spins within a Weiss domain are aligned parallel. In antiferromagnetism, the electron spins within a Weiss domain are aligned antiparallel and compensate each other. In ferrimagnetism, there are unequal antiparallel magnetic moments that do not compensate. Ferromagnetic materials appear unmagnetized if they are not exposed to a magnetic field and the magnetic moments are statistically distributed. In case they are exposed to a magnetic field they get magnetized. Materials are called remanent if the magnetization remains even if the external magnetic field is removed. Superparamagnetism occurs in ferro- and ferrimagnetic materials with small particle diameter. They do not experience of a remanent magnetization and lose their magnetization immediately outside a magnetic field.

7.1.2   Finite element method for magnetic fields

FEM is an appropriate way to numerically solve the Maxwell equations. The partial differential equations of the boundary value problem are solved in an integral form by multiplying with a weight function [19]. The simulation domain is discretised into the so called finite elements with a finite number of nodes $\vec{x}_p$, $p \in \mathbf{N}$. The underlying mesh is generally unstructured. The integral is numerically solved by summing over the numerical integrals of

the single elements. A dependent function a is approximated by a discrete solution variable a_p and basis functions $\psi_p(\vec{x})$,

$$a(\vec{x}) \approx \sum_p a_p\,\psi_p(\vec{x})\,, \tag{7.8}$$

what models a finite element. The following conditions

$$a(\vec{x}_p) = a_p \qquad \text{and} \qquad \sum_p \psi_p(\vec{x}) = 1 \tag{7.9}$$

have to be fulfilled. The finite elements are collected in a large system of algebraic equations that is solved numerically.

In general, the solution obtained by the FEM applied to solve the Maxwell equations is either a scalar Ψ or a vector potential $\vec{A}$. Eventually, the magnetic field $\vec{H}$ is obtained by

$$-\nabla \cdot (\mu_0\,\mu_r\,\nabla\Psi) = \nabla \cdot (\mu_0\,\mu_r\,\vec{H}) \tag{7.10}$$

with (7.1), (7.3) and (7.4).

7.2   Model equations, numerical approach and implementation aspects

The magnetic field is described by the Maxwell equations (7.1) and (7.2). The fluid flow is governed by the force-free NSE (see Section 2.2.1, $\vec{f} = 0$). The particle dynamics are modeled by Newton's equations of motion (see Chapter 4). As the number of particles is large, several simplifications are made to reduce computational costs.

- Interactions of the magnetic dipoles, rotations and contact forces are neglected.

- Particles that are already separated are not longer considered in the ongoing simulation.

- The removal of the separated particles that are attached to the sleeve is not performed.

- The hydrodynamic forces are limited to simple models. As the particles are small, Stokes drag force is applied.

- The impact of the particles on the fluid flow is not taken into account.

- The fluid flow simulation freezes when the particle simulation starts.

Nevertheless, a qualitative study of the particle separation is possible.

The particles are formulated by the Lagrange approach. The magnetic particles' dynamics are described by the Newton's equations of motion for the force (4.1). In this chapter, the total force is given by the Stokes drag (4.7) and the magnetic force (7.7):

$$\vec{F_l}(t) = \vec{F}_{\text{drag},l}(t) + \vec{F}_{\text{mag.},l}(t) \in \mathbb{R}^3 \,. \tag{7.11}$$

The Maxwell equations are solved by the FEM as described in Section 7.1.2. For the numerical computation of the fluid velocity, the SRT-LBM (Section 2.3) with discrete BGK-collision operator (2.34) is utilized. As the flow is turbulent, the Smagorinsky-Lilly model (Section 2.3.6) is included. For the flow simulation, the D3Q19 stencil ($q_f = 19$) is used. The magnetic field is computed by *COMSOL Multiphysics® 5.3, magnetic fields - no currents* [15] and is incorporated into *OpenLB* for both the fluid and the particle simulations. The implementation is as shown in Algorithm 2 in Appendix B.

7.3   Results and discussion

In this study, the particle separation is conducted for two exemplary mono-disperse particle fractions, F1 and F2, each of them assigned to two density related saturation magnetizations, $15\,\text{A}\,\text{m}^2\,\text{kg}^{-1}$ and $90\,\text{A}\,\text{m}^2\,\text{kg}^{-1}$. The density related saturation magnetizations correspond to the saturation magnetizations $\|\vec{M}_{\text{sat.},l}\|_2 = 45,600\,\text{A}\,\text{m}^{-1}$ and $\|\vec{M}_{\text{sat.},l}\|_2 = 265,600\,\text{A}\,\text{m}^{-1}$. The particle properties of F1 and F2 are depicted in Table 7.1, they differ in radius and mass concentration.

fraction	r_l / m	ρ_l / $\text{kg}\,\text{m}^{-3}$	$\sum_l \frac{m_l}{\text{m}^3}$ / $\text{kg}\,\text{m}^{-3}$
F1	10^{-4}	2,950	$2. \times 10^{-2}$
F2	10^{-5}	2,950	$2. \times 10^{-4}$

Table 7.1: Properties of the two particle fractions.

The simulations are conducted in the spiral magnetic separator that is introduced in the beginning of this chapter. It consists of an inlet for the uncleaned and an outlet for the processed fluid, Figure 7.1. The height of the fluid domain is $0.8\,\text{m}$, the width about $0.6\,\text{m}$. A volume flow rate as low as $30\,\text{m}^3\,\text{h}^{-1}$ is achievable. Inside the housing, the fluid flows around a cylindrical sleeve. Within the sleeve, a rotating drum with helical positioned permanent magnets is located. They generate a magnetic field that pulls the magnetizable

particles of the suspension to the sleeve. To clean the sleeve from the particles, the drum rotates and causes a transport of the deposited particles downwards to the bottom of the device by the guide spiral. To ensure that the suspension passes close to the sleeve and the magnetic field a guide tube surrounds the sleeve and the suspension flows in the annular gap in between. In the calming area between the outer wall of the device and the guide tube the fluid slows down again.

In this section, firstly the results of the magnetic field computation are presented. Secondly, the velocity field for a volume flow of $60\,\text{m}^3\,\text{h}^{-1}$ and $120\,\text{m}^3\,\text{h}^{-1}$ is depicted. Thirdly, the particle separation for both volume flows, both particle fractions and $\|\vec{M}_{\text{sat.},l}\|_2 = 45,600\,\text{A}\,\text{m}^{-1}$ as well as $\|\vec{M}_{\text{sat.},l}\|_2 = 265,600\,\text{A}\,\text{m}^{-1}$ is illustrated.

7.3.1   Magnetic field simulation

The magnetic field is generated by 188 permanent magnets of rare earth (e.g. neodymium magnet, $\text{Nd}_2\text{Fe}_{14}\text{B}$) that are arranged in a double helical pattern fixed on an iron drum, see Figure 7.1 (left). One helix contains the magnets with outward directed north pole (red), the other one consists of magnets with outward directed south pole (green). The magnets are of grade N35H with remanence flux density $\|\vec{B}\| = 1.15\,\text{T}$ and magnetization $\|\vec{M}\| = 915,000\,\text{A}\,\text{m}^{-1}$. The relative permeability of neodymium magnets is $\mu_r(\text{neodymium}) = 1.05$ and of the iron drum $\mu_r(\text{iron}) = 4,000$.

The magnitude of the computed magnetic flux density is depicted in the vertical center plane of the separator, Figure 7.2. On the top and on the bottom of the magnetic field, its spacial extension is larger than in between. At both drum ends the magnets do not have any neighboring magnets, the magnetic field lines close. This causes higher field gradients and thus higher magnetic forces that act on the particles. For $y = -0.4\,\text{m}$, the maximum of $\|\vec{B}\|$ is about $0.3\,\text{T}$ directly next to the sleeve, see Figure 7.3. For $y = -0.15\,\text{m}$, it is about $\|\vec{B}\| = 0.35\,\text{T}$. In both cases $\|\vec{B}\|$ decreases along the inner channel to about $0.1\,\text{T}$ at the guide tube. In the calming area in between the outer wall and the guide tube, $\|\vec{B}\|$ is smaller than $0.1\,\text{T}$. Usually, particles do not get there.

7.3.2   Velocity field simulation

The fluid of the suspension is oil ($55°\,\text{C}$, $\rho = 10^3\,\text{kg}\,\text{m}^{-3}$, $\mu = 10^{-3}\,\text{kg}\,\text{m}^{-1}\,\text{s}^{-1}$) and is considered as Newtonian, incompressible and continuous. The Dirichlet velocity boundary condition at the inlet is chosen to form a Poiseuille profile with maximal inflow velocity
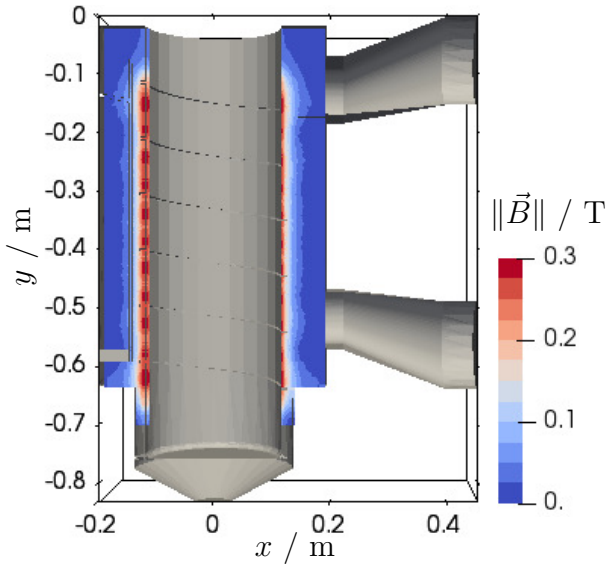
Figure 7.2: The magnetic flux density $\|\vec{B}\|$ is depicted in the centered cross-sectional x-y-plane. Next to the sleeve $\|\vec{B}\|$ is large and decreases rapidly in x-direction within the channel in between sleeve and guiding tube.
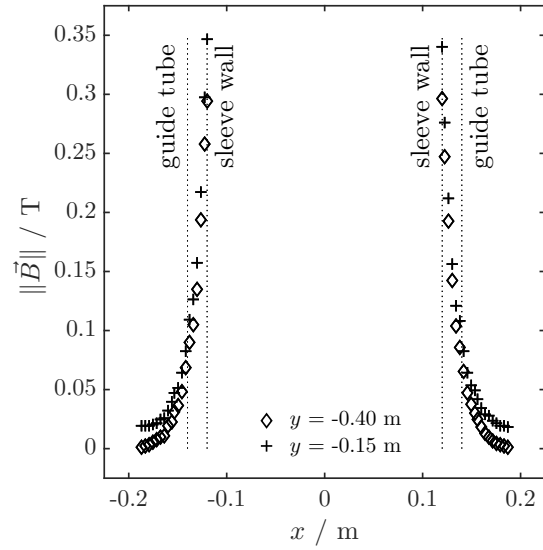
Figure 7.3: Depending on the y-position, $\|\vec{B}\|$ differs. For $y = -0.15\,\mathrm{m}$, $\|\vec{B}\| = 0.35\,\mathrm{T}$ next to the sleeve. $\|\vec{B}\|$ is larger compared to $\|\vec{B}\| = 0.29\,\mathrm{T}$ for $y = -0.40\,\mathrm{m}$. $\|\vec{B}\|$ decreases along the inner channel to about $0.1\,\mathrm{T}$ at the guide tube.

$\vec{u}_{\mathrm{in}}$, Figure 7.1. At the outlet, the pressure is fixed by a Dirichlet boundary condition and given density of one. On the walls, bounce-back behavior is applied that matches a no-slip boundary condition with zero velocity. In case of a volume flow of $60\,\mathrm{m^3\,h^{-1}}$, the maximal velocity of the Poiseuille inflow profile at the boundary is $\|\vec{u}_{\mathrm{in}}\| = 9.4 \times 10^{-1}\,\mathrm{m\,s^{-1}}$ with Smagorinsky constant $c_t = 0.14$. The simulation parameters are $\Delta x = 2.14 \times 10^{-3}$ m, $\Delta t = 2.3 \times 10^{-4}$ s with $\tau = 0.500149$. To enable a volume flow of $120\,\mathrm{m^3\,h^{-1}}$, a maximum velocity of $\|\vec{u}_{\mathrm{in}}\| = 18.8 \times 10^{-1}\,\mathrm{m\,s^{-1}}$ is chosen. Due to reasons of stability, the Smagorinsky constant is increased to $c_t = 0.3$. The simulation parameters are $\Delta x = 1.5 \times 10^{-3}$ m, $\Delta t = 7.5 \times 10^{-5}$ s with $\tau = 0.5001$. The fluid simulation duration is $4.6\,\mathrm{s}$.

In case of the simulation with volume flow $60\,\mathrm{m^3\,h^{-1}}$, the magnitude of the velocity is depicted in the centered vertical cross-sectional area, Figure 7.4. The fluid enters the inlet and is redirected into the annular gap in between guide tube and sleeve. The fluid flow downwards the annular gap is disturbed by the spiral guide and thus is turbulent with a maximum velocity of $1.37\,\mathrm{m\,s^{-1}}$ in the transition to the annular gap. The fluid flows over the guide spiral in a wave-like manner. In the calming area between guide tube and outer wall of the housing the fluid velocity is small. The net pressure loss from inlet to outlet is about
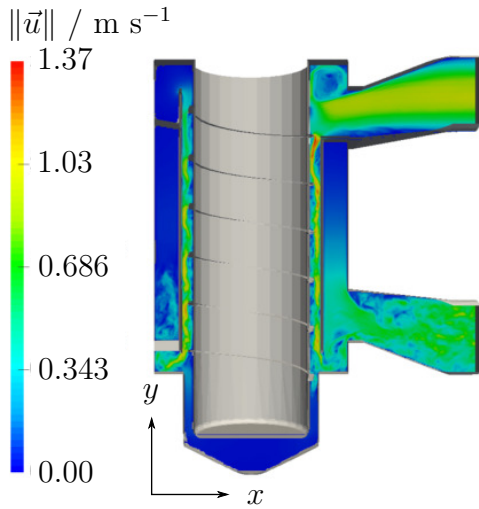
$\|\vec{u}\|$ / m s^{-1}

Figure 7.4: In the $60\,\mathrm{m^3\,h^{-1}}$ simulation, the magnitude of the velocity is shown in the centered, vertical cross-sectional area of the separator, $t = 4.6\,\mathrm{s}$. The flow is turbulent with a maximum velocity at the transition of the inlet to the annular gap.
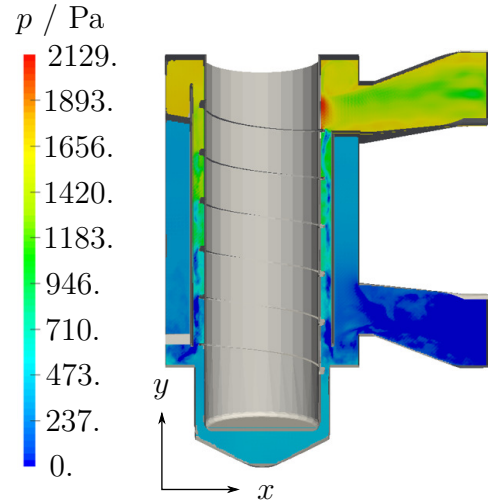
p / Pa

Figure 7.5: In the $60\,\mathrm{m^3\,h^{-1}}$ simulation, the hydro-static pressure is depicted in the centered, vertical cross-sectional area, $t = 4.6\,\mathrm{s}$. The maximum is located next to the sleeve at the inflow side. The net pressure loss from inlet to outlet is about 1,400 Pa.

$1,400\,\mathrm{Pa}$ with a maximum hydro-static pressure of about $2,000\,\mathrm{Pa}$ at the transition from inlet to annular gap, Figure 7.5. In addition to the front view, the magnitude of the velocity is presented in four horizontal cut-planes (a)-(d). The position of the cut-planes within the separator is sketched in Figure 7.6 (left). In cut-plane (a) at the inlet, the Poiseuille inflow profile with maximum velocity of $\|\vec{u}_{\mathrm{in}}\| = 9.4 \times 10^{-1}\,\mathrm{m\,s^{-1}}$ is clearly visible. The velocity decreases as the geometry widens and the turbulence of the flow is visible. In the annular gap, the velocity is higher than in the calming area where it drops down to zero. In cut-planes (b) and (c), the velocity in the calming area and within the annular gap is depicted. Close to the position of cut-plane (d) the fluid escapes the annular gap and is turbulent within the complete cross-sectional area. Compared to the results of the $60\,\mathrm{m^3\,h^{-1}}$ simulation, the results of the $120\,\mathrm{m^3\,h^{-1}}$ simulation look very similar, however the velocities are twice as high as obvious in Figure 7.7. A maximum velocity of $2.8\,\mathrm{m\,s^{-1}}$ is found at the transition from inlet to annular gap. Here, the flow is more turbulent and reaches deeper into the calming area as well as to the bottom of the device.
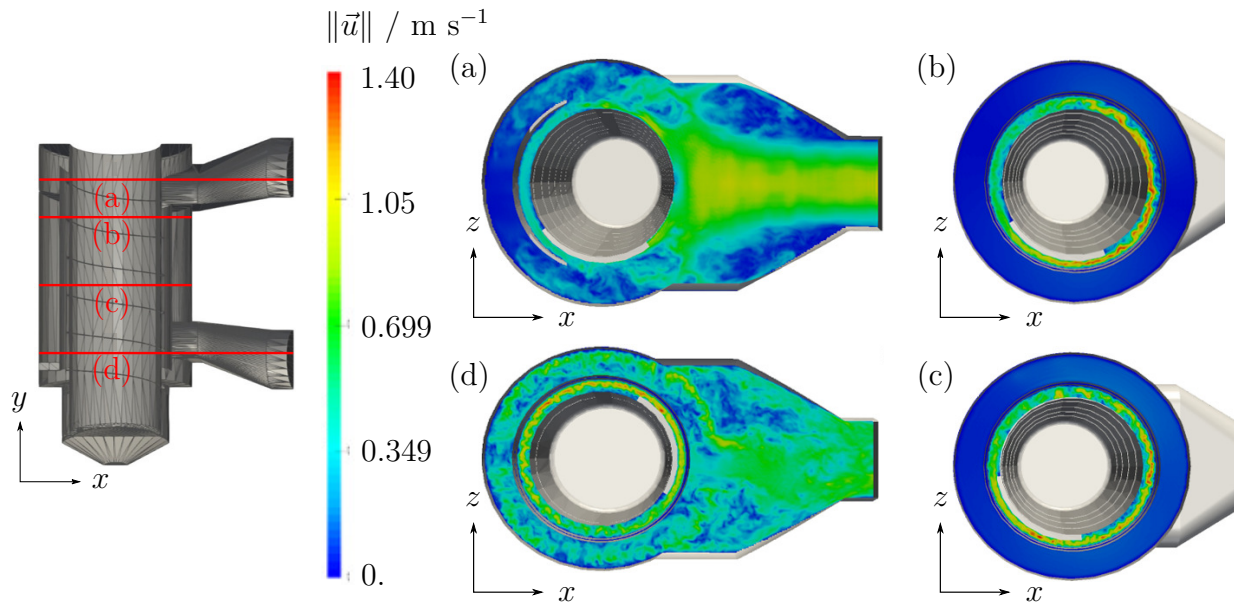
Figure 7.6: The magnitude of the velocity is presented in four horizontal cut-planes (1)-(4), $t = 4.6\,\text{s}$. Their position within the geometry is sketched on the left side.

7.3.3 Magnetic particle separation

The spherical magnetic particles are exposed to both the external magnetic field and the developed flow field of the carrying fluid. The latter is not updated during the particle simulation. The particles are generated at the inlet with the mass concentration given in Table 7.1. Once a particle touches the wall of the sleeve, it remains fixed at this position since the magnetic field is strong enough that it cannot be removed by the considered drag forces once attached. On the other walls, a reflection boundary is applied. The simulation duration is 7.2 s.

The separation of the particle fractions F1 and F2 is examined by visually comparing the final particle depositions after $t = 7.2\,\text{s}$. In Table 7.2, a short overview over the parameter setup of the individual separation simulations (A1, A2, B1, B2, C1, C2) is given. They depend on the particle fraction, the volume flow and the saturation magnetization. In all simulations, all particles remain within the separator. For the presentation of the results, the particles are depicted in a cross-sectional cut with partly present geometry. Separated particles possess the activity zero, freely moving particles the activity one.

Referring to simulation A1, the particles deposit on the upper fifth of the sleeve, mainly on the side facing the inlet, see Figure 7.8. Most of the particles are separated directly after reaching the annular gap. In simulation A2, the particles deposit to the upper half of the sleeve and all around, Figure 7.9. The particle deposition reaches more downwards the
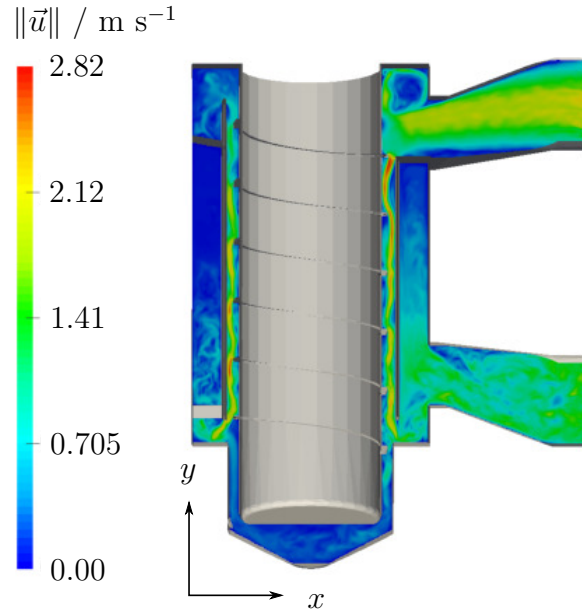
Figure 7.7: Visualization of the magnitude of the velocity in the centered, vertical cross-sectional area, $t = 4.6\,\mathrm{s}$. The flow is turbulent and has its maximum velocity at the transition of the inlet to the annular gap.

annular gap on the side facing the inlet than on the averted side. Compared to A1, they follow the fluid flow for a longer distance. In case of simulation B1, the particles deposit again to the upper fifth of the sleeve with a deposition that is slightly more concentrated towards the inlet than in simulation A1, Figure 7.10. In simulation B2, the particles are separated in the upper fifth of the sleeve and again all around it, Figure 7.11. The deposition is less enlarged downwards the sleeve. In simulation C1, the particles deposit again on the upper fifth of the sleeve mostly in direction to the inlet area, Figure 7.12. There is no noticeable difference to the results of simulation B1 although the volume flow is higher. In simulation

simulation	F1	F2	$60\,\mathrm{m}^3\,\mathrm{h}^{-1}$	$120\,\mathrm{m}^3\,\mathrm{h}^{-1}$	$45,600\,\mathrm{A}\,\mathrm{m}^{-1}$	$265,600\,\mathrm{A}\,\mathrm{m}^{-1}$
A1	✓		✓		✓	
A2		✓	✓		✓	
B1	✓		✓			✓
B2		✓	✓			✓
C1	✓			✓		✓
C2		✓		✓		✓

Table 7.2: Overview over the parameters adjusted for the individual simulations.

C2, the area of deposition is larger compared to simulation B2, Figure 7.13. The particles reach more downwards the annular gap but less than in simulation A2.

Referring to the visual examination of A1, B1 and C1, the final depositions look similar. A good separation is possible for both the high and small volume flows as well as for both saturation magnetizations. Due to the particle size, the acting magnetic force is strong and the inertia is high. The influence of the drag force diminishes in the presence of the magnetic field. In comparison, the deposition area on the sleeve increases from B2 to C2 to A2. Since the F2-particles are small, the magnetic force is small. For a smaller saturation magnetization (A2), or respective higher volume flow (C2), the drag force dominates and the deposition area increases. Concluding, for smaller magnetic particles a higher saturation magnetization, respective a lower volume flow, ensures good separation results. In contrast, for larger magnetic particles the effect of volume flow or saturation magnetization on the deposition is less pronounced.
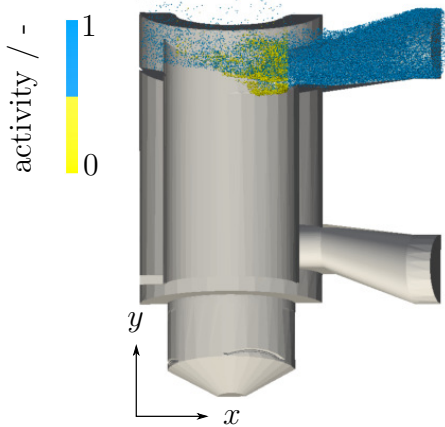
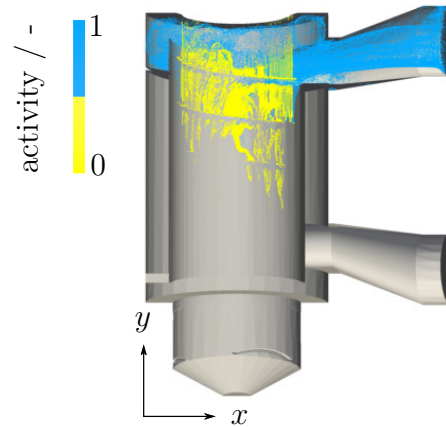**Figure 7.8:** A1 - The particles deposit on the upper fifth of the sleeve.

Figure 7.9: A2 - The particles deposit on the upper half of the sleeve and all around it.
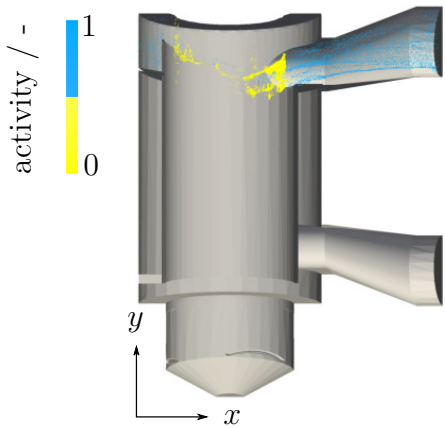
Figure 7.10: B1 - The particles deposit on the upper fifth of the sleeve with more concentrated deposition next to the inlet.
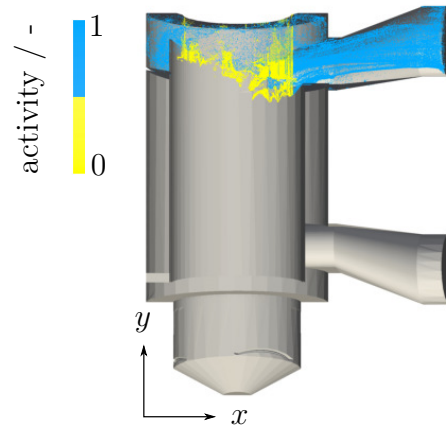

Figure 7.11: B2 - The particles deposit on the upper fifth of the sleeve and all around it.
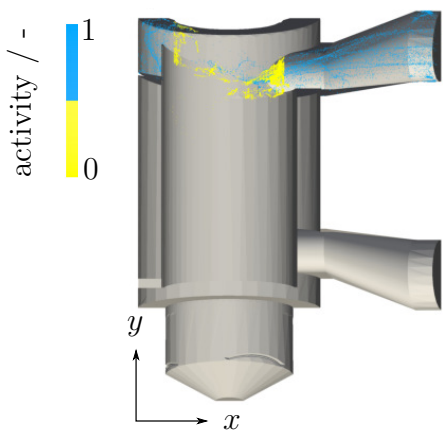

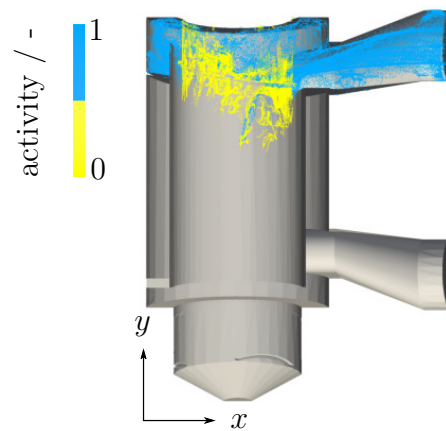**Figure 7.12:** C1 - The particles deposit on the upper fifth of the sleeve, mostly directed towards the inlet.

Figure 7.13: C2 - The particles deposit on the upper third of the sleeve and all around it.

7.4 Conclusion

Simulating the processes in the spiral magnetic separator shows successfully the influence of volume flow, particle size or saturation magnetization on the deposition of the magnetic particles. First, both the magnetic field and the flow field were computed. Subsequently, the magnetic separation of two mono-disperse particle fractions (F1 and F2) was performed for two volume flows and two saturation magnetizations. The particles of F1 show a good separation for the chosen parameter settings. The magnetic force dominates the separation of the large particles, the impact of the drag force is small. The particles of F2 are smaller than the particles of F1. They follow the fluid flow easier due to their smaller inertia and the smaller magnetic force. Thus the influence of the volume flow and the saturation magnetization on the particle separation is more prominent.

For further studies, following improvements to the simulations might be necessary. The consideration of particle-particle contacts and dipole-dipole interactions might be important as the particles form agglomerates. The impact of the particles on the fluid flow should be considered and the computation of the flow field during the particle simulation continued. The use of a continuous model approach to describe the particles might decrease computational costs since this allows for a better parallelization. Further, simulation aspects as e.g. grid independence, stability and turbulence statistics should be studied.

The performed simulations are capable to successfully demonstrate the separation of the magnetic particles for different fluid flow and particle parameters. This provides insight into the dependence of the particle separation on the chosen process parameters. The smaller the magnetic particles, the more important is a carefully chosen parameter setting for a good separation. Furthermore, the simulations are helpful for the prediction of the escape rate for particles with different magnetization. Nevertheless, further parameter studies as well as validation experiments are necessary.

8 Summary, conclusion and outlook

As highlighted in the introduction of this thesis, reactive particle fluid flows occur in a wide range of practical applications in process engineering, e.g. in chemical catalytic reactors, in fluidized bed reactors or in the uptake of phosphorus on C-S-H particles. The purpose of this work arose from the necessity to develop suitable numerical simulation tools to study and optimize such processes. The aim was to contribute novel LBM-based Euler-Lagrange algorithms for reactive particle fluid flows consisting of moving particles that consider a one-way, respective a fully two-way coupling of the components.

Part I of this work dealt with the mathematical models that describe the reactive particle fluid flows. The carrier fluid and the reactive mass transport, respectively, were modeled with the NSE or the VANSE, and the ADRE or the VAADRE, respectively. Insight into the numerical solution by means of the LBM was given afterwards. Newton's equations of motion and the considered forces were introduced to obtain the trajectories of the particles, which were represented by a Lagrange approach. In the following the achieved objectives are summarized.

Part II presented the applications of the methods to demonstrate the potential of the developed framework. In Chapter 5, a novel one-way coupled LBM-based algorithm was applied to study fluid flows and components mixing inclusive consideration of adsorption processes on the surface of moving, in water suspended and disperse sub-grid particles. The model equations were the NSE, respective the ADRE. The main focus was on the validation of the fluid flow and of the reactive substance transport. The components were one-way coupled. The results of the fluid flow simulation agreed very well with the results of the experiments using MRI to depict the fluid velocities. The simulation of the fluid mixing showed similar results as the experiments with water and ink solution that allowed a visual representation of the mixing quality. Additional, grid convergence studies for the mass transport of the reactive substance inclusive reactions were performed and reasonable results were obtained. The potential of the approach to simulate adsorption processes to moving particles could be demonstrated.

A fully coupled simulation of reactive particle fluid flows was achieved by a novel fully two-way coupled multi-scale LBM and DEM, as shown in Chapter 6. The reactive particle fluid flow consisted of the carrier fluid, a reactive substance and submerged, moving and dispersed sub-grid particles. The fluid flow and the reactive mass transport were modeled by a volume averaging method in kind of a continuous framework to determine the displacement by the particles. The considered governing equations were the VANSE and the VAADRE. The two-way coupling was achieved by taking into account drag forces acting on the fluid as well as changes in porosity. The effects on the reactive mass transport were considered both by adapting the diffusion coefficient to the porosity changes and by reactions at the specific surface of the particles. First, a two-way particle fluid flow simulation was carried out without consideration of reactions. For validation, a single particle sedimentation was performed in an initially resting fluid for three different particle sizes. A comparison with experimental results from the literature showed good agreement. Additional grid studies for both fluid and particle velocities confirmed the convergence of the simulations. Afterwards, a fully coupled reactive particle fluid flow simulation was performed in a channel with solid sub-grid particles. In the end, the comparison with a fully resolved pore-scale simulation was very good, the performed grid study converged. The correctness of the fully coupled volume averaging could be demonstrated. The comparison of a one- and two-way coupled multi-particle simulation of thousands of particles showed the true capability of the multi-scale approach being an efficient simulation tool for larger reactive particle fluid flows. In summary, the results obtained by the novel fully coupled volume-averaging method for the simulation of reactive particle fluid systems are encouraging.

Reactive particle fluid flows also occur in biotechnological processes e.g. to specifically separate target proteins from the fermentation broth using surface functionalised magnetic carrier particles. As a first step towards a realistic simulation of an entire reaction and separation process, the particle fluid flow in a complete magnetic separation device was chosen by means of a one-way coupled approach given in Chapter 7. The influence of volume flow, particle size or saturation magnetization on the separation of the magnetic particles gave information about how to chose optimal process parameters for a good particle separation. The separation behavior for different flow velocities and different particle parameters as particle size and saturation magnetization were investigated. The smaller the magnetic particles, the smaller the acting magnetic forces and the slower the separation. The presented approach is capable to carefully predict a proper parameter setting for a good separation process.

Both the one-way, Chapter 5, and the two-way, Chapter 6, coupled methods provide

an efficient numerical framework to simulate reactive particle fluid systems. As shown in Chapter 7, the use of the presented methods is generally possible both in realistic systems and in large devices. Further validation through experimental studies would pave the way for many more process engineering applications. Still, more investigations are necessary since e.g. shear flows at the particle surface influence the reaction processes. A precise observation of the reactive substance distribution in the immediate vicinity of the particles, e.g. by two-way coupling, is important since it is exposed to a dynamic change due to the flow conditions. Since reactive particle fluid flows usually do not consist of mono-disperse particles, particle size distribution and, if necessary, shape and surface of the particles have to be considered.

The thesis demonstrated that a suitable simulation tool that relates the fluid flow and the reaction processes on the particles to each other, is of essential use. In future work, the determination of the model equations of reaction kinetics by means of numerical investigations would enable a fundamental and new insight into the calculation of reaction kinetics detached from empirically determined parameters. Its direct use in reactive particle fluid flow simulations would help to predict and to optimize the uptake of reactive substances. The reaction kinetics of the nanoscale reaction process could be determined by using a molecular dynamic approach and suitable potential equations at pore or particle surface. The simulation could be performed with a coarse-grained model based on DEM. The obtained reaction kinetics could be transferred to micro- and macroscale flow simulations and coupled with the LBM.

A Algorithm related to Chapter 6

Algorithm 1 Overall coupling algorithm

Setup the **initial** and **boundary condition** in *Yantra* for VANSE and for VAADRE

Initialize *Yade* engines with **NewtonIntegrator()** and
ForceResetter(gravity=(0,0,0),damping=0.)

Initialize particle properties

Set $\Delta t = \min(\Delta t_{Yade}, \Delta t_{Yantra,\mathrm{VANSE}}, \Delta t_{Yantra,\mathrm{VAADRE}})$

Start numerical scheme

While $t \leq t_{\mathrm{end}}$:

DEM computation

Compute $s_l(t, \vec{x})$ by (4.20)

Compute $\langle \vec{u} \rangle(t, \vec{x}_l(t))$ by (4.19)

Compute $\frac{\mathrm{D}\langle \vec{u} \rangle(t, \vec{x}_l(t))}{\mathrm{D}t}$, $\frac{\mathrm{d}\,\vec{u}_l(t)}{\mathrm{d}\,t}$ with $\langle \vec{u} \rangle(t - \Delta t, \vec{x}_l(t - \Delta t))$ and $\vec{u}_l(t - \Delta t)$

Compute the relevant forces and torques

Solve the **new particle position** $\vec{x}_l(t + \Delta t)$ and the **new particle velocity** $\vec{u}_l(t + \Delta t)$ by (6.2)

Compute the **force density** $\vec{f}_{\mathrm{d}}(t, \vec{x})$ by (4.21) and the **porosity** $\phi(t, \vec{x})$ by (4.22)

LBM VANSE computation

Compute $\langle \vec{u} \rangle(t, \vec{x})^{\mathrm{eq}}$ by (3.6), $f_i^{\mathrm{eq}}(t, \vec{x})$ by (3.5), $\Omega_i^{\mathrm{F}}(t, \vec{x})$ by (3.7)

Execute **collision step** $(t_{\mathrm{collision}})$: $f_i(t_{\mathrm{collision}}, \vec{x}) = f_i(t, \vec{x}) + \Omega_i^{\mathrm{BGK}}(t, \vec{x}) + \Omega_i^{\mathrm{F}}(t, \vec{x})$

Compute $\Omega_i^{\mathrm{PCR}}(t, \vec{x})$ by (3.10)

Execute **pressure correction** (t_{PCR}): $f_i(t_{\mathrm{PCR}}, \vec{x}) = f_i(t_{\mathrm{collision}}, \vec{x}) + \Omega_i^{\mathrm{PCR}}(t, \vec{x})$

Execute **streaming step**: $f_i(t + \Delta t, \vec{x} + \vec{c}_i \Delta t) = f_i(t_{\mathrm{PCR}}, \vec{x})$

Compute the **macroscopic variables** for $t + \Delta t$ by (3.8)

LBM VAADRE computation

Compute $\Omega_j^{\mathrm{RXN}}(t, \vec{x})$ by (3.13) and (4.23), $g_j^{\mathrm{eq}}(t, \vec{x})$ by (3.14)

Compute **macroscopic variables** by (3.16)

Execute **collision step** $(t_{\mathrm{collision}})$: $g_j(t_{\mathrm{collision}}, \vec{x}) = g_j(t, \vec{x}) + \Omega_j^{\mathrm{TRT}}(t, \vec{x}) + \Omega_j^{\mathrm{RXN}}(t, \vec{x})$

Execute **streaming step**: $g_j(t + \Delta t, \vec{x} + \vec{c}_i \Delta t) = g_j(t_{\mathrm{collision}}, \vec{x})$

B Algorithm related to Chapter 7

Algorithm 2 Separation of magnetized particles in the spiral magnetic separator.

Setup the initial and boundary conditions for LBM and DEM

Integrate the stl-file of the separator geometry

While $t \leq 4.6$ s:

   LBM computation including Smagorinsky-Lilly model (Section 2.3.6)

Load the magnetic field data

Compute the gradient of the magnetic field

While $t \leq 7.2$ s:

   DEM computation

      Generate particles at the inlet

      Compute $\vec{F}_{\mathrm{drag},l}(t)$ and $\vec{F}_{\mathrm{mag.},l}(t)$

      Solve the **new particle position** and the **new particle velocity**

C Publications and congress proceedings

Publications and submitted articles

M.-L. Maier, R. A. Patel, N. I. Prasianakis, S. V. Churakov, H. Nirschl, and M. J. Krause. "Coupling of multiscale lattice Boltzmann discrete-element method for reactive particle fluid flows". In: *Phys. Rev. E* 103 (3 2021), p. 033306. DOI: `10.1103/PhysRevE.103.033306`

M.-L. Maier, S. Milles, S. Schuhmann, G. Guthausen, H. Nirschl, and M. J. Krause. "Fluid flow simulations verified by measurements to investigate adsorption processes in a static mixer". In: *Computers & Mathematics with Applications* 76 (2018), pp. 2744–2757. DOI: `10.1016/j.camwa.2018.08.066`

M.-L. Maier, T. Henn, G. Thaeter, H. Nirschl, and M. J. Krause. "Multiscale simulation with a two-way coupled lattice Boltzmann method and discrete element method". In: *Chemical Engineering & Technology* 40.9 (2017), pp. 1591–1598. ISSN: 1521-4125. DOI: `10.1002/ceat.201600547`

International congress proceedings

M.-L. Maier, "Magnetic particle dynamics combined with protein purification modeled by Euler and Lagrange approaches", 12 European Fluid Mechanics Conference (EFMC12), Vienna, Austria (2018).

M.-L. Maier, "Comparison of Physical and Numerical Experiments of Adsorption Processes in a Static Micro-Mixer", International Conference for Mesoscopic Methods in Engineering and Science (ICMMES), Nantes, France (2017).

M.-L. Maier, "Numerical Simulation of Magnetic Particle Separation: First Validation Results to LBM-DEM Coupling", International Congress on Particle Technology (PARTEC), Nuernberg, Germany (2016).

Bibliography

[1]   U. Berg, G. Knoll, E. Kaschka, V. Kreutzer, D. Donnert, P. Weidler, and R. Nüesch. "P-RoC-Phosphorus recovery from wastewater by crystallisation of calcium phosphate compounds". In: *Journal of residuals science and technology* 4.3 (2005).

[2]   C. K. Aidun and J. R. Clausen. "Lattice-Boltzmann method for complex flows". In: *Annual review of fluid mechanics* 42 (2010), pp. 439–472.

[3]   M. J. Krause, T. Gengenbach, and V. Heuveline. "Hybrid parallel simulations of fluid flows in complex geometries: Application to the human lungs". In: *European Conference on Parallel Processing.* Springer. 2010, pp. 209–216.

[4]   B. Blais, J.-M. Tucny, D. Vidal, and F. Bertrand. "A conservative lattice Boltzmann model for the volume-averaged Navier–Stokes equations based on a novel collision operator". In: *Journal of Computational Physics* 294 (2015), pp. 258–273.

[5]   H. Freund, T. Zeiser, F. Huber, E. Klemm, G. Brenner, F. Durst, and G. Emig. "Numerical simulations of single phase reacting flows in randomly packed fixed-bed reactors and experimental validation". In: *Chemical engineering science* 58.3-6 (2003), pp. 903–910.

[6]   L. Zhou, Z. Qu, T. Ding, and J. Miao. "Lattice Boltzmann simulation of the gas-solid adsorption process in reconstructed random porous media". In: *Physical Review E* 93.4 (2016), p. 043101.

[7]   S. Sullivan, F. Sani, M. Johns, and L. Gladden. "Simulation of packed bed reactors using lattice Boltzmann methods". In: *Chemical Engineering Science* 60.12 (2005), pp. 3405–3418.

[8]   S. Agarwal, N. Verma, and D. Mewes. "A lattice Boltzmann model for adsorption breakthrough". In: *Heat and Mass Transfer* 41.9 (2005), pp. 843–854. ISSN: 1432-1181. DOI: 10.1007/s00231-005-0625-x.

[9]   N. Manjhi, N. Verma, K. Salem, and D. Mewes. "Simulation of 3D velocity and concentration profiles in a packed bed adsorber by lattice Boltzmann methods". In: *Chemical Engineering Science* 61.23 (2006), pp. 7754–7765. ISSN: 0009-2509. DOI: https://doi.org/10.1016/j.ces.2006.09.028.

[10]   R. A. Patel, J. Perko, D. Jacques, G. De Schutter, G. Ye, and K. Van Breugel. "A three-dimensional lattice Boltzmann method based reactive transport model to simulate changes in cement paste microstructure due to calcium leaching". In: *Construction and Building Materials* 166 (2018), pp. 158–170.

[11]   M.-L. Maier, S. Milles, S. Schuhmann, G. Guthausen, H. Nirschl, and M. J. Krause. "Fluid flow simulations verified by measurements to investigate adsorption processes in a static mixer". In: *Computers & Mathematics with Applications* 76 (2018), pp. 2744–2757. DOI: 10.1016/j.camwa.2018.08.066.

[12]   M. J. Krause, A. Kummerländer, S. J. Avis, H. Kusumaatmaja, D. Dapelo, F. Klemens, M. Gaedtke, N. Hafen, A. Mink, R. Trunk, J. E. Marquardt, M.-L. Maier, M. Haussmann, and S. Simonis. "Openlb—open source lattice Boltzmann code". In: *Computers & Mathematics with Applications* (2020).

[13]   R. A. Patel. "Lattice Boltzmann method based framework for simulating physico-chemical processes in heterogeneous porous media and its application to cement paste". PhD thesis. Ghent University, 2016.

[14]   R. Patel. 2016. URL: https://bitbucket.org/yantralbm/yantra.

[15]   COMSOL AB, Stockholm, Sweden. *COMSOL Multiphysics® v. 5.3.* URL: www.comsol.com.

[16]   J. Lindner, K. Menzel, and H. Nirschl. "Parameters influencing magnetically enhanced centrifugation for protein separation". In: *Chemical Engineering Science* 97 (2013), pp. 385–393.

[17]   Z. Guo and C. Shu. *Lattice Boltzmann method and its applications in engineering.* Vol. 3. Advances in computational fluid dynamics 3. World Scientific, 2013. ISBN: 978-981-4508-29-2.

[18]   G. K. Batchelor. *An introduction to fluid dynamics.* 9. print. Cambridge mathematical library. Cambridge [u.a.]: Cambridge Univ. Press, 2007.

[19] T. Krüger, H. Kusumaatmaja, A. Kuzmin, O. Shardt, G. Silva, and E. M. Viggen. *The lattice Boltzmann method.* Springer, 2017. ISBN: 978-3-319-44649-3. DOI: 10.1007/978-3-319-44649-3.

[20] R. B. Bird. "Transport phenomena". In: *Applied Mechanics Reviews* 55.1 (2002), R1–R4. DOI: 10.1115/1.1424298.

[21] M. C. Sukop and D. T. Thorne. "Lattice Boltzmann Modeling Lattice Boltzmann Modeling". In: (2006).

[22] A. Mohamad. *Lattice Boltzmann Method.* Vol. 70. Springer, 2011.

[23] P. L. Bhatnagar, E. P. Gross, and M. Krook. "A Model for Collision Processes in Gases. I. Small Amplitude Processes in Charged and Neutral One-Component Systems". In: *Physical Review* 94.3 (3 1954), pp. 511–525. DOI: 10.1103/PhysRev.94.511.

[24] C. Cercignani. "The Boltzmann equation". In: *The Boltzmann equation and its applications.* Springer, 1988, pp. 40–103.

[25] U. Frisch, D. d'Humieres, B. Hasslacher, P. Lallemand, Y. Pomeau, and J.-P. Rivet. *Lattice gas hydrodynamics in two and three dimensions.* Tech. rep. Los Alamos National Lab., NM (USA); Observatoire de Nice, 06 (France); 1986.

[26] X. He and L.-S. Luo. "Lattice Boltzmann model for the incompressible Navier-Stokes equation". In: *Journal of statistical Physics* 88.3 (1997), pp. 927–944. DOI: 10.1023/B:JOSS.0000015179.12689.e4.

[27] R. R. Nourgaliev, T.-N. Dinh, T. G. Theofanous, and D. Joseph. "The lattice Boltzmann equation method: theoretical interpretation, numerics and implications". In: *International Journal of Multiphase Flow* 29.1 (2003), pp. 117–169.

[28] X. Shan, X.-F. Yuan, and H. Chen. "Kinetic theory representation of hydrodynamics: a way beyond the Navier–Stokes equation". In: *Journal of Fluid Mechanics* 550 (2006), pp. 413–441.

[29] E. M. Viggen. "The lattice Boltzmann method: Fundamentals and acoustics". In: (2014).

[30] D. Hänel. *Molekulare Gasdynamik: Einführung in die kinetische Theorie der Gase und Lattice-Boltzmann-Methoden.* Springer-Verlag, 2006.

[31] D. A. Wolf-Gladrow. *Lattice-gas cellular automata and lattice Boltzmann models: an introduction.* Springer, 2004.

[32] M. C. Sukop and D. T. Thorne. *Lattice Boltzmann modeling: an introduction for geoscientists and engineers.* 2., corr. print. Berlin: Springer, 2007. ISBN: 3-540-27981-4; 978-3-540-27981-5.

[33] X. He and L.-S. Luo. "Theory of the lattice Boltzmann method: From the Boltzmann equation to the lattice Boltzmann equation". In: *Physical Review E* 56.6 (1997), p. 6811.

[34] S. Ubertini, P. Asinari, and S. Succi. "Three ways to lattice Boltzmann: a unified time-marching picture". In: *Physical Review E* 81.1 (2010), p. 016311.

[35] M. J. Krause. "Fluid Flow Simulation and Optimisation with Lattice Boltzmann Methods on High Performance Computers - Application to the Human Respiratory System". PhD thesis. 2010. DOI: `10.5445/IR/1000019768`.

[36] S. Succi. *The lattice Boltzmann equation: for fluid dynamics and beyond.* Oxford university press, 2001.

[37] Q. Zou and X. He. "On pressure and velocity boundary conditions for the lattice Boltzmann BGK model". In: *Physics of fluids* 9.6 (1997), pp. 1591–1598. DOI: `10.1063/1.869307`.

[38] B. Chopard, A. Dupuis, A. Masselot, and P. Luthi. "Cellular automata and lattice Boltzmann techniques: An approach to model and simulate complex systems". In: *Advances in complex systems* 5.02n03 (2002), pp. 103–246.

[39] M. Junk and Z. Yang. "Outflow boundary conditions for the lattice Boltzmann method". In: *Progress in Computational Fluid Dynamics,* 8.1–4 (2008), pp. 38–38. DOI: `10.1504/PCFD.2008.018077`.

[40] Z. Guo, C. Zheng, and B. Shi. "Discrete lattice effects on the forcing term in the lattice Boltzmann method". In: *Physical Review E* 65.4 (2002), p. 046308.

[41] G. Hauke. *An introduction to fluid mechanics and transport phenomena.* Vol. 86. Springer, 2008.

[42] H. K. Versteeg, H. K. Henk Kaarle Versteeg AACR: Versteeg, and W. Malalasekera. *An introduction to computational fluid dynamics : the finite volume method.* Ed. by W. Weeratunge Malalasekera AACR: Malalasekera. 2. ed. Harlow [u.a.]: Pearson/Prentice Hall, 2007. ISBN: 0131274988; 9780131274983.

[43] B. Andersson, R. Andersson, L. Håkansson, M. Mortensen, R. Sudiyo, and B. Van Wachem. *Computational fluid dynamics for engineers*. Cambridge University Press, 2011.

[44] S. Hou, J Sterling, S. Chen, and G. Doolen. "A lattice Boltzmann subgrid model for high Reynolds number flows". In: *arXiv preprint comp-gas/9401004* (1994).

[45] A. A. Mohamad. *Lattice Boltzmann method: fundamentals and engineering applications with computer codes*. London / New York: Springer Science & Business Media, 2011.

[46] R. Trunk, T. Henn, W. Dörfler, H. Nirschl, and M. J. Krause. "Inertial dilute particulate fluid flow simulations with an Euler–Euler lattice Boltzmann method". In: *Journal of Computational Science* 17.Part 2 (2016), pp. 438–445. DOI: 10.1016/j.jocs.2016.03.013.

[47] M.-L. Maier, R. A. Patel, N. I. Prasianakis, S. V. Churakov, H. Nirschl, and M. J. Krause. "Coupling of multiscale lattice Boltzmann discrete-element method for reactive particle fluid flows". In: *Phys. Rev. E* 103 (3 2021), p. 033306. DOI: 10.1103/PhysRevE.103.033306.

[48] S. Whitaker. *The method of volume averaging*. Vol. 13. Springer Science & Business Media, 2013.

[49] H. Enwald, E. Peirano, and A.-E. Almstedt. "Eulerian two-phase flow theory applied to fluidization". In: *International Journal of Multiphase Flow* 22 (1996), pp. 21–66.

[50] L. Wang, L.-P. Wang, Z. Guo, and J. Mi. "Volume-averaged macroscopic equation for fluid flow in moving porous media". In: *International Journal of Heat and Mass Transfer* 82 (2015), pp. 357–368.

[51] B. D. Wood, F. Cherblanc, M. Quintard, and S. Whitaker. "Volume averaging for determining the effective dispersion tensor: closure using periodic unit cells and comparison with ensemble averaging". In: *Water resources research* 39.8 (2003).

[52] S. Torquato and H. Haslach Jr. "Random heterogeneous materials: microstructure and macroscopic properties". In: *Appl. Mech. Rev.* 55.4 (2002), B62–B63.

[53] L. Weber, J. Dorn, and A. Mortensen. "On the electrical conductivity of metal matrix composites containing high volume fractions of non-conducting inclusions". In: *Acta Materialia* 51.11 (2003), pp. 3199–3211.

[54] P. Pivonka, C. Hellmich, and D. Smith. "Microscopic effects on chloride diffusivity of cement pastes—a scale-transition analysis". In: *Cement and Concrete Research* 34.12 (2004), pp. 2251–2260.

[55] J. Zhang, L. Wang, and J. Ouyang. "Lattice Boltzmann model for the volume-averaged Navier-Stokes equations". In: *EPL (Europhysics Letters)* 107.2 (2014), p. 20001.

[56] S. B. Höcker, R. Trunk, W. Dörfler, and M. J. Krause. "Towards the simulations of inertial dense particulate flows with a volume-averaged lattice Boltzmann method". In: *Computers & Fluids* 166 (2018), pp. 152–162.

[57] A. Vikhansky and I. Ginzburg. "Taylor dispersion in heterogeneous porous media: Extended method of moments, theory, and modelling with two-relaxation-times lattice Boltzmann scheme". In: *Physics of Fluids* 26.2 (2014), p. 022104.

[58] I. Ginzburg, D. d'Humières, and A. Kuzmin. "Optimal stability of advection-diffusion lattice Boltzmann models with two relaxation times for positive/negative equilibrium". In: *Journal of Statistical Physics* 139.6 (2010), pp. 1090–1143.

[59] A. B. Basset. *A treatise on hydrodynamics: with numerous examples.* Vol. 2. Deighton, Bell and Company, 1888.

[60] J. Boussinesq. *Théorie analytique de la chaleur mise en harmonic avec la thermodynamique et avec la théorie mécanique de la lumière: Tome I-[II].* Vol. 2. Gauthier-Villars, 1903.

[61] C. W. Oseen. "Neuere Methoden und Ergebnisse in der Hydrodynamik". In: *Leipzig: Akademische Verlagsgesellschaft mb H.* (1927).

[62] T. Chan-Mou. *Mean value and correlation problems connected with the motion of small particles suspended in a turbulent fluid.* Springer, 2013.

[63] K. Hiltunen, A. Jäsberg, S. Kallio, H. Karema, M. Kataja, A. Koponen, M. Manninen, and V. Taivassalo. "Multiphase flow dynamics". In: *Theory and Numerics. Tech. Rep* 722 (2009).

[64] C. T. Crowe, J. D. Schwarzkopf, M. Sommerfeld, and Y. Tsuji. *Multiphase flows with droplets and particles.* CRC press, 2011.

[65] R. Clift, J. R. Grace, and M. E. Weber. *Bubbles, drops, and particles.* Academic Press, 1978.

[66] G. G. Stokes. *On the effect of the internal friction of fluids on the motion of pendulums.* Vol. 9. Pitt Press Cambridge, 1851.

[67] L. Schiller and A. Naumann. "Über die grundlegenden Berechnungen bei der Schwerkraftaufbereitung". In: *Z. Vereines Deutscher Inge.* 77 (1933), pp. 318–321.

[68] M. A. Habte and C. Wu. "Particle sedimentation using hybrid lattice Boltzmann-immersed boundary method scheme". In: *Powder technology* 315 (2017), pp. 486–498.

[69] J. S. Marshall and S. Li. *Adhesive particle flow.* Cambridge University Press, 2014.

[70] N. Mordant and J.-F. Pinton. "Velocity measurement of a settling sphere". In: *The European Physical Journal B-Condensed Matter and Complex Systems* 18.2 (2000), pp. 343–352.

[71] T. Auton, J. Hunt, and M. Prud'Homme. "The force exerted on a body in inviscid unsteady non-uniform rotational flow". In: *Journal of Fluid Mechanics* 197 (1988), pp. 241–257.

[72] N. Deen, M. V. S. Annaland, M. A. Van der Hoef, and J. Kuipers. "Review of discrete particle modeling of fluidized beds". In: *Chemical engineering science* 62.1-2 (2007), pp. 28–44.

[73] P. A. Cundall and O. D. Strack. "A discrete numerical model for granular assemblies". In: *geotechnique* 29.1 (1979), pp. 47–65.

[74] H. Kruggel-Emden, E. Simsek, S. Rickelt, S. Wirtz, and V. Scherer. "Review and extension of normal force models for the discrete element method". In: *Powder Technology* 171.3 (2007), pp. 157–173.

[75] V. Šmilauer and B. Chareyre. "Yade DEM formulation". In: *Yade Documentation* 393 (2010).

[76] V. Smilauer and B. Chareyre. *DEM Formulation.* Nov. 2015. DOI: 10.5281/zenodo. 34044. URL: https://doi.org/10.5281/zenodo.34044.

[77] V. Smilauer, E. Catalano, B. Chareyre, S. Dorofeenko, J. Duriez, N. Dyck, J. Elias, B. Er, A. Eulitz, A. Gladky, C. Jakob, F. Kneib, J. Kozicki, D. Marzougui, R. Maurin, C. Modenese, L. Scholtes, L. Sibille, J. Stransky, T. Sweijen, K. Thoeni, and C. Yuan. *Reference Manual.* Nov. 2015. DOI: 10.5281/zenodo.34045. URL: https://doi.org/10.5281/zenodo.34045.

[78] S. McNamara, E. G. Flekkøy, and K. J. Måløy. "Grains and gas flow: Molecular dynamics with hydrodynamic interactions". In: *Physical review E* 61.4 (2000), p. 4054.

[79] L. Goren, E. Aharonov, D. Sparks, and R. Toussaint. "The mechanical coupling of fluid-filled granular material under shear". In: *Pure and Applied Geophysics* 168.12 (2011), pp. 2289–2323.

[80] A. Damsgaard, D. L. Egholm, J. A. Piotrowski, S. Tulaczyk, N. K. Larsen, and C. Brædstrup. "A new methodology to simulate subglacial deformation of water-saturated granular material". In: *The Cryosphere* 9.6 (2015), pp. 2183–2200.

[81] C.-T. Hsu and P. Cheng. "Thermal dispersion in a porous medium". In: *International Journal of Heat and Mass Transfer* 33.8 (1990), pp. 1587–1597.

[82] A. Brand, L. Allen, M. Altman, M. Hlava, and J. Scott. "Beyond authorship: attribution, contribution, collaboration, and credit". In: *Learned Publishing* 28.2 (2015), pp. 151–155.

[83] M. Levesque, M. Duvail, I. Pagonabarraga, D. Frenkel, and B. Rotenberg. "Accounting for adsorption and desorption in lattice Boltzmann simulations". In: *Phys. Rev. E* 88 (1 2013), p. 013308. DOI: 10.1103/PhysRevE.88.013308.

[84] M. Mantle, A. Sederman, and L. Gladden. "Single- and two-phase flow in fixed-bed reactors: MRI flow visualisation and lattice Boltzmann simulations". In: *Chemical Engineering Science* 56.2 (2001), pp. 523–529. DOI: 10.1016/S0009-2509(00)00256-6.

[85] B. Manz, L. Gladden, and P. Warren. "Flow and dispersion in porous media: Lattice-Boltzmann and NMR studies". In: *AIChE journal* 45.9 (1999), pp. 1845–1854. DOI: 10.1002/aic.690450902.

[86] T. Henn, G. Thäter, W. Dörfler, H. Nirschl, and M. J. Krause. "Parallel dilute particulate flow simulations in the human nasal cavity". In: *Computers & Fluids* 124.Supplement C (2016), pp. 197 –207. ISSN: 0045-7930. DOI: https://doi.org/10.1016/j.compfluid.2015.08.002.

[87] E. Worch. *Adsorption technology in water treatment: fundamentals, processes, and modeling*. Walter de Gruyter, 2012. ISBN: 978-3-11-024022-1.

[88] D. Anderl, M. Bauer, C. Rauh, U. Rude, and A. Delgado. "Numerical simulation of adsorption and bubble interaction in protein foams using a lattice Boltzmann method". In: *Food Funct.* 5 (4 2014), pp. 755–763. DOI: 10.1039/C3FO60374A.

[89] S. Chen and G. D. Doolen. "Lattice Boltzmann method for fluid flows". In: *Annual Review of Fluid Mechanics* 30.1 (1998), pp. 329–364. DOI: `10.1146/annurev.fluid.30.1.329`.

[90] C. Aidun and J. Clausen. "Lattice Boltzmann method for complex flows". In: *Annual Review of Fluid Mechanics* 42.1 (2010), pp. 439–472. DOI: `10.1146/annurev-fluid-121108-145519`.

[91] M.-L. Maier, T. Henn, G. Thaeter, H. Nirschl, and M. J. Krause. "Multiscale simulation with a two-way coupled lattice Boltzmann method and discrete element method". In: *Chemical Engineering & Technology* 40.9 (2017), pp. 1591–1598. ISSN: 1521-4125. DOI: `10.1002/ceat.201600547`.

[92] V. Heuveline, M. J. Krause, and J. Latt. "Towards a hybrid parallelization of lattice Boltzmann methods". In: *Computers & Mathematics with Applications* 58.5 (2009), pp. 1071–1080. ISSN: 0898-1221. DOI: `10.1016/j.camwa.2009.04.001`.

[93] J. Fietz, M. Krause, C. Schulz, P. Sanders, and V. Heuveline. "Optimized hybrid parallel lattice Boltzmann fluid flow simulations on complex geometries". In: *Euro-Par 2012 Parallel Processing* (2012), pp. 818–829. DOI: `10.1007/978-3-642-32820-6_81`.

[94] R. Kimmich. *NMR: tomography, diffusometry, relaxometry.* Springer Science & Business Media, 2012.

[95] P. T. Callaghan. *Principles of nuclear magnetic resonance microscopy.* Oxford University Press on Demand, 1993.

[96] V. Hessel, H. Löwe, and F. Schönfeld. "Micromixers - a review on passive and active mixing principles". In: *Chemical Engineering Science* 60.8 (2005), pp. 2479–2501. ISSN: 0009-2509. DOI: `10.1016/j.ces.2004.11.033`.

[97] M. Spiga and G. Morino. "A symmetric solution for velocity profile in laminar flow through rectangular ducts". In: *International Communications in Heat and Mass Transfer* 21.4 (1994), pp. 469 –475. ISSN: 0735-1933. DOI: `https://doi.org/10.1016/0735-1933(94)90046-9`.

[98] N. Kockmann. *Transport phenomena in micro process engineering.* Springer Science & Business Media, 2007. DOI: `10.1007/978-3-540-74618-8`.

[99]   A. Mink, G. Thäter, H. Nirschl, and M. J. Krause. "A 3D lattice Boltzmann method for light simulation in participating media". In: *Journal of Computational Science* 17.Part 2 (2016), pp. 431–437. ISSN: 1877-7503. DOI: `https://doi.org/10.1016/j.jocs.2016.03.014`.

[100]   J. Bear. "Dynamics of fluids in porous media. Elsevier, New York." In: *Dynamics of fluids in porous media. Elsevier, New York.* (1972).

[101]   M. T. Van Genuchten and W. Alves. *Analytical solutions of the one-dimensional convective-dispersive solute transport equation.* 1661. US Department of Agriculture, Agricultural Research Service, 1982.

[102]   Y. Tsuji. "Multi-scale modeling of dense phase gas–particle flow". In: *Chemical Engineering Science* 62.13 (2007), pp. 3410–3418.

[103]   Z. Zhang, X. Wang, and J. Zhao. "Phosphate recovery from wastewater using calcium silicate hydrate (CSH): sonochemical synthesis and properties". In: *Environmental Science: Water Research & Technology* 5.1 (2019), pp. 131–139.

[104]   R. A. Patel, J. Perko, D. Jacques, G. De Schutter, K. Van Breugel, and G. Ye. "A versatile pore-scale multicomponent reactive transport approach based on lattice Boltzmann method: Application to portlandite dissolution". In: *Physics and Chemistry of the Earth, Parts A/B/C* 70 (2014), pp. 127–137.

[105]   Z. Guo and C. Shu. *Lattice Boltzmann method and its applications in engineering.* Vol. 3. World Scientific, 2013.

[106]   C. Rettinger and U. Rüde. "A coupled lattice Boltzmann method and discrete element method for discrete particle simulations of particulate flows". In: *Computers & Fluids* 172 (2018), pp. 706–719.

[107]   T. Baldock, M. Tomkins, P Nielsen, and M. Hughes. "Settling velocity of sediments at high concentrations". In: *Coastal engineering* 51.1 (2004), pp. 91–100.

[108]   S. H. Kim and H. Pitsch. "A generalized periodic boundary condition for lattice Boltzmann method simulation of a pressure driven flow in a periodic geometry". In: *Physics of Fluids* 19.10 (2007), p. 108101.

[109]   K. Menzel, J. Lindner, and H. Nirschl. "Removal of magnetite particles and lubricant contamination from viscous oil by High-Gradient Magnetic Separation technique". In: *Separation and Purification Technology* 92 (2012), pp. 122–128.

[110] J. Weschke, U. Löffler, J. Schiebel, and J. Brenk. "Device and method for separating magnetizable particles from a fluid". German. Pat. WO/2014/161819. 2014.

[111] S. G. Frantz. "Magnetic separator". Pat. US Patent 2,074,085. 1937.

[112] J. Svoboda. *Magnetic techniques for the treatment of materials.* Springer Science & Business Media, 2004.

[113] B. C. Fuchs, C. Hoffmann, K. Keller, and C. M. Rey. "Magnetic field and field gradient enhanced centrifugation solid-liquid separations". Pat. US Patent 8,012,357. 2011.

[114] J. Lindner, K. Wagner, C. Eichholz, and H. Nirschl. "Efficiency optimization and prediction in High-Gradient Magnetic Centrifugation". In: *Chemical engineering & technology* 33.8 (2010), pp. 1315–1320.

[115] A. Bettini. *A Course in Classical Physics: Electromagnetism.* Springer, 2016.

[116] C. Eichholz. *Zur magnetfeldinduzierten Strukturierung von Filterkuchen: Experimenteller Nachweis, Simulation und Anwendung in der selektiven Bioseparation.* Cuvillier Verlag Göttingen, Germany, 2010.

[117] J. Lindner. "On Continuous Magnetically Enhanced Centrifugation in Large Scale Downstream Processing of Bioproducts". PhD thesis. 2014. DOI: 10.5445/IR/1000042771.

[118] R. Gerber and R. R. Birss. "High gradient magnetic separation". In: *Research Studies Press Div. of John Wiley & Sons, Ltd., 1983,* (1983), p. 209.